Finite Element Modelling of Phospholipid-Shelled Microbubbles for Therapeutic Uses at Low Acoustic Pressures

Gaël Yves Vincent Léauté

Ultrasound Group
School of Electronic and Electrical Engineering
University of Leeds

Submitted in accordance with the requirements for the degree of

Doctor of Philosophy

October 2014

The candidate confirms that the work submitted is his/her own and that appropriate credit has been given where reference has been made to the work of others.

This thesis is dedicated to my parents Annick Léauté and Yves Léauté, to my brother Xavier Léauté and my fiancée Chen Ding.

Acknowledgements

My sincere thanks to my supervisor Dr. Steven Freear for the encouragement, patient guidance, and advice he has given during the PhD. I thank Dr. David Cowell, Dr. James McLaughlan, Dr. Sevan Harput for their support and helping me keep things in perspective.

I would like to thank all the members of the ultrasound group at the University of Leeds: Chau Vo, Robert Ingham, Stephen Staples, Zainab Alomari, Safeer Hyder, Asraf Moubark, Chrisoula Chappell, Dr. Peter R. Smith, Dr. Muhammad Arif, Benjamin Raiton, Stephen Ellwood, Olaoluwa Olagunju, Dr. Alexandro Pirelli and David Charutz. My fellow graduate students also deserve thanks for the warmth they brought.

Many thanks to Anna de Jong for her secretarial assistance. I also wish to express my gratitude to the members of my examination committee Prof. John Cunningham and Dr. Steven Lind.

I acknowledge the generous financial support from the Sir Richard Stapley Educational Trust.

Abstract

The use of clinical Ultrasound Contrast Agents (UCAs), in the recent years, has seen novel applications, such as the development of UCAs for therapeutic drug delivery for the treatment of cancerous tumours and gene therapy. Common UCAs are microbubbles encapsulated with a monolayer of amphiphilic molecules, such as phospholipids or fatty acids. The interaction of the molecules at the interface with the adjacent gas and liquid phases in the presence of an acoustic pressure allows the occurrence of bending moments and shear forces in the coating, which emerge as surface waves.

In this study, the surface modes of SonoVue® microbubbles are observed using high-speed imaging, and accordingly are compared to the numerical solutions of a three-dimensional finite element model. Comsol Multiphysics® is employed in an effort to implement the viscoelastic properties of the thin material encapsulating SonoVue® UCA. This work discusses the possible problems encountered in finite element analysis to model the deformation of thin viscoelastic shells. The proposed model allows the simulation of non-spherical deformations at low acoustic pressures (50-80 kPa) in an effort to examine the mechanisms contributing to the presence of shell modes.

The numerical results demonstrate that the surface mode amplitudes are dependent on a relaxation time, which models the time necessary for the amphiphilic molecules to reach an equilibrium state. Additionally, a decrease of separation distance between a microbubble and a thin viscoelastic membrane is shown as contributing to the doubling

of the surface mode amplitude. The finite element model is able to show that significant perturbation in a cell membrane is present when a bubble exhibited surface modes of the second order. These effects are shown to contribute to the understanding of the effectiveness of sonoporation — a process during which cell membranes show an increase of permeability in the presence of ultrasound and UCAs, thus permitting therapeutic agents to enter the cells.

Contents

List of Figures

List of Tables

Nomenclature

Abbreviations	
CCD	charge-coupled devices
DPPC	dipalmitoylphosphatidycholine
FE	finite element
FEM	finite element method
Mfps	million frames per second
MI	mechnical index
PEG	polyethylene glycol
Pmma	poly(methyl methacrylate)
R-P	Rayleigh-Plesset
SLS	standard linear solid
UCA	ultrasound contrast agent
Variables	
c_g	velocity of sound in the gas
c_m	velocity of sound in the medium
d	separation distance between two bodies
e	shell thickness
e_{mem}	membrane thickness
e_{cell}	cell thickness
e_{Pmma}	Pmma layer thickness
E	shell Young's modulus
E_1	shell dissipating elastic modulus
E_{mem}	membrane elastic modulus
E_{cell}	cell elastic modulus
f	source term in the Helmholtz equation (chapter 2)

f	frequency
f_0	resonance frequency
G	shell shear modulus
G_1	shell dissipating shear modulus
k	wave number in the medium
$\mathbf{k}$	direction of the planar wave field
M_n	mean molar mass
$\mathbf{n}$	outward pointing unit normal vector on boundary
p_A	absolute pressure
p	the unknown pressure variable
qm	symmetric tensor of the spring and dashpot pair m
R_s	the specific gas constant
R_0	initial bubble radii
R	the universal gas constant
s	the Laplace variable
s_d	stress deviator tensor
$\mathbf{s}$	total stress tensor
t	time
t'	time delay
T	ambient temperature
Y	shell two-dimensional Young modulus
χ_{eq}	shell elastic dilational modulus
ϵ	strain tensor
ϵ_0	initial strain
ϵ_d	strain deviator tensor
ϵ_{vol}	volumetric stress
η_m	shell shear viscosity of the spring and dashpot pair m
η_1	shell shear viscosity
$\eta_{1,mem}$	membrane viscosity
$\eta_{1,cell}$	cell viscosity
γ	polytropic gas index
Γ	boundary of Ω
Γ_D	Dirichlet boundary
Γ_N	Neumann boundary

κ_{eq}	shell viscous dilational modulus
λ_m	shell relaxation time of the spring and dashpot pair m
λ_1	shell relaxation time
$\lambda_{1,mem}$	membrane relaxation time
$\lambda_{1,cell}$	cell relaxation time
ν	Poisson's ratio
ω	angular frequency of the corresponding signal or field
Ω	domain
ϕ	complex scalar field
ρ_g	density of the gas inside the microbubble
ρ_l	density of lipids composing the shell
ρ_m	density of the medium surrounding the microbubble
σ	applied stress
$\boldsymbol{\sigma}$	Cauchy stress tensor
$\boldsymbol{\tau}$	Cauchy traction vector
$\boldsymbol{\tau}_S$	surface traction vector
τ_{mean}	mean shear stress
τ_{mag}	magnitude of surface traction
τ_{shear}	surface shear
θ	phase

Operators and functions

$\mathbf{A}$	system matrix
$\mathbf{A}^T$	transpose of matrix $\mathbf{A}$
δ_{ij}	Kronecker delta
Δ	Laplace differential operator
$\mathbf{J}$	Jacobian matrix
H	Heaviside function
$\mathbf{\Lambda}$	inverse Jacobian matrix
∇	gradient
ϕ^h	finite-dimensional approximation
Ψ_i	shape function where i refers to the corresponding node number
$\mathbb{R}$	real part of a number
u_ω	weight function
$\hat{x}$	Laplace transform

Chapter 1

Introduction

1.1 Ultrasound Contrast Agents

Ultrasound has versatile uses in the medical field and during the past four decades it has been employed for therapeutic and diagnostic uses. Therapeutic applications include the destruction of kidney stones and thermal necrosis of cancer cells with high intensity focused ultrasound (HIFU) (Aus, 2006). Diagnostic applications include real-time and non-invasive imaging of the heart, liver, breast, bladder, vessels, kidneys, bones and other organs as well as foetuses (Meire *et al.*, 1995). The diagnostic applications also include the Doppler mode which helps to visualise and estimate the blood flow velocity using the Doppler effect (Szabo, 2004). These diagnostic uses of ultrasound employ frequencies in the range of 0.5 to 15 MHz. The spatial imaging resolution is dependent on the wavelength, where the highest frequency provides the shortest wavelength and therefore the highest resolution. Penetration depth is frequency dependent, where attenuation by tissue increases for higher frequencies. Therefore for a given frequency, trade-off between imaging depth and resolution exists. This limitation is accompanied by another one, due to the low contrast between blood and organs or tissues with high vascularity. Kidney, liver and tumours are examples where an increase in contrast between the blood and tissue may help the diagnosis.

In 1968, Shah and Gramiak observed an effect of contrast change in ultrasound images when solutions such as indocyanine green dye, saline or alkaline

serum was injected rapidly into the vascular system or agitated prior to injection (Gramiak & Shah, 1968). The clouds of micron sized air bubbles created in the injected solution scattered more ultrasound than the surrounding tissues. Hence brighter regions at the location of the bubble clouds were observed within the acquired images, and the contrast was enhanced relative to the regions devoid of bubbles with an ultrasound scanner. Early clinical applications of bubbles as contrast agents were focused on the study of the heart such as the diagnosis of ventricular septal defect for the reason that the bubbles were unable to reach the left ventricle in a healthy heart Drobac *et al.* (1983). The limited applications of these early products came from the short life-span of the microbubbles, which was typically less than a second. From these findings, efforts became focused on the development of stable micro-meter gas bubbles for enhanced ultrasound contrast imaging. These are commonly named Ultrasound Contrast Agents (UCAs).

The main constitution of an UCA is a gas core which scatters with incident ultrasound and thus gives their echogenic property, in which part of the emitted pressure is re-transmitted towards the ultrasound probe. Free or encapsulated gas bubbles perform as excellent ultrasound scatterers because their density is lower than, and their compressibility is higher than that of blood and the surrounding tissues. The difference in density translates into a difference in acoustic impedance at the interface of the gas and the liquid medium, and gives the microbubbles their high echogenicity. Also, when the microbubbles are excited off-resonance with ultrasound, their shell and gas compress and expand, but not necessary in phase with incoming acoustic pressure, resulting in additional emitted ultrasound (Hoff, 2001) and producing harmonic overtones of the original sound wave due to their non-linear oscillations. In diagnostic imaging, using a pulse-inversion mode, linearly responding constituent will disappear while tissues and gas with non-linear compressibility stand out. In the presence of UCA this effect is greatly enhanced and therefore improves and reveals more details than conventional B-mode imaging (Harvey *et al.*, 2000). This is achievable due to UCA size range varying between 0.5 to 10 micrometers, allowing the UCA to reach the smallest capillaries and thus improving the imaging of the vasculature of a given organ or tumour. In ultrasound imaging UCA can achieve significant

improvement of the image quality for non-invasive medical diagnosis (De Jong *et al.*, 1991; Frinking *et al.*, 2000; Goldberg *et al.*, 2001).

Early research of UCA focused on the development of stable encapsulated gas microbubbles with bio-compatible materials to prevent toxicity or immune responses in patients. Various encapsulations were designed to extend their life-span and reduce their average size for them to pass through the capillaries (Goldberg *et al.*, 1994). Echovist (Schering AG, Berlin, Germany) (Fritzsch *et al.*, 1988; Schlief *et al.*, 1990) was the first approved contrast agent for clinical use in Europe (Baert, 2008). This *first generation* UCA contained air stabilised with a coating of galactose (monosaccharide microparticles). These remained stable in the venous system and right ventricle but were found to dissolve during their passage through the pulmonary capillaries (Baert, 2008). The first marketed product for contrast enhancement in the left heart ventricle was Albunex® (Mallinckrodt Medical) (Bleeker *et al.*, 1990), which was introduced in the United States of America in 1994. It consisted of human albumin microbubbles filled with air, and its mean diameter was 3 to 5 µm. Despite the proteinous coating of 15 nm (Christiansen *et al.*, 1994), the lifetime of these UCAs *in vivo* was less than five minutes.

The *second generation* of UCA use perfluorocarbons, sulphur hexafluoride or other gases, which replace the air used in the previous generation. The gases used in these microbubbles are specifically chosen for their heavy molecular weight, which gives their low dissolution property in water, the main solvent in blood. During the production of UCA, the gas is encapsulated by a layer of surface active materials such as amphiphilic molecules or proteins. This encapsulating layer, or shell is used to stabilise the microbubble against dissolution of the gas by lowering the surface tension between the gas and the liquid medium. Commercially available second generation UCA populations have a size range of 0.5 to 10 µm in diameter and a mean diameter of 1 to 3 µm depending on the manufacturing process and the coating used Maresca *et al.* (2010). In this thesis the attention is focused on UCA with a **phospholipidic encapsulation** such as SonoVue® (Bracco Imaging Italia srl, Milan , Italy), Definity™ (Lantheus Medical Imaging, N. Billerica, MA, USA) and Micromarker™ (Bracco, Geneva; Visualsonics,

Canada). The bio-compatible encapsulation allows the UCA sufficient stability for therapeutic application while retaining their excellent ultrasound scattering properties. These main advantages have brought research communities to study their application for therapeutic drug delivery (Borden *et al.*, 2008; Kooiman *et al.*, 2009; Meijering *et al.*, 2009; Unger *et al.*, 2004).

1.2 The role of sonoporation in therapeutic drug delivery

A combination of ultrasonic insonation and microbubbles can increase the permeability of a cell membrane. This mechanism is described as sonoporation and enables the uptake of a therapeutic agent by a nearby cell. During the phenomena, the agents, either loaded onto the microbubbles or co-administrated, enter a cell through one or multiple pores created by oscillating microbubbles near the cell membrane. Although it is tempting to propose a single phenomenon driving the sonoporation, it is not always possible to separate the methods from the mechanical effects that are in play. Multiple phenomena might be responsible permitting the sonoporation effect, such as the jetting, the acoustic microstreaming, and the radiated acoustic force . Since the sonoporation is an ephemeral event, to assess its occurrence, a therapeutic drug is often marked or substituted with a fluorescent agent (Delalande *et al.*, 2011; Kooiman *et al.*, 2011; McLaughlan *et al.*, 2013). The effectiveness of the sonoporation process is dependent on the mechanical effect permitting formation of a pore in the endothelial lining, however, due to the method used to assess occurrence of sonoporation, the delivery method should also be taken into account.

To elucidate the delivery methods, one should first understand how microbubbles can be assembled to incorporate a therapeutic agent in or on their coating. The choices are inherently dependent on the task which they must perform and the type of cells targeted. While some drugs, notably hydrophilic ones, can be co-administered or attached onto the outer surface of the microbubble coating, hydrophobic drugs need a carrier. The latter ones can be loaded onto the inner side of the microbubble coating (Shortencarier *et al.*, 2004) or alternatively are encapsulated within micelles or vesicles (Peyman *et al.*, 2012). In Figure 1.1, a schematic view of vesicle loaded microbubbles is presented. The vesicles are attached onto the microbubbles using avidin proteins, which strongly bind to biotinilated propylene glycol chains used in the lipid mixture for the production of the microbubbles and vesicles. Similarly, antibodies or ligands can be bound to the microbubble coating, which enables the targeting of cells expressing the

sought extracellular membrane protein or antigen. Although microbubbles are not always targeted, compared to freely circulating microbubbles, McLaughlan *et al.* (2013) demonstrated experimentally that targeting increased the efficiency of drug uptake during sonoporation. The characterisation of the sonoporation effectiveness is therefore not solely dependent on the type of microbubble, but also altered by the method used to load the therapeutic agents and the targeting of the cells' ligands. For example, while the use of vesicles might enable larger quantities of therapeutic agents to be loaded onto the microbubbles, the vesicles itself must also release the therapeutic agent simultaneously with the pore formation. Pua & Zhong (2009) and later Kooiman *et al.* (2014) mentioned in their reviews that the plethora of different cell models, ultrasound settings, and cell lines, made it difficult to reach a conclusion on the relation of therapeutic agent uptake with the sonoporation mechanisms.

For some researchers, sonoporation is described as the asymmetric contraction and jetting of ultrasound excited microbubbles. The jetting, or 're-entry jets' are often observed prior to microbubble collapse, known as inertial cavitation. Inertial cavitation creates high shear rates, which can rupture a nearby cell membrane (Ohl *et al.*, 2006; Prentice *et al.*, 2005). Sonoporation is described by Kudo *et al.* (2009) where collapse through fragmentation and dissolution of the microbubbles produces 25.4 % chance of the permanent poration of cells using a single ultrasound pulse of 1.1 MPa peak rarefactional pressure at 1MHz. Prentice *et al.* (2005) described the jetting by microbubbles achieved a 17 % chance of induced sonoporation on a nearby tissue mimicking material. However, in both cases a monolayer of cells were attached to a rigid wall. This inherently affected the direction of the jets, and allowed them to be directed towards the cells. This due to the high elasticity of rigid boundaries (Kooiman *et al.*, 2014). Léauté *et al.* (2012) confirmed by finite element modelling that the transient jet formation in the presence of a viscoelastic membrane is **directed away** from the membrane. The jet formation from the study is reproduced in Figure 1.2, where the formation of a protrusion begins in the sequence *e* and further increases in size in the sequence *f*. The formation of microbubble jets near viscoelastic membranes is comparable to the jets of uncoated bubbles near a water-gas interface, where the

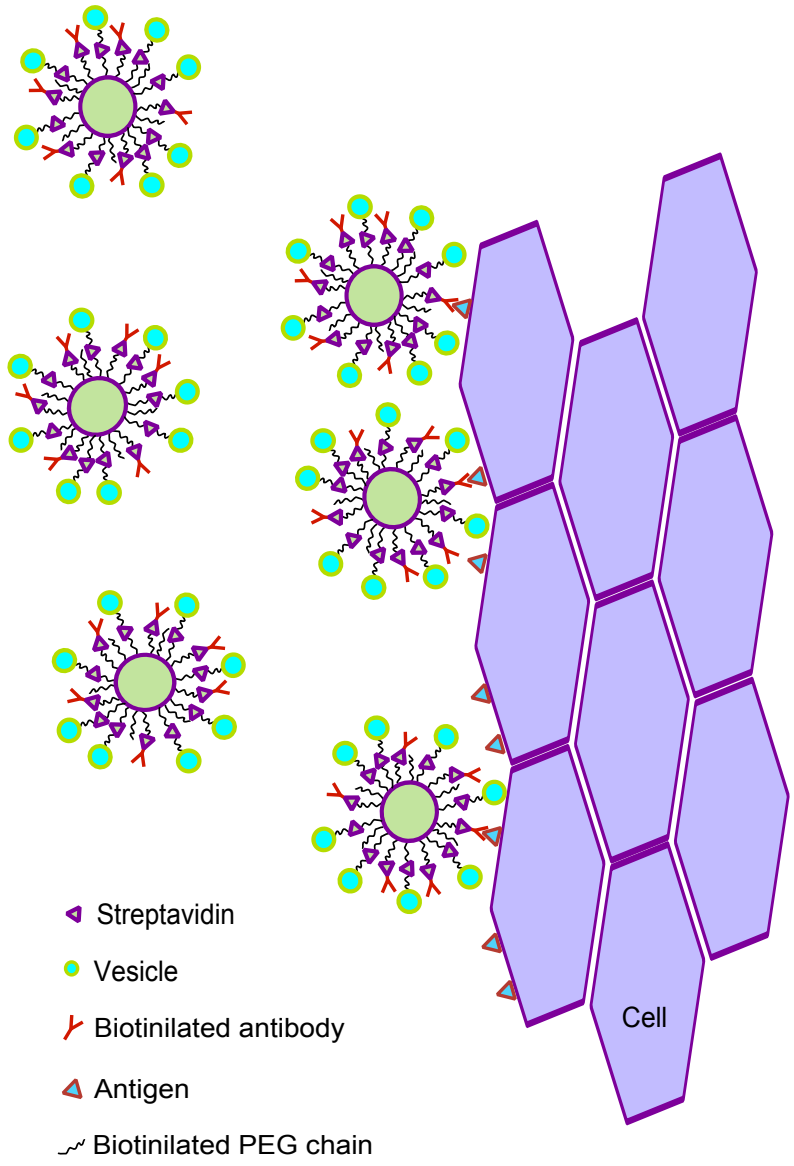

Figure 1.1: Engineered microbubbles to target cells expressing a specific antigen. Vesicles containing drugs are attached to microbubbles with specific peptide chains.

jet direction is pointed away from the boundary (Lind & Phillips, 2013). The discussed studies permit to draw attention to the nature of nearby boundaries when the dynamics of microbubbles is researched.

While *in vivo* studies (Forbes *et al.*, 2008; Lee *et al.*, 2008; Yang *et al.*, 2013) show a preference for the destruction of microbubbles — which allows repeated exposures of ultrasound for successive microbubble populations to burst and wait for the vasculature to replenish and therefore increase the chances of drug delivery to the exposed site —, other studies show inertial cavitation induces drug uptake (Lai *et al.*, 2006), but Forbes *et al.* (2008) concluded that the collapse of microbubbles did not fully explained the results observed. Inertial cavitation was described as not being necessary to provide *in vivo* sonoporation, in that, below inertial cavitation threshold significant sonoporation was observed with a rate up to 7% sonoporated cells. At acoustic pressures where 95% of the microbubbles were undergoing intertial caviation, less than 3% of sonoporation was achieved, while the maximum of 10.21% sonoporated cells occurred at pressures on the order of twice the inertial cavitation threshold. However, it might be argued that at those pressures significant loss in cell viability is expected (Lai *et al.*, 2006). Therefore the inertial cavitation alone might not provide efficient sonoporation. These results point to additional mechanical effects that are necessary for the drug uptake into the targeted cells.

Inertial cavitation is a rapid phenomenon whereas oscillations are perennial. Using 5 seconds ultrasound exposure, Van Wamel *et al.* (2006) describes that it is the microbubble oscillations interacting with the nearby cells that permitted the membrane permeabilisation. He observed that only the cells undergoing deformation would show an increase in permeability and suggested a poking mechanism where the disruption of the cell membrane permits sonoporation while preserving the cell viability. The pushing and pulling of the cell membrane when a nearby microbubble is undergoing stable cavitation is described as cell massaging. Additionally, when microbubbles oscillate, acoustic microstreaming is generated (Collis *et al.*, 2010; Nyborg, 1958). Doinikov & Bouakaz (2010a), Wu

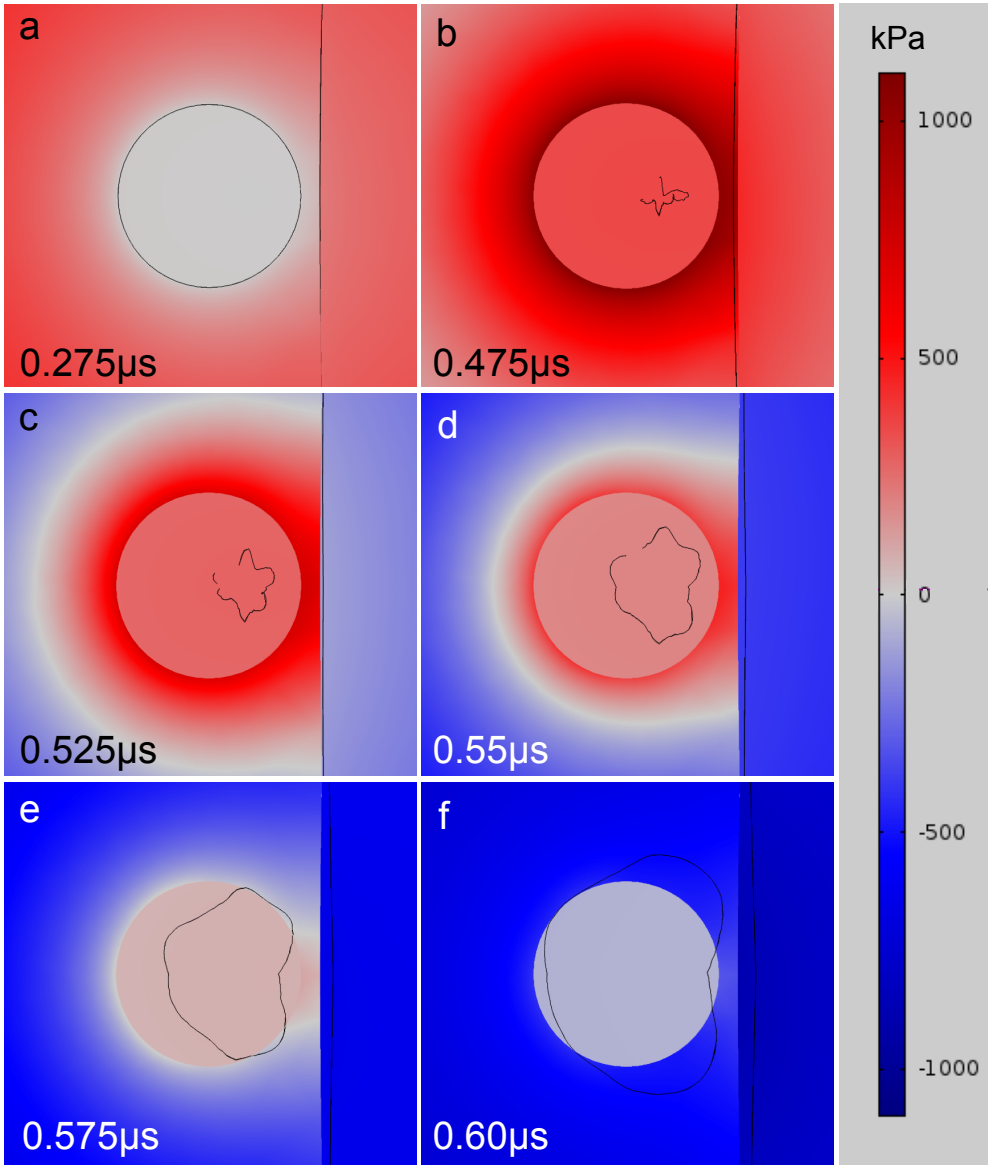

Figure 1.2: Exposure to an 1 MPa sine pulse wave at 1.8 MHz allows the formation of an inward protrusion directed away from a viscoelastic membrane (sequence *f*). Reproduced from (Léauté *et al.*, 2012) © 2012 IEEE.

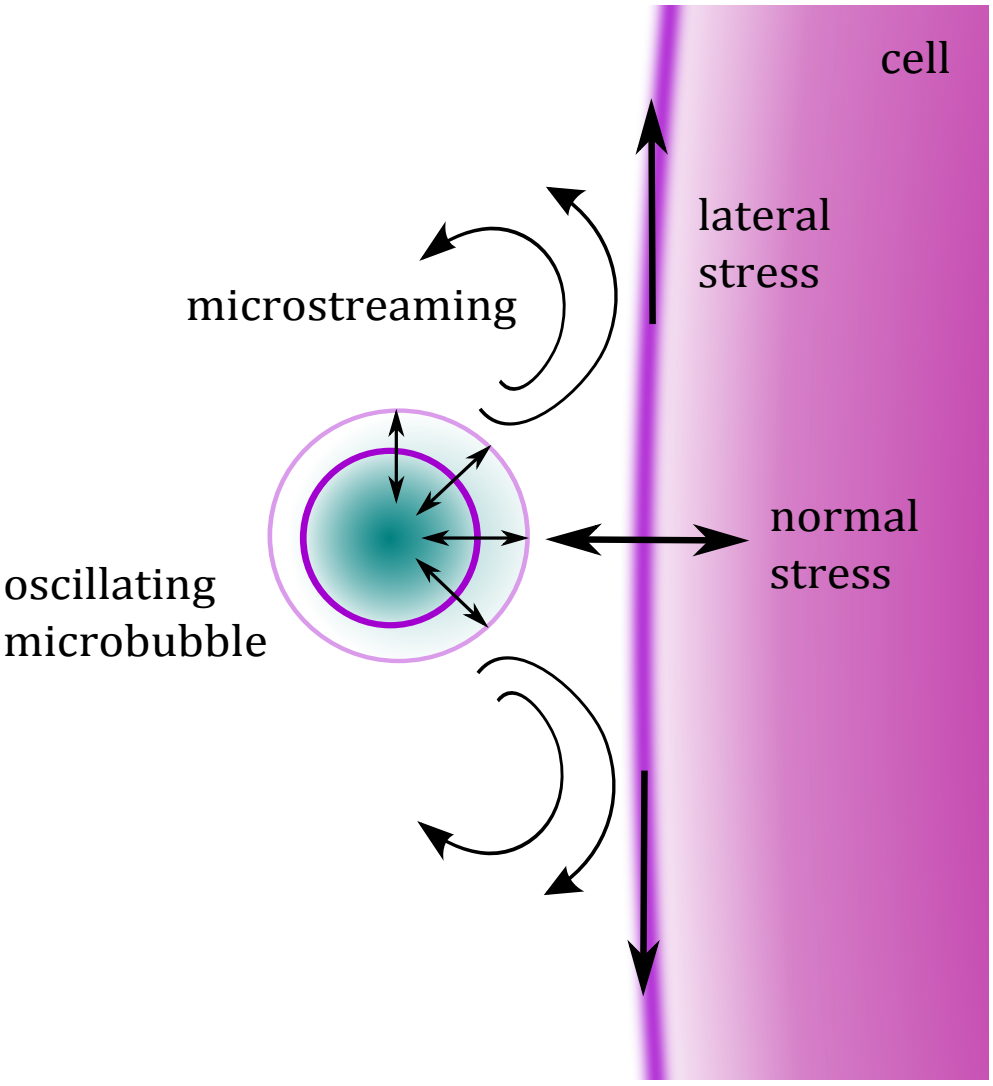

Figure 1.3: Schematic representation of the stresses experienced by a cell during the sonoporation phenomenon.

(2002), and Wu *et al.* (2002) described this as an important mechanism contributing to non-destructive sonoporation. This phenomenon and the cell massaging were proposed in the literature as two important fundamental mechanical phenomena contributing to non-destructive sonoporation (Kooiman *et al.*, 2014). While the cell massaging is thought to create a *normal* extensional stress, the acoustic microstreaming is believed to generate a *lateral* shear stress on the cell membrane. These mechanical actions are illustrated in Figure 1.3. Additionally microstreaming flow surrounding the microbubble can help the diffusion of the drugs in the vicinity of the cell and thus increase drug uptake (Gelderblom, 2012).

Microbubble oscillation amplitudes vary with the frequency of the ultrasound field and achieve the highest amplitude oscillation at the resonance frequency. Thus theoretically, sonoporation depends on the acoustic pressure and the frequency at which microbubbles are insonified. In this context, this gives two options to improve the sonoporation efficiency of microbubbles population: narrowing the size distribution, or in the case of a microbubble population with a polydisperse size distribution, exposing the populations to an ultrasound field composed of a range of frequencies. With poly-dispersed sized microbubbles McLaughlan *et al.* (2013) was able to increase sonoporation efficiency by using chirp excitation signals, which carried a broad range of acoustic frequencies and therefore increase the number of microbubbles undergoing oscillations. Narrowing the size distribution would enable an increase in number of microbubbles being driven near or at their resonance frequency. The production of uniformly sized microbubbles was investigated by Hettiarachchi *et al.* (2007); Peyman *et al.* (2012); Teh *et al.* (2008). However the preponderant limitations to the manufacturing process are: the difficulty to mass produce them due to clogging of the microfluidic channels; the difficulty to predict the microbubble radii which provide maximum yield from the initial design of the chip; low production yields which result in low microbubble concentrations. The latter problem can be alleviated through centrifugation but this would be of impractical use in clinical applications.

Different surface oscillation modes may provide a local gradient of acoustic pressure and characteristics of the flow field which consequently drive different

forces onto the nearby membrane or wall. The surface modes of uncoated bubbles, sometimes referred as the 'bubble dance' or 'shimmering', has given to researchers some insight into the mechanism enabling the cleaning of surfaces with water containing insonified microbubbles (Xi *et al.*, 2014). Offin *et al.* (2014) demonstrated oscillating uncoated microbubbles were effective at cleaning micrometer pores under less than a second of ultrasound exposure. Kim *et al.* (2009) studied the removal of particles by oscillating uncoated micron sized bubbles and argued the force generated by the microstreaming is an order of magnitude lower than the force necessary for the particle detachment. Interestingly the results were favouring the pressure gradient as the main mechanism permitting the removal of particles. The acoustic microstreaming flow and surface modes are interdependent mechanisms (Wang *et al.*, 2013). However, both the streaming effect and the acoustic pressure contribute to the mechanism permitting sonoporation (Kooiman *et al.*, 2014). Watson *et al.* (2003) studied the mass transfer in the vicinity of bubbles undergoing volume oscillations and bubbles with surface modes. They measured an increase in mass transfer for bubbles with surface modes compared to those undergoing volume oscillations. This correlates with Tho *et al.* (2007) who observed a 2 to 3 times increase in streaming velocities of shape mode oscillating bubbles compared to volume and translating modes of oscillation.

While microstreaming contributes to a continuous stress, it is a resultant force driven by the oscillations. Those oscillations are primarily dependent on the acoustic pressure. The surface modes contribute to the microstreaming, but their dependency on the nature of the gas liquid interface, which is, for an UCA, its coating, has not yet been quantified. Additionally, the influence of a nearby boundary on the nonspherical microbubble shape oscillations is not entirely clear. In the case of a gas bubble, the onset pressure for shape oscillations is lowered in the presence of a wall (Xi *et al.*, 2014), however experimental study by Birkin *et al.* (2011) suggests the presence of a wall does not necessarily affects the mode order, in that the theoretical pressure threshold to calculate the predicted surface mode was still valid for a bubble bound to a wall. These observations have not yet been made for coated microbubbles. Furthermore, the observation of nonspherical oscillations in experimental studies suggest the presence of a nearby

boundary strongly affects the shape oscillation of coated microbubbles and that the break-up of the microbubble is inherently linked to the presence of non-spherical shapes (Caskey *et al.*, 2006; Vos *et al.*, 2008; Zhao *et al.*, 2005). The introduction of surface modes in analytical and numerical models is the first step in understanding the conditions leading to the break-up of the microbubble coating and may provide additional clues to the mechanisms permitting sonoporation.

1.3 Objectives and outline of the thesis

The mechanisms of sonoporation events in the presence of coated microbubbles and ultrasound is not fully understood. Once a microbubble has reached the vicinity of a cell, the influence of the nearby cell membrane on the oscillation modes, particularly the non-spherical oscillation modes is still unknown. Meanwhile, the literature points towards the acoustic pressures and the hydrodynamic forces exerted on the cell membrane may inherently be dependent on the oscillation modes. The study aims to create a finite element model to provide a numerical analysis of the surface modes and their potential role in the exerted forces by microbubbles on a nearby cell membrane.

The first objective is to define a material model of the microbubble interface adjacent to the gas and liquid phases which permits the occurrence of surface modes. The aim is to implement a relaxation time parameter for modelling of the time required for the shell's molecules reorganisation. In Chapter 2, the surface rheology of lipid monolayers is presented and the implications for a finite element analysis are discussed. Then, the theory of the numerical model is laid out. In Chapter 3, a viscoelastic model for simulating the response of lipid monolayers to ultrasound is proposed. The approach taken provides a novel implementation of the lipid's rheological properties that is compatible with the finite element method. The numerical results of the FE model are compared to published experimental data to calibrate the shell parameters and to ensure these are within the order of magnitude found in the literature.

The second objective is to study microbubbles undergoing surface modes at low acoustic pressures (<100 kPA) and find the mechanisms contributing to the presence of surface modes. In Chapter 4, high speed imaging is employed to measure the eigenfrequencies of the surface modes of SonoVue® microbubbles and a comparison with the FE model is presented to further estimate the relaxation time parameter. The application of the model is then presented through the assessment of the surface modes amplitudes

dependence on the relaxation time parameter and on the distance separating a microbubble and a viscoelastic membrane.

The third and last objective of the study is aimed at estimating and assessing the extent of the mechanical effect of the exerted acoustic pressure on a cell membrane by a nearby microbubble. In Chapter 5, a numerical analysis of the normal displacements and the surface lateral shear of a cell membrane in the presence of the microbubbles is proposed to study the mechanisms permitting pore formation at low acoustic pressures.

The results of the surface modes observations using high speed imaging, their comparison with the finite element model and the study of the mode amplitude in relation to the distance separating a microbubble and a viscoelastic membrane will be submitted as:

Gaël Yves Vincent Léauté, James McLaughlan, Sevan Harput, Steven Freear, "Surface modes oscillations of phospholipid-shelled microbubbles near a boundary", *The Journal of the Acoustical Society of America* (Manuscript in preparation)

Chapter 2

Modelling and numerical method

2.1 Surface rheology of amphiphile coated microbubbles

Surface tension has an important role to play in determining the mechanical properties of interfacial films. Langmuir monolayer troughs are an example of such films, and can be composed of numerous amphiphilic molecules, such as phospholipids, surfactants and fatty acids. The surface tension alone does not depend on the change of surface area or the surface curvature, but rather on the cohesive energy between the molecules of the liquid medium (De Gennes *et al.*, 2004). Such is the case of an interface devoid of amphiphilic molecules. Amphiphilic molecules influence the surface tension as they agglomerate on a surface, replace some liquid phase molecules, and accordingly form a Langmuir monolayer, which resists dilation with increasing force. Surface tension decreases since fewer liquid phase molecules can attract one another. Thus, amphiphilic molecules decrease the surface tension at an interface; additionally however, the surface obtains shear and dilational properties (Monroy *et al.*, 1998).

The intra-molecular cohesion of which the surface tension is dependent is higher for the aqueous phase molecules —*i.e.* water molecules— than for the amphiphilic molecules. A water molecule is composed of two positively charged hydrogen atoms and a negatively charged oxygen atom. They form a wedge

structure due to an unequal sharing of the electrons in the covalent bond. A positive polarity arises on the side at which the hydrogen atoms reside, and a negative polarity on the oxygen atom side; hence, water is a polar molecule. As a result, water molecules have a strong electrical dipole moment. With the mutually attracting positive and negative inter-molecule charges, water molecules attract on another in a coherent manner; this could be described as a force that is present between all of the water molecules — and not only at the interfaces with gasses — but is certainly observable at those interfaces as the surface tension.

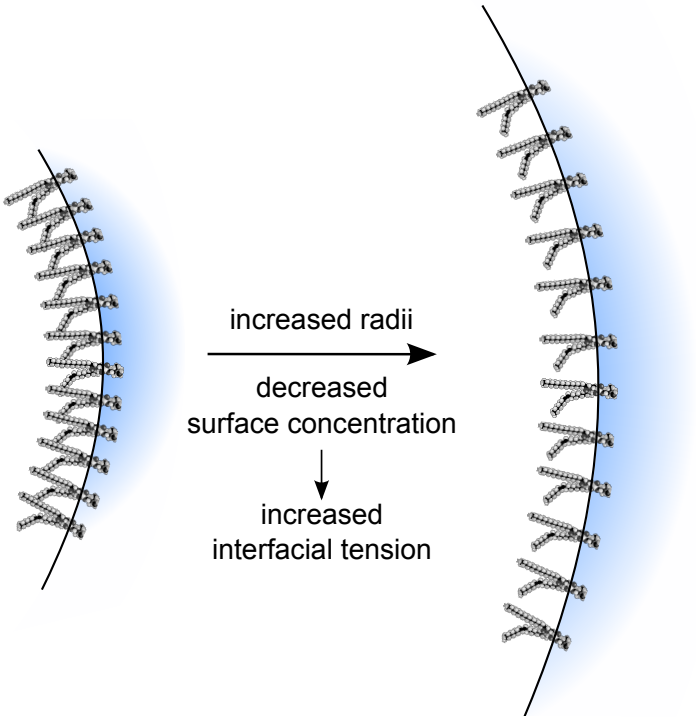

Figure 2.1: Increased surface decreases the concentration of the amphiphilic molecules at the gas-liquid interface, which increases the interfacial tension.

As the microbubble surface increases due to a rarefaction of the acoustic pressure, there is an increase of aqueous phase molecules —mostly water molecules— interacting at the interface exist, which results in an increase in interfacial tension. For a decreased surface, the opposite is witnessed. Thus, the following can

be assumed: the interfacial tension between a gas and a liquid phase depends on the concentration of the amphiphilic molecules in the Langmuir trough. An increase in surface will decrease the concentration of the amphiphile molecules at the interface, whilst the simultaneous increase of water molecules at the interface increases the interfacial tension (see Figure 2.1). Alternatively, a decrease in surface, accordingly increases the concentration of the amphiphile molecules, and thus, decreases in the interfacial tension until the critical monolayer concentration (CMC) is reached. At CMC, no more molecules can fit at the interface. A further decrease in the microbubble gas volume results in the buckling of the amphiphilic molecules at the interface, and their possible desorption into adjacent phases (see Figure 2.2).

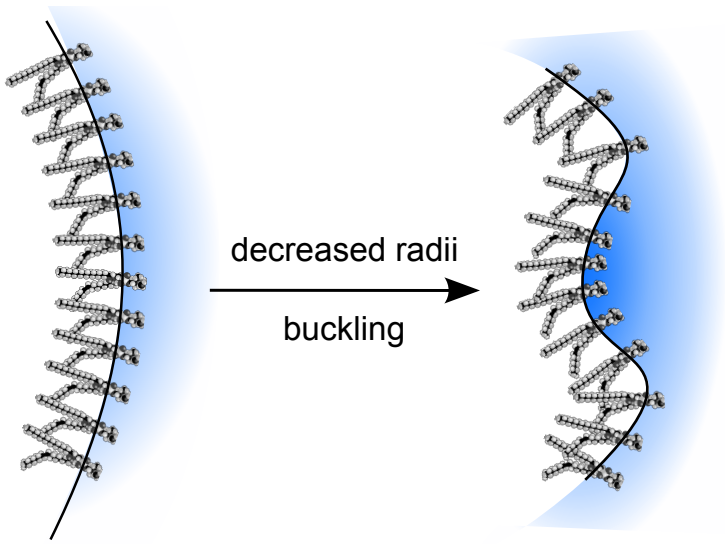

Figure 2.2: The decreased surface causes buckling of the amphiphilic molecules at the gas liquid interface.

In the literature, the study of interfacial properties is often discussed in terms of surface rheology. The term 'rheology' is used to describe the mechanical properties of materials that exhibit solid and fluid mechanics. Viscoelastic materials are rheological materials with elastic and viscous properties. The term 'elastic',

in this context, refers to the ability of the materials to return to their original state once the applied stress is ceased. This memory effect is accompanied by the viscosity, which corresponds to the material's molecules ability to diffuse and resist shear flow within the material. The combination of both properties allows viscoelastic materials to be dependent on the rate of the applied stress. In this study, the rheological term is a relaxation time λ, which represents the time needed for the molecules at the interface to reach equilibrium. The relaxation time that characterises the interface serves as a model to take account of the dynamic properties caused by the absorption and desorption effect, and the orientation and organisation processes of the amphiphilic molecules. The implementation of the relaxation time within the FE model is explained in Section 3.2.2.

The increase of interfacial tension whilst the interfacial layer is dilated has led the research community — including Dimitrov *et al.* (1978) — to model the interface by analogy to a material resisting dilation with a dilational elastic modulus. One can note that the surface tension and the dilational elasticity have the same units of $\mathrm{N.m^{-1}}$. Saulnier *et al.* (2001) and Malzert *et al.* (2002) have shown that the rheological dilational behaviour of phospholipids, surfactants, polymers and proteins at a gas-water interface have properties homologous to a two-dimensional viscoelastic material. Espinosa *et al.* (2011) explain the mechanics of lateral diffusion in lipid monolayers as depending on the mobility of the molecules at the interface, which, in turn, affect their rheological behaviour (e.g., fluid-, gel-, plastic-like behaviour). This behaviour dependency can be related to **the rate of the applied shear**, as described in Figure 2.3, which translates into **a frequency dependency**.

The molecules' lateral mobility can be related to the molecules' ability to reorganise their distribution across the surface. At low shear rates, as shown in Figure 2.3c, the inter-molecule reorganisation can take place similar to the molecules of a fluid. At high shear rates, as shown in Figure 2.3b, no, or altogether limited, inter-molecule reorganisation can take place, resulting in a plastic- or elastic material-like behaviour. This can be explained by the amount of inter-molecule friction, where, at high shear rates, the high amount of friction prevents

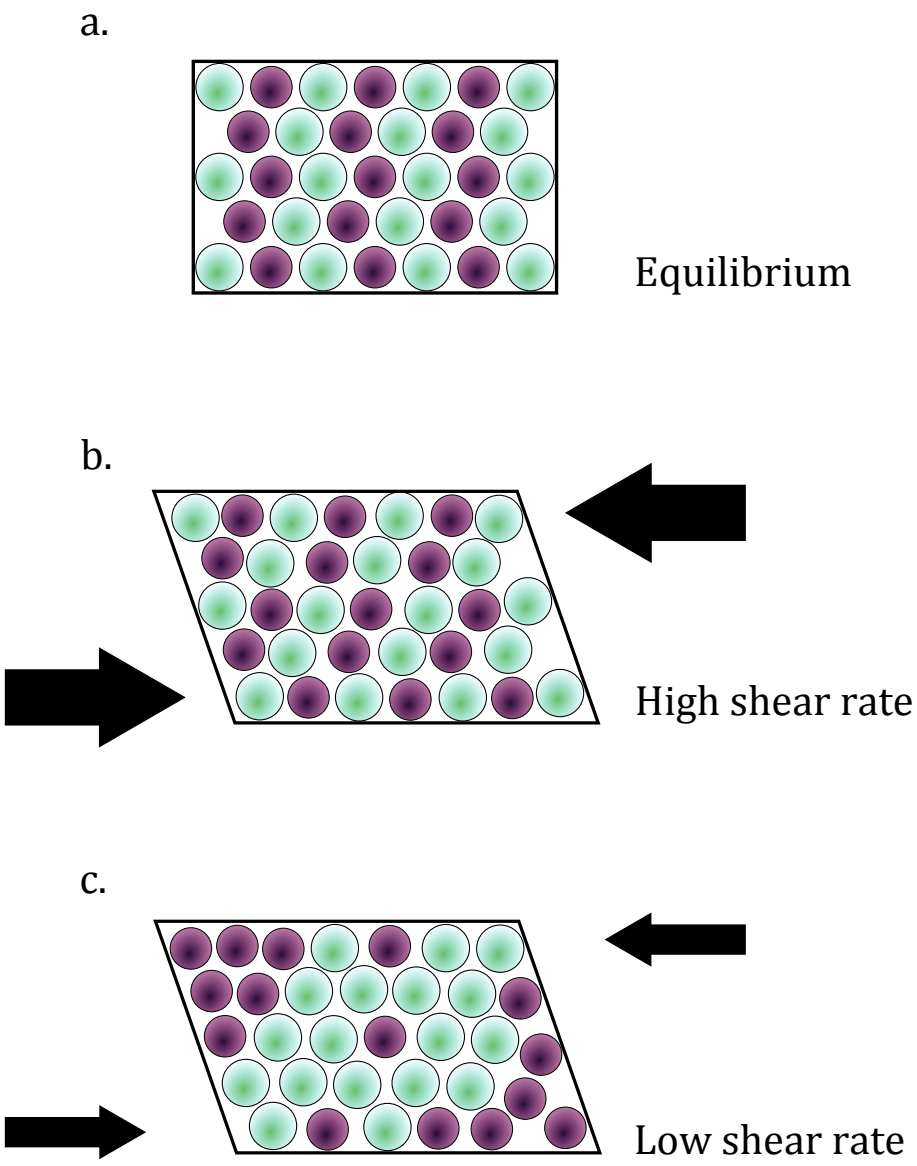

Figure 2.3: A schematic view of a monolayer interface. The mobility of the molecules at the interface affects their reorganisation. At a high lateral shear rates (b.), their mobility is low due to high inter-molecular friction similar to an elastic material. At low lateral shear rates (c.), their mobility allows spatial reorganisation which can be described as lateral flow.

reorganisation, and inversely, at low shear rates, the low friction allows reorganisation. The latter can give the properties of increased fluidity at low shear rates, but reduced fluidity or solid-gel-like behaviour at high shear rates. This mechanical behaviour is recognised as related to the relaxation of the elasticity (Monteux *et al.*, 2004).

Additional to the lateral shear deformation, we propose in this study a finite element model which enables modelling the transverse shear of the lipids represented in Figure 2.4 by opting for a material of finite thickness. Colin *et al.* (1997) observed the effects of a non-ionic surfactant dynamics on light, and accordingly proposed a method to measure their orientation in relation to the surface of the substrate. Although the transverse shear will not be discussed in this study, it is believed to be related to the bending, buckling and reorganisation mechanisms discussed earlier.

de Jong *et al.* (1994),Church (1995) and Hoff (2001) combined the physics of elasticity and surface tension to model the dynamics of albumin encapsulated contrast agents, such as Albunex® with a Rayleigh-Plesset-like equation. In the work presented by Church a 'constant surface concentration of active molecules is assumed' for the estimation of the surface tension; however, an elastic modulus is implemented in an effort to model the change in interfacial tension. Similar work was adapted to lipid-coated contrast agents including Chatterjee & Sarkar (2003) and Doinikov & Dayton (2007) to model the rheological properties of the lipid interface, and, later, Doinikov *et al.* (2009b) to include shear thinning properties. These models perform well for modelling the one-dimensional radial motion of the microbubble surface; however, all of the above models separate the physics of the surface tension and the elastic properties of the amphiphilic molecules coating the microbubbles. One of the main assumptions in their models is the definition of the surface tension parameter as a constant. The idea of a constant surface tension precludes the use of a dilational elastic modulus to model the variation of interfacial tension, whilst the microbubble oscillates. However Marmottant *et al.* (2005) was the first to have suggested a Rayleigh-Plesset-like equation, where surface tension is not defined by a constant, but rather by a piece-wise

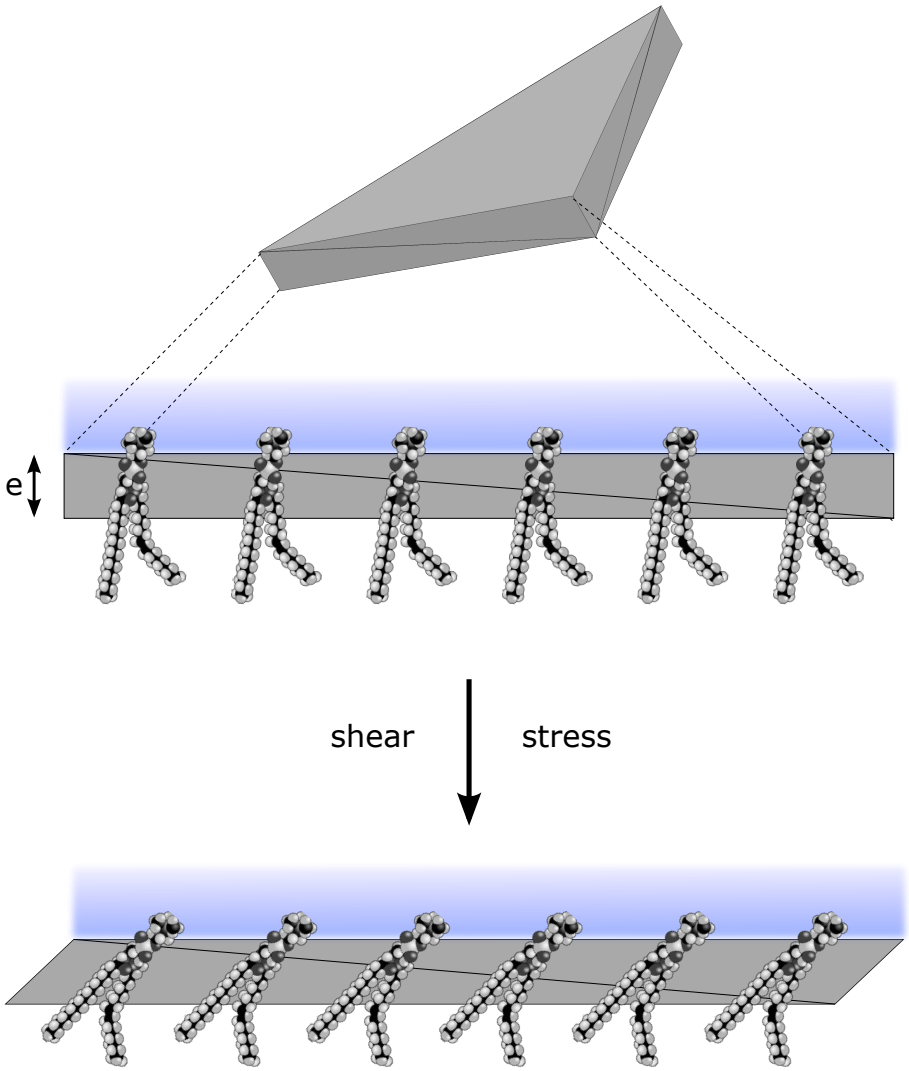

Figure 2.4: Two-dimensional schematic view of three-dimensional tetrahedral shell elements. The elements can model the transverse shear deformation essential for the modelling of shear wave propagation.

function for modelling microbubbles dynamics. In this study, the surface tension is defined as dependent on the dilational elastic modulus, but not in two other states: a buckling state, at which the surface tension is nil, and a ruptured state, at which the surface tension can only take the surface tension value of the fluid medium. In this study, we propose a viscoelastic material to model the rheological dynamics of the amphiphilic molecules at a gas liquid interface as a single physical entity. In the Section 2.2, the considerations taken into account concerning the implementation of thin viscoelastic material into a FE model are introduced. Subsequently, in Section 3.2.2, the implementation of the viscoelastic material equations within the FE differential equations are presented.

2.2 Small strains, large deformations in curved thin shells

Robert Hooke first described the deformation of a spring as proportional to the magnitude of the applied force (Hartsuijker & Welleman, 2007). This law, recognised as Hooke's Spring Law, is a first-order linear approximation of the response of elastic materials to applied forces. When the forces and deformations are sufficiently small, the strain–stress relation of most elastic materials has a linear relationship, which is, by analogy, identical to Hooke's law. In the modern theory of elasticity, which generalises Hooke's law in all directions of the considered space, a tensor is used to represent the linear relationship between the strain and stress in each direction. For a homogeneous and isotropic material, the strain–stress relation must be independent of the directions in space; therefore, the linear elasticity theory for continuous media in isotropic materials is represented by a symmetric strain tensor.

2.2.1 Geometrical nonlinearity for thin shells

The plate theories were developed for the analysis of thin structures, whilst simultaneously reducing the mathematical complexity. In the case of a curved plate, the term 'shell' is used. As in the modern theory of elasticity, the load magnitude needs to be sufficiently small in order for the linear shell theory to be applicable; otherwise, a nonlinear shell theory is required (Wan & Weinitschke, 1988). If the strain–displacement relation is nonlinear, but linear stress–strain is adequate, such a relation then is a geometrically nonlinear theory. Thin shells are such a case, and when using conventional linear elastic materials, there is good reason to formulate geometrically nonlinear theories with the assumption that kinematics can be characterised by finite displacements but small strains.

Lamb (1882) and Rayleigh (1881) were the first to attempt to solve the theory of kinematics of thin, elastic spherical shells for the study of free vibrations. However it was not until the work of Love (1888) that the classic theory of shells was

laid. In these geometrical nonlinear theories, the displacement components u and v tangential to the surface curvature of the shell are assumed small compared to the normal displacement w, for which the strain–displacement relation of u and v remains linear.

The Kirchhoff-Love theory of thin shells would be adequate for pure elastic shells. Pure elastic plates and shells are prevalent and readily implemented in most finite element modelling software; however, as discussed previously in Section 2.1, viscoelastic properties are necessary in order to model the rheological behaviour of the amphiphilic molecules at the gas-liquid interface. The Mindlin-Reissner plate theory — in comparison to the Kirchhoff-Love theory — does not neglect the shear deformation through the thickness of the plate and therefore would be more adequate for modelling the rheological aspect of amphiphilic molecules. Truesdell (1945) discusses the compatibility condition of three-dimensional strains for shells of revolution when the thickness is assumed finite. If Hooke's Law is considered —of which the modern theory of elasticity is based— then, in order to ensure the conditions of compatibility are satisfied, a variable thickness should be considered in order to compute the correct values of shear stress and shear strain across all three directions, including across the thickness. The Reissner plate theory assumes a quadratic shear stress through the thickness; however, the Mindlin's theory assumes that there is a linear variation of displacement across the plate thickness, and that the plate thickness does not change during deformation. Consequently, a strain–displacement incompatibility arises. In order to alleviate the incompatibility, a shear correction factor is commonly implemented in the Mindlin-Reissner plate theory. The implementation of the Mindlin-Reissner plate theory for finite element modelling generally requires mixed formulations —the most prevalent approach, where the pressure is implemented with an independent degree of freedom—, which results in the approximation of Hooke's law. In addition, the elements need to be carefully formulated so as to satisfy the mathematical conditions of stability and convergence (Brezzi *et al.*, 1989; Hughes & Franca, 1988). Thus, two-dimensional elements or boundary elements could be used to model the microbubble coating;

however, the Mindlin-Reissner plate theory was not used owing to the fact an implementation of the viscoelasticity with two-dimensional shell elements in Comsol Multiphysics® was not identified. In this work, a more conservative approach is favoured through the employment of three-dimensional elements. Comparatively, this increases the numbers of degrees of freedom to solve, but ultimately reduces the complexity of the implementation and accordingly limits the approximation of the results.

In finite element modelling, the element type needs to be chosen according to the problem to be solved whilst also ensure the complexity is kept to the minimum for reduced computational load. Quadratic wedge elements with 10 nodes per elements were studied. For a spherical shell discretised by single wedge elements across the thickness, a shear locking phenomena was observed [results of this avenue are not presented in this thesis]. This effect prevents the shape of the shell from taking other forms than a sphere, and is most prevalent in thin shells. Moreover, radial oscillation amplitudes would be limited to less than 1% of the initial radii. This problem arises as a result of the volumetric locking phenomenon in quasi-incompressible materials — in this study, lipids are considered quasi-incompressible; in other words near perfectly compressible materials, such as cork oak, are characterised by a Poisson ratio close to 0. In the same manner, rubber-like materials and liquids are considered quasi-incompressible and have a Poisson ratio closely under 0.5 —. Flores (2013) discusses different techniques centred on avoiding locking phenomena in shells with quasi-incompressible materials for geometric and material nonlinear behaviour. These include the averaging of the volumetric strain throughout each element, selective reduced integration, assumed natural strains and enhanced assumed strains. These techniques help to reduce the total number degrees of freedom for reduced computation complexity whilst maintaining faithful simulations of the material properties; however, such techniques are not necessarily readily implemented in finite element simulation software. The implementation of these techniques for thin materials in Comsol Multiphysics® was not available at the time of study.

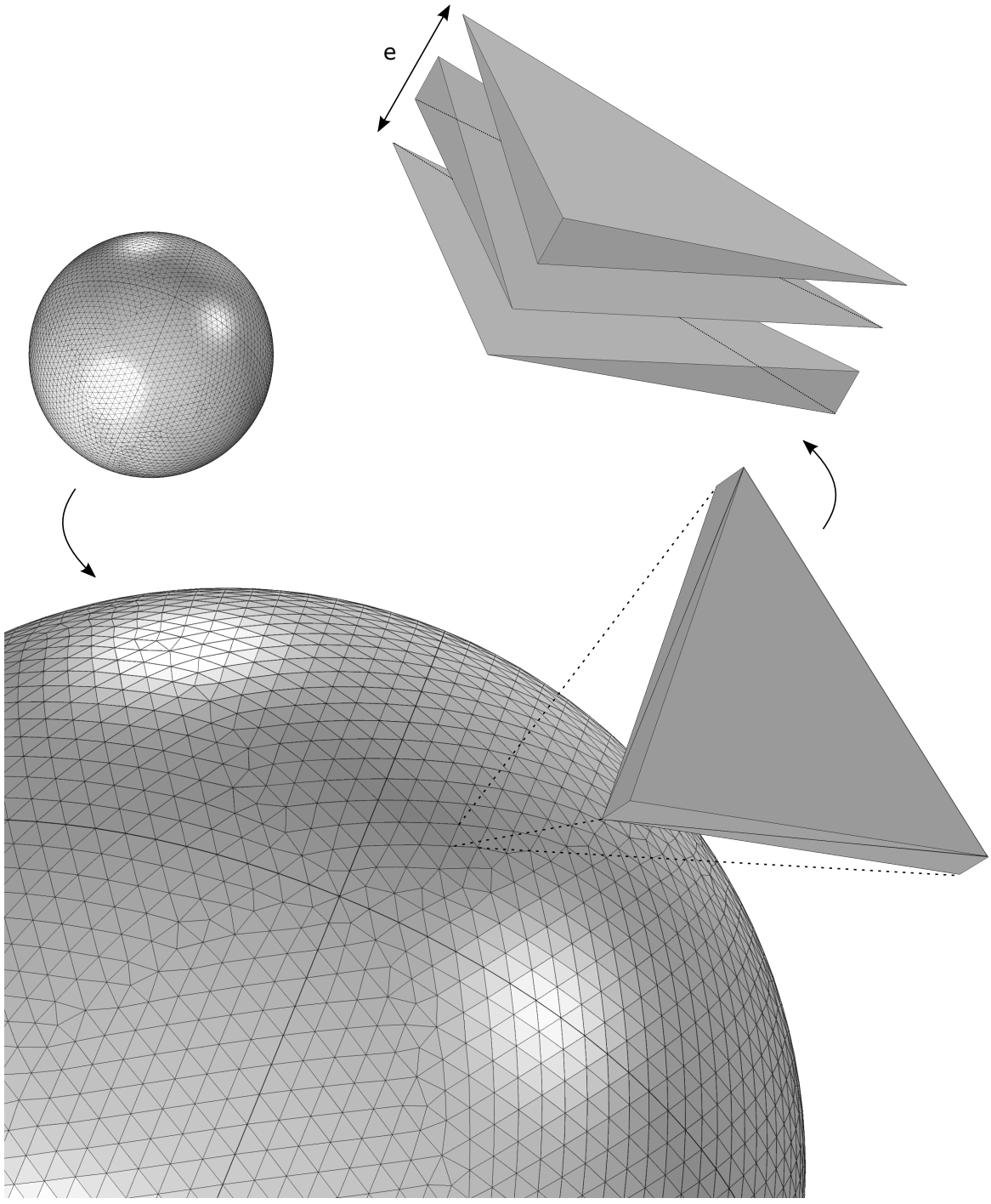

Figure 2.5: The microbubble shell is discretised by three tetrahedral elements across the thickness e. The schematic is not to scale.

In this research, tetrahedral elements are used to model a thin spherical shell of 2 nm in thickness. This size is an approximate thickness of phospholipids monolayers, calculated by halving the one of lipid bilayers (Lewis & Engelman, 1983). In an effort to satisfy the condition of compatibility of the aforementioned Hooke's law, a minimum of 3 tetrahedral elements were assembled across the shell thickness in a form of a wedge. Figure 2.5 illustrates the assembly of the elements. Additionally, in an effort to accommodate the curvature, the tetrahedrals are quadratic. The quadratic geometric order enables the elements to fit the curvature defined by the geometry at the initial position. The elements of first-order would not be adequate as, at the nodes connecting the elements, an angle would exist. This angle would interfere in calculating the distribution of strains tangent to the curvature.

In an element, the order of the shape function defines the maximum order of the Lagrange (polynomial) interpolations characterising the element's nodes' position. For a more in-depth introduction to the finite element method and element order, the reader is referred to Section 2.3. A linear (first-order) shape function is adequate to model the linear coupling between the normal deformations and the in-plane strains (Paulose & Nelson, 2013). Generally, the geometry and displacements of an element are represented by the same set of shape functions. Such elements are called isoparametric elements. Super-parametric elements have shape functions of higher order than their geometric representation. Sub-parametric elements have less resolution than their geometric representation. The study will be limited to isoparametric elements, as the FE modelling software is commonly limited to this type of geometric representation of their elements.

A rheological material has an elastic modulus that can relax (see Section 2.1); thus, the elastic modulus is variable, and the stress–strain relation must be nonlinear. A FE model might not — or only with difficultly — converge to a solution, since it decomposes the problem in linear differential equations $Av = f$ that would admit more than one solution. However, a nonlinear material can be approximated by the generalised Maxwell model (see Section 3.2.2), therefore, allowing the FE model to solve a linear stress–strain relation and thus avoiding

the complexity of nonlinear relations. The generalised Maxwell model allows one to approximate the nonlinear characteristic of certain materials through a series of elastic constant and relaxation time pairs.

2.3 Introduction to finite element method

The finite element method (FEM) is a widely procedure used to numerically approximate a solution of a set of partial differential equations (PDEs). The FEM is based on approximating a solution by piecewise smooth polynomial functions on convex sub-domains such as polygons or polyhedrons. The object of this chapter is to show how a general problem is decomposed with the appropriate differential equations and unstructured mesh grids to allow the FEM to converge to a solution. This introduction follows the approach to FEM explained by Hughes (2012), and Zienkiewicz & Taylor (2005) and covers the notions necessary to understand FEM with an example. The reader is referred to these introductory books for a more detailed explanations of the intricacies encountered in solving FEM problems.

2.3.1 The problem domain

The definition of the problem comes as described in Figure 2.6 by the representation of its physical domain Ω and its boundaries Γ. In FEM all domains must have a finite volume and are delimited by boundaries. Unlike in a mathematical problem, where solutions to the infinite generally exist, in FEM, owing the discretisation of a domain into finite elements, representation of the infinite is not readily available. A solution to the problem of waves travelling to infinity is discussed in chapter 3.

The boundaries Γ_N and Γ_D represent the two types conditions that exist at the limits of a domain Ω. A Dirichlet boundary Γ_D defines the conditions of the displacements or potential, whereas a Neumann boundary Γ_N defines the conditions of the normal stresses or flux. For a scalar field ϕ of the domain the boundary conditions Γ_N and Γ_D must be defined on disjoint parts of the boundary. Here the formulation of the elliptic partial differential Helmholtz equation is proposed to study the problem of a propagating wave on Ω:

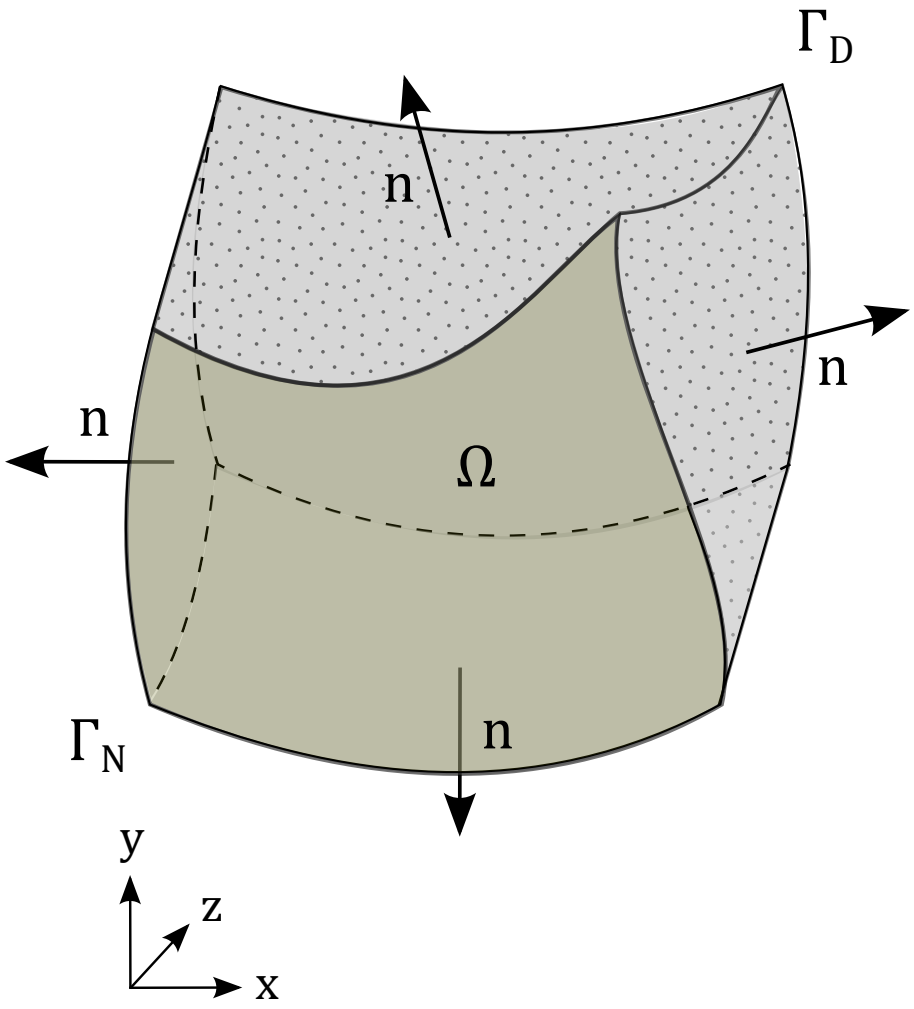

Figure 2.6: A domain Ω in the geometrical Euclidean space $\mathbf{x}, \mathbf{y}, \mathbf{z}$ is delimited by a Neumann boundary Γ_N and a Dirichlet boundary Γ_D whose surface is dotted.

$$\Delta\phi + k^2\phi = f \qquad \text{on } \Omega, \tag{2.1a}$$

$$\phi = g_D \qquad \text{on } \Gamma_D, \tag{2.1b}$$

$$(\nabla\phi) \cdot \mathbf{n} = g_N \qquad \text{on } \Gamma_N \tag{2.1c}$$

where ϕ is the complex scalar field representing the pressure across Ω, Δ is the Laplace differential operator, ∇ is the gradient, k is the wave number. f is the source term in the Helmholtz equation on Ω, g_D and g_N are the functions defining the loads at the locations of Γ_D and Γ_N .

For the remainder of the introduction to the finite element method, the above defined problem of the Helmholtz wave equations on Ω will be used as an example.

2.3.2 The weak formulation of the PDEs

Section 2.3.1 denoted the problem in the strong form which requires continuity on the dependent field variables. The strong form is generally used to define the problem in a FEM software, however the weak form is necessary to solve the problem over a discretisised field. The weak form is also sometimes called the variational form. In order to do so, whatever functions define these variable, they have to be differentiable up to the order of the PDEs in the strong form. There are three commonly approaches used to define the problem in the weak form:

1. The principle of Virtual Work
2. The principle of Minimum Potential Energy
3. The method of weighted residuals — Galerkin, Collocation, Least Squares methods, etc. . . —

The third approach allows the use of weight functions which are required to find a scalar field u_ω converging to the solution u of the system of PDEs. In this case, u_ω is called the weight function which are also known as the test function in the literature. The main idea here is that u_ω allows to find a approximation converging to the average solution over the whole Euclidean space Ω where u is

defined. In the example of the Helmholtz wave equations ϕ_ω is defined as the weight function.

In a first step, the PDE 2.1a is multiplied by the test function ϕ_ω and integrated over the domain Ω:

$$\int_\Omega \phi_\omega[\Delta\phi + k^2\phi]\mathrm{d}\Omega = \int_\Omega \phi_\omega f \mathrm{d}\Omega, \tag{2.2}$$

In a second step, 2.2 is integrated by parts using the Green's first identity (Johnson, 1987):

$$\int_\Omega v(\Delta u)\ \mathrm{d}\Omega + \int_\Omega \nabla u \cdot \nabla v\ \mathrm{d}\Omega = \int_\Gamma v(\nabla u \cdot \mathbf{n})\ \mathrm{d}\Gamma, \tag{2.3}$$

where $\mathbf{n}$ is the outward pointing unit normal field of the piecewise smooth boundary Γ. This identity can also derived from the Gauss' theorem and the product rule of a scalar and a vector field.

Thus with $v = \phi_\omega$ and $u = \phi$ continuously differentiable field, Green's theorem is applied to the domain Ω and its boundaries Γ to reduce the maximal order of the derivatives. The weak form 2.2 is reformulated to yield:

$$-\int_\Omega \nabla\phi_\omega \cdot \nabla\phi\ \mathrm{d}\Omega + k^2 \int_\Omega \phi_\omega\phi\ \mathrm{d}\Omega + \int_\Gamma \phi_\omega(\nabla\phi)\cdot\mathbf{n}\ \mathrm{d}\Gamma = \int_\Omega \phi_\omega f\ \mathrm{d}\Omega, \tag{2.4}$$

The boundary Γ is decomposed into the two sub-boundaries, the Dirichlet and the Neumann boundary:

$$\int_\Gamma \phi_\omega(\nabla\phi)\cdot\mathbf{n}\ \mathrm{d}\Gamma = \int_{\Gamma_N} \phi_\omega(\nabla\phi)\cdot\mathbf{n}\ \mathrm{d}\Gamma + \int_{\Gamma_D} \phi_\omega(\nabla\phi)\cdot\mathbf{n}\ \mathrm{d}\Gamma, \tag{2.5}$$

Substituting 2.1b into 2.5 and using the weak formulation 2.4, the problem can be reformulated such as:

find ϕ such that :

$$\phi = g_D, \qquad \text{on } \Gamma_D, \tag{2.6a}$$

$$-\int_\Omega \nabla\phi_\omega \cdot \nabla\phi \, \mathrm{d}\Omega + k^2 \int_\Omega \phi_\omega \phi \, \mathrm{d}\Omega = \int_\Omega \phi_\omega f \, \mathrm{d}\Omega - \int_{\Gamma_N} \phi_\omega g_N \, \mathrm{d}\Gamma, \tag{2.6b}$$

$$\text{for all } \phi_\omega, \text{ such that } \quad \phi_\omega = 0 \qquad \text{on } \Gamma_D, \tag{2.6c}$$

The original PDE 2.1a requires second order spatial derivatives and therefore its solution ϕ must contain continuous differentiable functions. However, since the weak form uses first order spatial derivatives, its solution can be satisfied by a larger set of functions which are continuous but not necessarily differentiable: these functions are continuous within an element but discontinuities might exist between elements. This defines the term 'weak form', which sometimes is seen as being physically more realistic than the strong form which requires excessive smoothness for its solution (Zienkiewicz & Taylor, 2005).

2.3.3 Discretisation of the weak form

To allow to solve the problem with a mesh, a collection of functions denoted by the superscript h must be defined to permit the discretisation of the weak form. h is the characteristic length of the discretisation, in that a larger h results in a coarser mesh and a smaller h permits to solve the problem on a finer mesh. More of the characteristic length h is discussed in Section 2.4.2. This method will allow to define a finite-dimensional approximation of the solution ϕ and the associated boundary condition g_D defined in 2.6a.

$$\phi \approx \phi^h + g_D^h, \tag{2.7}$$

where g_D^h is a finite-dimensional approximation of the boundary condition 2.1b, and ϕ^h is a finite-dimensional approximation such that $\phi - g_D^h$ and $\phi^h = 0$ on Γ_D.

By substituting the weak approximations 2.7 into the weak form 2.6b, and substituting the weight functions ϕ_ω with a finite number of weight functions ϕ_ω^h, yields:

$$\int_\Omega \left[-\left(\nabla \phi_\omega^h\right) \cdot \left(\nabla \phi^h\right) + k^2 \phi_\omega^h \phi^h \right] \mathrm{d}\Omega = \int_\Omega \phi_\omega^h f \mathrm{d}\Omega - \int_{\Gamma_N} \phi_\omega^h g_N \mathrm{d}\Gamma - \int_\Omega \left[-\left(\nabla \phi_\omega^h\right) \cdot \left(\nabla g_D^h\right) + k^2 \phi_\omega^h g_D^h \right] \mathrm{d}\Omega, \quad (2.8)$$

The weak form contains all the necessary information in a single equation, which can be now be reformulated in the matrix differential equation form.

In order to obtain the discrete problem, the domain is divided by a set of non-overlapping elements. This requires a set of N grid nodes which is represented by a unique index $\{1, 2, 3, \ldots, N\}$. P represents the set of all nodes of the grid. Each grid nodes $n_j \in P$ with $j = \{1, 2, 3, \ldots, N\}$. This discretisation is referred as the Bubnov-Galerkin's method.

$$\phi^h = \sum_{i=1}^{n} \phi_i \Psi_i, \qquad \text{for} i = 1, \ldots, N \quad (2.9)$$

where Ψ_i are the shape functions.

The approximate solution ϕ^h is therefore determined by the coefficients ϕ_i which represent the value of the unknown function at node i. At each node i defined by the coordinates P_i the shape function must satisfy the condition:

$$\Psi_i(P_j) = \delta_{ij}, \qquad \text{for } i, j = 1, \ldots, N \quad (2.10)$$

where δ_{ij} is the Kronecker delta.

The shape functions permit the interpolation of the solution between the values obtained at the mesh nodes within an element. While for example a tetrahedral element is comprised of 4 nodes, the total number of nodes within an element depends on the order of the shape functions Ψ assigned to the element. For linear shape functions, 4 nodes are sufficient to determine the unknown coefficients of the first order polynomials of a tetrahedron. This type of element is called a linear tetrahedron. For quadratic shape functions additional nodes are required. Typically each edge of the element are split by an additional node called internal node. A quadratic tetrahedron has a total of 10 nodes, 4 at each corner and 6 at the middle section of each edges. The number of nodes is therefore related to the order of the polynomials used in the shape function. However in FEM the placement of the nodes is not limited to the edges. The use of the shape functions for the calculus of the unknown coefficients in relation of the coordinate system is further detailed in Section 2.3.5.

From the relation of number of nodes with the element order described above the following remark can be made: An increase of the element order will increase the number of nodes on the discretised domain Ω_h and therefore reduce the characteristic length h and *vice versa*. Similarly an increase or decrease of h could be achieved using new meshes with different element sizes. However, the latter results the computation of new matrices for the coordinate points of each nodes and thus requires considerably more computational resources. The usefulness of a variable characteristic length h will become apparent in Section 2.4.2.

2.3.4 The matrix differential equation form

The matrix differential equation that represents the weak form 2.8 depends on the choice of the shape functions Ψ_i. Lagrangian shape functions are used in this study. Equation 2.9 permits the approximation of the solution (Johnson, 1987):

$$\phi^h = \sum_{i=1}^{M} \Psi_i \phi_i, \qquad \text{for } i = 1, 2, \ldots, M \tag{2.11}$$

where Ψ_i are the shape functions and i refers to the corresponding node number.

The test functions are reformulated in their discrete form:

$$\phi_\omega^h = \Psi_j, \qquad \text{for } j = 1, 2, \ldots, N \tag{2.12}$$

where Ψ_j are the shape functions and j refers to the corresponding node number. In this regard, the weight functions ϕ_ω^h are identical to the shape functions for the approximation of the unknown part of the solution ϕ^h. However, the order of the shape function Ψ_i can be of a lower order than Ψ_j. The latter will be further discussed in chapter 2.4.2.

Similarly, the approximation of the Dirichlet boundary condition becomes:

$$g_D^h = \sum_{l=M+1}^{N} \Psi_l g_{D,k}, \qquad \text{for } l = M+1, \ldots, N \tag{2.13}$$

where $k = N+1, \ldots, M$ comprises all the boundary nodes.

Substitution of the approximations 2.11, 2.12, and 2.13 into the weak form 2.8 results in:

$$\begin{aligned}\int_\Omega \left[-(\nabla\Psi_j) \cdot \left(\nabla \sum_{i=1}^{M} \Psi_i \phi_i \right) + k^2 \Psi_j \sum_{i=1}^{M} \Psi_i \phi_i \right] \mathrm{d}\Omega = \int_\Omega \Psi_j f \mathrm{d}\Omega - \int_{\Gamma_N} \Psi_j g_N \mathrm{d}\Gamma \\ - \int_\Omega \left[-(\nabla\Psi_j) \cdot \left(\nabla \sum_{l=M+1}^{N} \Psi_l g_{D,l} \right) + k^2 \Psi_j \sum_{l=M+1}^{N} \Psi_l g_{D,l} \right] \mathrm{d}\Omega, \\ \text{for } j = 1, \ldots, N \end{aligned} \tag{2.14}$$

Since the unknown coefficients ϕ_i and $g_{D,k}$ are constants the following reformulation can be made:

$$\sum_{i=1}^{M} \phi_i \int_\Omega \left[-\left(\nabla \Psi_j\right) \cdot \left(\nabla \Psi_i\right) + k^2 \Psi_j \Psi_i \right] \mathrm{d}\Omega = \int_\Omega \Psi_j f \mathrm{d}\Omega - \int_{\Gamma_N} \Psi_j g_N \mathrm{d}\Gamma$$
$$- \sum_{l=M+1}^{N} g_{D,l} \int_\Omega \left[-\left(\nabla \Psi_j\right) \cdot \left(\nabla \Psi_l\right) + k^2 \Psi_j \Psi_l \right] \mathrm{d}\Omega, \text{ for } j = 1, \ldots, N \quad (2.15)$$

where the nodes $i = \{1, \cdots, M\}$ include all the unknown coefficients that must be determined, and the nodes $l = \{M+1, \cdots, N\}$ include all the known coefficients from the Dirichlet boundary condition.

Eq. 2.15 can be written in the matrix differential equation form (Johnson, 1987; White, 1985):

$$\mathbf{A}\mathbf{u} = \mathbf{b}, \quad (2.16)$$

where $\mathbf{A}$ is a system matrix whose entries $a_{i,j}$ are defined as:

$$a_{ij} = \int_\Omega \left[-(\nabla \Psi_j) \cdot (\nabla \Psi_i) + k^2 \Psi_j \Psi_i \right] \mathrm{d}\Omega \quad (2.17)$$

One can note in 2.17 that the value of the integral is zero, unless Ψ_i and Ψ_j belong to the same element, therefore most entries a_{ij} of the matrix are zero and $\mathbf{A}$ is sparse. The vector $\mathbf{u}$ contains the unknown coefficients $\mathbf{u} = [\phi_1, \ldots, \phi_N]^T$ of equation 2.11. Thus the scalar field ϕ^h is represented by a vector. The vector $\mathbf{b} = [b_1, \ldots, b_N]^T$ contains all known body forces f and Dirichlet boundary conditions g_D and Neumann boundary conditions g_N. The entries of b are defined as :

$$b_j = \int_\Omega \Psi_j f \mathrm{d}\Omega - \int_{\Gamma_N} \Psi_j g_N \mathrm{d}\Gamma$$
$$- \sum_{m}^{N} g_{D,m} \int_\Omega \left[-(\nabla \Psi_j) \cdot (\nabla \Psi_m) + k^2 \Psi_j \Psi_m \right] \mathrm{d}\Omega, \text{ for } j = 1, \ldots, N \quad (2.18)$$

The above terms a_{ij} and b_j can be calculated element per element and then the contributions of all elements are summed to compute the integral over the complete domain. This method of constructing $\mathbf{A}_{ij}$ and $\mathbf{b}_j$ is called the assembly of the matrices (Johnson, 1987).

The solution is calculated by solving equation 2.16 to get $\mathbf{u}$. Solving requires a factorisation of the system matrix $\mathbf{A}$. The computational time for this factorisation depends on the number of degrees of freedom in $\mathbf{u}$ and on the sparsity of the matrix $\mathbf{A}$.

2.3.5 The Nucleus form

The discrete form of the weak partial differential equation allows to solve the problem with matrices. The computation can be performed element per element and the matrix $\mathbf{A}$ corresponding to an element is called the nucleus matrix and is often referred as the stiffness matrix in the literature. The shape function of a linear tetrahedral element in a 3-dimensional Cartesian space at the node i has the form (White, 1985):

$$\Psi_i(x, y, z) = a_i + b_i x + c_i y + d_i z \tag{2.19}$$

The accuracy of the approximate solution ϕ^h is therefore dependent on the degree of freedom provided by the shape functions. The estimation of the solution can be improved by increasing the order of the shape function. In the case of iso-parametric elements, the shape function's order and the element's order are identical. A shape function of a quadratic tetrahedral element in a 3-dimensional Cartesian space at the node i has the form:

$$\Psi_i(x, y, z) = a_i + b_i x + c_i y + d_i z + e_i xy + f_i yz + g_i xz + h_i x^2 + i_i y^2 + j_i z^2 \tag{2.20}$$

While a linear tetrahedral has 4 nodes, a quadratic tetrahedral is comprised of 10 nodes. At each node of the tetrahedral the shape function 2.19 must satisfy the condition 2.10 which results in a system of equations to determine the coefficients $a_i, b_i, c_i, d_i, \ldots$. However the system of equations will be solved indirectly and therefore the determination of the coefficients will not be necessary. All nodes are mapped into a new coordinate system (ξ, ζ, ψ), often called the natural coordinate system. For example, for a linear tetrahedral, the transformation is given by (Ceric, 2005):

$$\begin{aligned} x &= x_1 + (x_2 - x_1)\xi + (x_3 - x_1)\zeta + (x_4 - x_1)\psi, \\ y &= y_1 + (y_2 - y_1)\xi + (y_3 - y_1)\zeta + (y_4 - y_1)\psi, \\ z &= z_1 + (z_2 - z_1)\xi + (z_3 - z_1)\zeta + (z_4 - z_1)\psi, \end{aligned} \tag{2.21}$$

This transformation permits one corner of the element to be orthogonal in each direction of the new space (ξ, ζ, ψ). The simple shape of the element and the orthogonality of the element in the natural coordinate system permits simple derivations of the shape functions in the new space. Therefore reducing the complexity of the computational task which is the determination of the Jacobian matrix. The above 3-dimensional coordinate transformation enables to define the Jacobian matrix $\mathbf{J}$ using the chain rule:

$$\begin{bmatrix} dx \\ dy \\ dz \end{bmatrix} = \begin{bmatrix} \frac{\partial x}{\partial \xi} & \frac{\partial x}{\partial \zeta} & \frac{\partial x}{\partial \psi} \\ \frac{\partial y}{\partial \xi} & \frac{\partial y}{\partial \zeta} & \frac{\partial y}{\partial \psi} \\ \frac{\partial z}{\partial \xi} & \frac{\partial z}{\partial \zeta} & \frac{\partial z}{\partial \psi} \end{bmatrix} \begin{bmatrix} \partial \xi \\ \partial \zeta \\ \partial \psi \end{bmatrix} = \mathbf{J}^T \begin{bmatrix} \partial \xi \\ \partial \zeta \\ \partial \psi \end{bmatrix} \tag{2.22}$$

The shape functions of a linear tetrahedron in the natural coordinate system are given by:

$$\Psi_1^t(\xi,\zeta,\psi) = 1-\xi-\zeta-\psi,$$
$$\Psi_2^t(\xi,\zeta,\psi) = \xi,$$
$$\Psi_3^t(\xi,\zeta,\psi) = \zeta,$$
$$\Psi_4^t(\xi,\zeta,\psi) = \psi, \quad (2.23)$$

For a more comprehensive explanation on the rules defining the iso-parametric shape functions, the reader is referred to Zienkiewicz & Taylor (2005). The shape functions allow to solve the partial differential equations in the natural orthogonal coordinate system. The gradient of a function $f(x,y,z)$ in the natural coordinate system takes the form:

$$\nabla^t f = \begin{bmatrix} \frac{\partial f}{\partial \xi} & \frac{\partial f}{\partial \zeta} & \frac{\partial f}{\partial \psi} \end{bmatrix}^T \quad (2.24)$$

The derivatives of the function in the new coordinate system are determined using the transverse of the Jacobi:

$$\begin{bmatrix} \frac{\partial f}{\partial \xi} \\ \frac{\partial f}{\partial \zeta} \\ \frac{\partial f}{\partial \psi} \end{bmatrix} = \begin{bmatrix} \frac{\partial x}{\partial \xi} & \frac{\partial y}{\partial \xi} & \frac{\partial z}{\partial \xi} \\ \frac{\partial x}{\partial \zeta} & \frac{\partial y}{\partial \zeta} & \frac{\partial z}{\partial \zeta} \\ \frac{\partial x}{\partial \psi} & \frac{\partial y}{\partial \psi} & \frac{\partial z}{\partial \psi} \end{bmatrix} \cdot \begin{bmatrix} \frac{\partial f}{\partial x} \\ \frac{\partial f}{\partial y} \\ \frac{\partial f}{\partial z} \end{bmatrix} \quad (2.25)$$

which in the shorthand notation reads:

$$\nabla^t f = \mathbf{J}\nabla f \quad (2.26)$$

Therefore the gradient of a function $f(x,y,z)$ in the original coordinate system can be expressed in the new coordinate system:

$$\nabla f = (\mathbf{J})^{-1} \nabla^t f = \mathbf{\Lambda} \nabla^t f, \tag{2.27}$$

where $\mathbf{\Lambda}$ is the inverse Jacobian matrix.

Therefore the Jacobian must be determined before an approximation of the solution $\mathbf{u}$ can be computed. The computation of the Jacobian reads:

$$\mathbf{J} = \begin{bmatrix} \frac{\partial x}{\partial \xi} & \frac{\partial y}{\partial \xi} & \frac{\partial z}{\partial \xi} \\ \frac{\partial x}{\partial \zeta} & \frac{\partial y}{\partial \zeta} & \frac{\partial z}{\partial \zeta} \\ \frac{\partial x}{\partial \psi} & \frac{\partial y}{\partial \psi} & \frac{\partial z}{\partial \psi} \end{bmatrix} = \begin{bmatrix} \frac{\partial \Psi_1}{\partial \xi} & \frac{\partial \Psi_2}{\partial \xi} & \cdots & \frac{\partial \Psi_N}{\partial \xi} \\ \frac{\partial \Psi_1}{\partial \zeta} & \frac{\partial \Psi_2}{\partial \zeta} & \cdots & \frac{\partial \Psi_N}{\partial \zeta} \\ \frac{\partial \Psi_1}{\partial \psi} & \frac{\partial \Psi_2}{\partial \psi} & \cdots & \frac{\partial \Psi_N}{\partial \psi} \end{bmatrix} \cdot \begin{bmatrix} x_1 & y_1 & z_1 \\ x_2 & y_2 & z_2 \\ \vdots & \vdots & \vdots \\ x_N & y_N & z_N \end{bmatrix} \tag{2.28}$$

with N the number of nodes or shape functions in each iso-parametric elements.

The Neumann boundary condition is represented by the normal derivative $\partial \mathbf{n}$ of ϕ in the outward direction to the boundary Γ_N. Assuming vanishing normal derivatives the condition can be re-written as:

$$g_N = \frac{\partial \phi}{\partial \mathbf{n}} = \nabla \phi \cdot \mathbf{n} = 0 \tag{2.29}$$

Using the example of the Helmholtz wave equation, the discrete weak form 2.15 can be expressed as a system of matrices. Each tetrahedral element of N nodes can be expressed in the natural coordinate system using the following reformulation of element matrices $\mathbf{C}$, $\mathbf{D}$, $\mathbf{F}$:

$$\begin{aligned} \mathbf{C}_{ij} &= \int_\Omega -(\nabla \Psi_i) \cdot (\nabla \Psi_j) \\ &= \det(\mathbf{J}) \int_0^1 \int_0^{1-\xi} \int_0^{1-\xi-\zeta} -(\mathbf{\Lambda} \nabla^t \Psi_i^t) \cdot (\mathbf{\Lambda} \nabla^t \Psi_j^t) d\psi d\zeta d\xi, \end{aligned} \tag{2.30}$$

and similarly:

$$\mathbf{D}_{ij} = \int_{\Omega} \Psi_i \Psi_j \mathrm{d}\Omega = \det(\mathbf{J}) \int_0^1 \int_0^{1-\xi} \int_0^{1-\xi-\zeta} \Psi_i^t \Psi_j^t d\psi d\zeta d\xi, \tag{2.31}$$

$$\mathbf{F}_j = \int_{\Omega} \Psi_j \mathrm{d}\Omega = \det(\mathbf{J}) \int_0^1 \int_0^{1-\xi} \int_0^{1-\xi-\zeta} \Psi_j^t d\psi d\zeta d\xi, \tag{2.32}$$

The problem of the Helmholtz wave equation on a discrete domain can be solved using the following system of equation for each element comprised of N nodes :

$$\sum_{i=1}^{N} \phi_i \left[\mathbf{C}_{ij} + k^2 \mathbf{D}_{ij}\right] = f\mathbf{F}_j - \sum_{m=1}^{N} g_{D,m} \left[\mathbf{C}_{jm} + k^2 \mathbf{D}_{jm}\right], \quad \text{for } j = 1, \ldots, N \tag{2.33}$$

2.4 Scaling factors & multigrid method

Direct solvers which solve the differential equations on the whole matrix are relatively fast for small problems with few elements. Large problems with relatively high amount of finite elements have therefore more degrees of freedom and can take a relatively high amount of memory. This is essentially true for large 3-dimensional problems. In finite element analysis keeping the memory footprint low is essential to solve a given problem fast. When high amounts of memory are required, the speed at which the algorithm can run is limited by the hardware used. A lower memory footprint requires fewer memory operations by the hardware. Decomposing the problem into smaller ones is effective in reducing the complexity of a large problem which would be otherwise difficult to solve.

In this study, the software Comsol Multiphysics® was set to use the sparse direct solver PARDISO (Parallel Sparse Direct And Multi-Recursive Iterative Linear Solvers) (Kuzmin *et al.*, 2013; Schenk & Gärtner, 2004) which provides an effective method to solve linear systems of equations. This method was used in conjunction with a multigrid algorithm described in Section 2.4.2.

2.4.1 Scaling factors

When the coefficients of the matrices have a high order of magnitude or have values close to zero it might increase the amount of required memory. This is especially true in this study as displacements are of the order of the micrometer: 10^{-6} m or below and pressures are in the order of 10^4 Pa or above. The latter requires the use of scaling factors.

The software might use default scaling factors, which are automatically estimated from the input parameter. Among those estimated scaling factors are those for each scalar fields computed as matrices by the solver. A wrongly estimated scale factor might easily prevent any convergence to a solution. The closer the values in the matrices are to 1, the faster the convergence and the less iterations will be necessary to compute a solution within the tolerance. These scales

in this study were set manually to allow faster convergence. For example, since the expected pressure field p had an order of magnitude of 100 kPa or 10^5 Pa, the scale factor for the pressure field were set to 10^5 and all values of the pressure field matrix were divided the factor during computation. Similarly, since that displacement field has values of the order of a tenth of micrometer, the displacement field in this study u of the materials were divided by a factor of 10^{-7} in the solver settings.

2.4.2 Multigrid solver

The solving method can be direct or iterative. Direct methods find an approximation of the solution $A^{-1}b = u$ by matrix factorisation in a number of operations that depend on the number of unknowns coefficients. Factorisation is computationally expensive, but once it has been computed it is relatively inexpensive to solve for new right-hand sides . The approximate solution will be available only when all operations required by the factorisation algorithm are executed.

Iterative methods begin with an approximated initial guess and then proceed to improve it by a succession of iterations. This means that, contrary to direct methods, the iterative algorithm can be stopped at any iteration to obtain access to the approximate solution . Stopping the iterative process too early will result in an approximate solution with poor accuracy.

The 'geometric multigrid' algorithm available in Comsol Multiphysics® enables one to solve the lower element order initially using an iterative solver. The shape functions' order is lowered by one. The main idea behind multigrid methods is to use the smoothing property, spatial aliasing, and the residual correction to the advantage of convergence.

When using iterative methods, the convergence is slower for a low wavenumber and quicker for higher wavenumber for a given field due to an intrinsic limitation of iterative methods. Because oscillatory components from high wavenumbers are

efficiently eliminated from the error, while the smoother variations from lower wavenumbers prevail and are left almost unchanged at every iteration, the convergence is stalling.

To accelerate the convergence rate of iterative methods, multigrid methods were developed (Briggs *et al.*, 2000). If h is the grid spacing of the mesh, then on a mesh with an increased grid spacing of $2h$, lower wavenumbers will appear more oscillatory. Therefore when the convergence is stalling it becomes interesting to use a coarser grid with a larger grid spacing than the initial grid spacing h. However, due to spacial aliasing, higher wavenumbers on a coarser grid will have their solution accuracy drop. The idea of multigrids is to solve long waves on a coarser meshes and short waves on a finer meshes. Solutions found on a coarser mesh can then be smoothed out onto the finer mesh by interpolation (Zienkiewicz & Taylor, 2005). As described at the end of Section 2.3.4, the characteristic length h can be varied by a change in element order or by a change in the number of elements used. In this study, quadratic elements had their order reduced to solve the problem on a coarser discretised domain Ω_{2h}. In other words, the multigrid method was restricted to the variation of element order and no change in the number of element was required.

The multigrid algorithm operates using a method to iteratively update the solution. This achieved using successive *restrictions* to a coarser mesh Ω_{2h} and *prolongations* to the original mesh Ω_h. This method is called *the coarse grid correction algorithm* (Marra, 2013).

Figure 2.7 is an overview of the processes involved in the coarse grid correction algorithm.

First, the procedure starts computing an initial approximation v of the searched solution u with a nested iteration procedure: A first solution of $Av = b$ is estimated on the coarse mesh Ω_{2h} to obtain an initial guess of the solution for Ω_h. Then on Ω_h to obtain a finial approximation of the solution. However convergence might stall on the finest mesh due to the lower wavenumbers. This is overcome

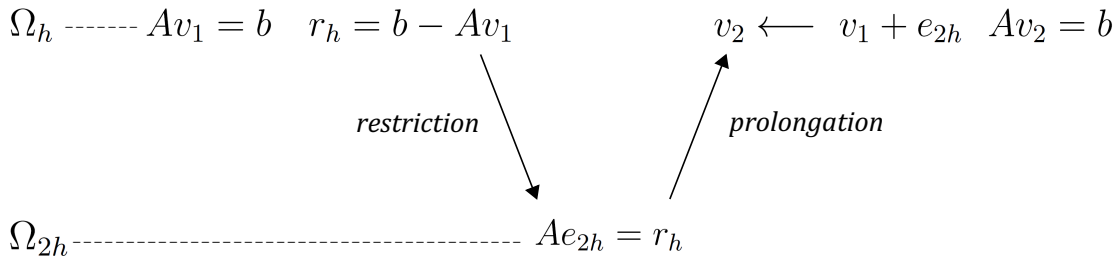

Figure 2.7: The multigrid solver iteration procedure on the initial mesh Ω_h and the coarser mesh Ω_{2h}. A single iteration involves a restriction on Ω_{2h} of the initial residual r_h to find the error e_{2h}, followed by a prolongation to update the solution v_1 to v_2

by the use of the residual equation.

Then, during the iterative method, approximate solutions v_n are computed. To find how far an approximate solution v_n is from the solution u the error $e = |u - v_n|$ is estimated to find out if the iterative method is able to converge v_n towards u. Since u is unknown, e is unknown too, but the residual can be computed with $r = b - Av$. One can find after some algebra the residual equation:

$$Ae = r, \tag{2.34}$$

Using 2.34 e can be computed and the initial approximation of v can be improved into v_1 on the mesh Ω_h. After a few iterations, if the solution has not converged enough, the residual r_h is estimated on Ω_h and the error e_{2h} is computed on a coarser mesh Ω_{2h} with r_h (restriction). Then v_1 can be improved into a better approximation of the solution v_2 on Ω_h (prolongation) using e_{2h}. The iterative method is stopped when the error e meets a set criterion.

2.5 Summary

This chapter discussed in Section 2.1 how the surface rheology of amphiphile molecules is related to the bending mechanisms existing in the microbubble coating. For this particular behaviour, as discussed in Section 2.2, a special case of the plate theory, the thin shells, for which a geometrically nonlinear theory was necessary to allow finite displacements but small strains while retaining the assumption of infinitesimal strain–stress necessary for Hooke's law. In Section 2.2.1, the conditions of compatibility were explained and presented the solutions found to enable the radial oscillations and the occurrence bending moments in spherical shells to model the coating of microbubbles with the finite element method. In Section 2.3, some basics of the finite element method have been introduced with the inhomogeneous Helmholtz wave equation. Finally, in Section 2.4, the chosen solver and the multigrid algorithm that allows a faster convergence to a solution were presented.

Chapter 3

A FE model of a microbubble with a viscoelastic shell

3.1 Introduction

A finite element model of a gas bubble with a solid shell governed by a generalised Maxwell model also refered as the Maxwell-Wiechert model is proposed to study the oscillation amplitudes and modes observed for phospholipid coated microbubbles. Microbubble shell material have been found to possess elastic and viscous properties (Hoff, 2001). Doinikov & Dayton (2007) suggested a viscoelastic Maxwell model may be a good approximation to model the rheological properties of lipid shells rather than simple viscous fluid or elastic material. Although the phospholipidic and polyethylene glycol chains mixtures coating some microbubble type (e.g. SonoVue®, Definity, Micromarker) might also possess the rheological property of shear thinning and strain-softening (Doinikov *et al.*, 2009a). Here, the generalised Maxwell model is used to model a linear approximation of the material's nonlinear behaviour (Dai & Jazar, 2012), which enables a relative good convergence rate during solving.

3.2 Methods: a FE model of a microbubble with a viscoelastic shell

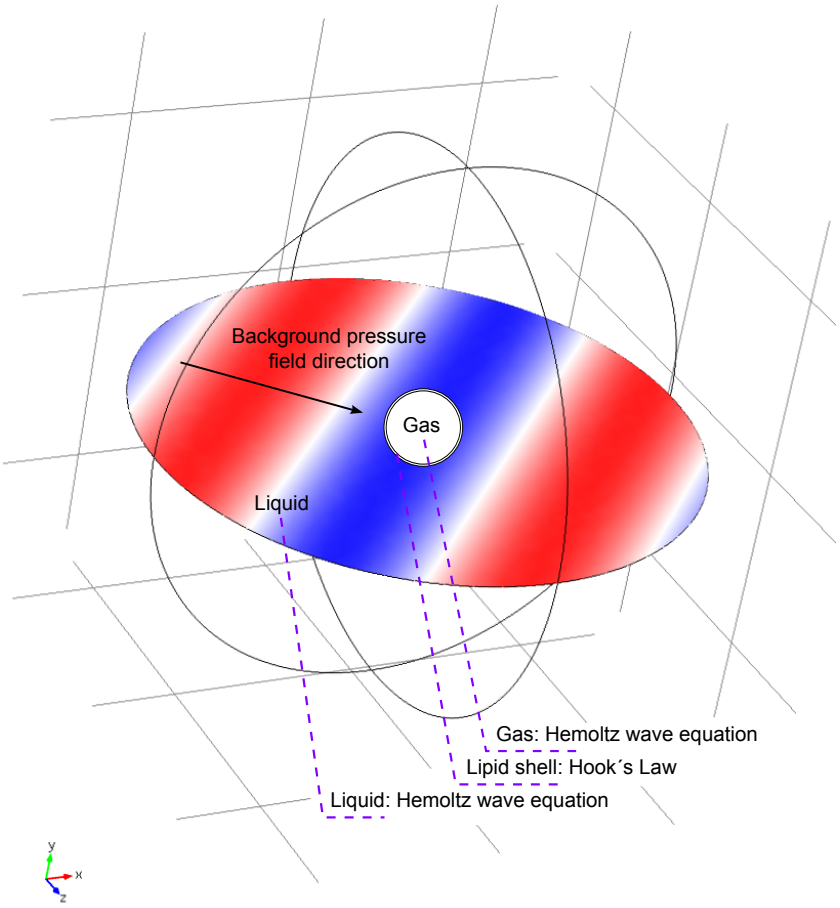

Figure 3.1: Unscaled schematic view of a modelled coated bubble in Comsol Multiphysics®

3.2.1 The wave equation field in fluids

The propagation of sound waves in the mediums is described by the inhomogeneous Helmholtz wave equation for linear elastic wave propagation in Blackstock (2000) and Temkin & Temkin (1981):

$$\nabla \cdot \left(\frac{-1}{\rho_m} \nabla p_t \right) - \frac{k^2 p_t}{\rho_m} = 0, \tag{3.1}$$

where p_t is the total acoustic pressure, c_m is the longitudinal speed of sound in the medium, and ρ_m is the density of the medium. k is the wave number defined as the angular frequency ω over the speed of sound c_m.

The attenuation factor of pure water as a function of temperature has been studied by Pinkerton (1949). For an ideal plane wave, absorption due to the viscosities and the scattering are the only phenomena occurring during the propagation of sound waves. The amplitude attenuation coefficient α is the sum of the scattering and absorption. For pure water it is frequency dependent and thus $\alpha = \alpha_0 f^2$, where α_0 is the temperature dependent coefficient often expressed in dB.cm^{-1}.MHz^{-2} and the frequency f is in megahertz (Cobbold, 2007). Pinkerton found $\alpha_0 = 21.97 \times 10^{-4}$ dB.cm^{-1}.MHz^{-2} for water at $20°C$. For example at 5MHz the attenuation of water at $20°C$ is α= 0.055 dB.cm^{-1}, whereas at 30 MHz it is 1.98 dB.cm^{-1}. The diameter of the medium considered being 1400 µm, the maximum attenuation across the domain would be 0.0077 dB at 5 MHz and 0.2772 dB at 30 MHz which is sufficiently low to neglect the viscous contribution to the wave amplitude. The viscous terms, the shear viscosity and the bulk viscosity, generally denoted μ and μ_B respectively are therefore neglected. This choice is appropriate as the calculated viscous losses occur over distances much longer than the diameter of the medium surrounding the microbubble at the frequencies considered in this study.

At low acoustic pressure, where microbubbles are driven in a non-inertial (stable) cavitation regime, the host fluid viscosity and compressibility can be neglected since in the present case the dominant dampening mechanism for the

estimation of the coating displacement is the viscosity of the coating.

The total acoustic pressure field p_t is defined as the sum of the scattered pressure field p_s and the background pressure field p_b:

$$p_t = p_s + p_b, \tag{3.2}$$

where p_s is the unknown variable solved by the partial differential equations. All pressures are defined on the scalar field $\mathbf{x}$ in form of a harmonic wave $p = p(\mathbf{x})e^{i\omega}$. Note the dependence on ω is implicit. The background pressure field is defined as:

$$p_b = p_0 e^{-i\mathbf{x}\cdot\mathbf{k}}, \tag{3.3}$$

where p_0 is the wave pressure amplitude and the planar wave field travels in the direction $\mathbf{k}$ with $|\mathbf{k}| = \omega/c_m$, where ω is the angular frequency of the wave field.

In 3.1 and 3.3 c_m and ρ_m are dependent on their coordinates $\mathbf{x}$ and can be complex valued if they are dependent on a complex valued scalar field, *e.g.* the total pressure field p_t.

Gas Model

The gas being a fluid, the Helmholtz equation 3.1 models the acoustic wave propagation; however, in this case, the velocity of the gas c_g and the density of the gas ρ_g are dependent on the absolute pressure p_A. The ideal gas law is a good approximation for the thermodynamic properties of gasses at wide ranges of pressures and temperatures but not undergoing phase transitions. At each point of the acoustic field, the density is governed by the ideal gas law:

$$\rho_g = \frac{p_A}{R_s T} = \frac{p_A M_n}{RT} \tag{3.4}$$

where $p_A = p_t + P_0$ is the absolute pressure field inside the gas bubble, with P_0 is the hydrostatic pressure with a value of 101.325 kPa throughout the study, M_n is the mean molar mass in kg.mol^{-1}, T is the ambient temperature, R is the

universal gas constant in J.mol^{-1}.K^{-1} and $R_s = \frac{R}{M_n}$ is the specific gas constant in J.kg^{-1}.K^{-1}. ρ_g is complex valued as it is dependent on the total pressure field p_t.

The velocity of sound waves in the gas for an adiabatic process is given by:

$$c_g = \sqrt{\gamma R_s T}, \tag{3.5}$$

where γ is the polytropic gas index.

3.2.2 The viscoelastic material

The dilational rheological properties of interfacial films such as Lysozyme and polyethylene glycol 2000, Dipalmitoylphosphatidycholine (DPPC) monolayer at a gas/water interface have been observed by Saulnier *et al.* (2001) and Monteux *et al.* (2004) under ramp type or sinusoidal perturbations. A standard linear solid (SLS) model of Maxwell form was found to be able to characterise the response of the monolayers and permit the measurement of the parameters. In this Section, the generalised Maxwell model proposed in Section 3.1, will be limited to the use of a generalised Maxwell model with a single dashpot-spring branch which is equivalent to the SLS of Maxwell form.

The propagation of the sound waves in the shell material is described by the Hooke's law for isotropic materials (Landau & Lifshitz, 1987; Morse, 1986):

$$\rho_l \omega^2 \mathbf{u} - \nabla \cdot \mathbf{s} = \mathbf{F} e^{i\theta}, \tag{3.6}$$

where $\mathbf{s}$ is the total stress tensor: $\mathbf{s} = -p\mathbf{I} + s_d$ and $\mathbf{I}$ is the second order identity tensor, s_d is the stress deviator, p is the pressure within the material, $\mathbf{F}$ is the external force (pressure load) defined in equation3.29 with θ the phase. Note the displacement term $\mathbf{u}$ is present in equation 3.6, but not in the equations 3.1. Therefore, the displacement is solved only in the solids. The temperature effects are neglected, and thus the pressure is computed as:

$$p = -K\epsilon_{vol}, \tag{3.7}$$

where the bulk modulus K is defined as : $\frac{2G(1+\nu)}{3(1-2\nu)}$, and the volumetric strain ϵ_{vol} is given by the following relations:

$$\epsilon_{vol} = trace(\epsilon), \tag{3.8}$$

where ϵ is the strain tensor,

$$\epsilon = \frac{1}{3}\epsilon_{vol} + \epsilon_d, \tag{3.9}$$

where ϵ_d is the strain deviator tensor.

For a time dependent analysis, the general linear dependence of the stress deviator s_d on the strain history ϵ_d can be expressed by the hereditary integral:

$$s_d = 2\int_0^t \Gamma(t-t')\frac{\partial \epsilon_d}{\partial t'}dt', \tag{3.10}$$

where t is the time, t' is the time delay and $\Gamma(t)$ is the relaxation shear modulus function used to model the stress evolution of a material held at a constant strain ϵ_0 and which can be approximated in a Prony series:

$$\Gamma(t) = G + \sum_{m=1}^{N} G_m e^{-t/\lambda_m}, \tag{3.11}$$

where G_m is the shear modulus and λ_m is the relaxation time constant of each m spring and dashpot pairs of the generalised Maxwell model represented in Figure 3.2.

The relation between the stress deviator and strain deviator is expressed similarly to 3.10 and 3.11 by:

$$s_d = 2G\epsilon_d + \sum_{m=1}^{N} 2G_m q_m, \tag{3.12}$$

where q_m is a symmetric tensor characterising the extension of the m branch. q_m related to the relaxation time by partial differential equation:

$$\dot{q_m} + \frac{1}{\lambda_m}q_m = \dot{\epsilon_d}, \tag{3.13}$$

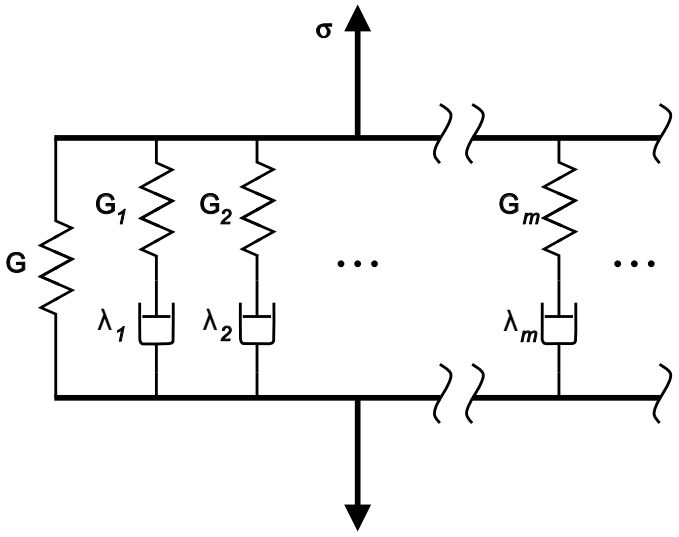

Figure 3.2: Generalised Maxwell model

The FE model implements the generalized Maxwell model with a single branch and therefore the relaxation shear modulus function is expressed as: $\Gamma(t) = G + G_1 e^{-t/\lambda_1}$, where $G = E/(2(1+\nu))$ and the non-equilibrium shear modulus $G_1 = \eta_1/\lambda_1$. At $t = 0$, we define $G_{t0} = G + G_1$ the initial total shear modulus.

The hypothesis for the FE model is that the elastic and viscous properties of the interfacial monolayer can be modelled with an SLS of Maxwell form. In the FE model the shell is modelled by a material with a finite thickness. As mentioned by Church (1995) the forces exerted by the shell on the gas bubble can effectively replace the surface tension.

In Figure 3.3 the SLS of Maxwell form is represented . It is constituted of two parallel branches:

1. The equilibrium shear modulus G represented by a Hookean spring;

2. The non-equilibrium shear modulus G_1, the relaxation time λ_1 and its viscosity $\eta_1 = G_1\lambda_1$ represented by a Hookean spring in series with a Newtonian dashpot.

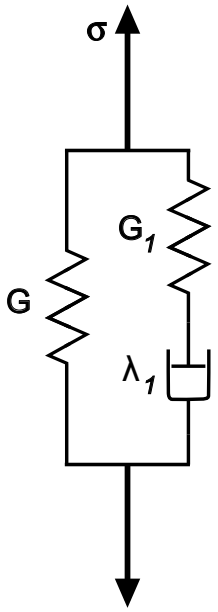

Figure 3.3: Standard Linear Solid of Maxwell form

As seen in Figure 3.3, the two branches share the same stress σ which can be formulated by the mathematical relation:

$$\sigma = \sigma_0 + \sigma_1, \tag{3.14}$$

, where σ_0 is the stress in the Hookean spring (G), and σ_1 is the stress in the Hookean spring (G_1) in series with the Newtonian dashpot (λ_1).

$$\sigma_0 = G\epsilon, \tag{3.15}$$

where ϵ

$$\dot{\epsilon} = \frac{\dot{\sigma_1}}{G_1} + \frac{\sigma_1}{\eta_1}, \tag{3.16}$$

By applying a constant strain ϵ_0 to the model through a Heaviside function $H(t)$ yields the equation for stress relaxation (Dai & Jazar, 2012):

$$\epsilon = \epsilon_0 H(t), \tag{3.17}$$

of which the Laplace transform is:

$$\hat{\epsilon} = \frac{\epsilon_0}{s}, \tag{3.18}$$

where s — a complex number— is the Laplace variable to allow the calculus in the s-domain.
The constitutive equation of the SLS of Maxwell form can be found by substituting 3.15 into 3.14, taking the Laplace transform of 3.14-3.16, and solving $\hat{\sigma}$:

$$\frac{\hat{\sigma}}{\hat{\epsilon}} = G + \frac{s\eta_1 G_1}{s\eta_1 + G_1}, \tag{3.19}$$

The frequency analysis of the SLS system can be achieved using the frequency decomposition:

$$s_d = real(\hat{s_d} e^{iwt}), \tag{3.20}$$

$$\epsilon_d = real(\hat{\epsilon_d} e^{iwt}), \tag{3.21}$$

With the above decomposition and rewriting equations 3.12 and 3.13 gives the relation:

$$\hat{s_d} = 2\bar{G(\omega)}\hat{\epsilon_d}, \tag{3.22}$$

Using the constitutive equation 3.19 and substituting $\hat{\epsilon}$ and $\hat{s}$ respectively with $\hat{\epsilon_d}$ and $\hat{s_d}$ lets to write the transfer function:

$$\bar{G(\omega)} = G + \frac{i\omega\eta_1 G_1}{i\omega\eta_1 + G_1}, \tag{3.23}$$

where i is the complex imaginary unit.

$\bar{G(\omega)}$ can be decomposed into its corresponding real and imaginary parts:

$$\bar{G(\omega)} = G'(\omega) + iG''(\omega), \tag{3.24}$$

Using the relation $\eta_1 = G_1\lambda_1$, if the temperature effects are neglected, one can find:

$$G'(\omega) = G + \frac{G_1\omega^2\lambda_1^2}{1+\omega^2\lambda_1^2} \tag{3.25}$$

$$G''(\omega) = \frac{G_1\omega\lambda_1}{1+\omega^2\lambda_1^2} \tag{3.26}$$

The expression 3.25 and 3.26 are known respectively as the storage and loss modulus. By observing the variable ω, the theoretical mechanism of the shell material can be analysed.

if the monolayer is strained fast enough $\omega \gg \lambda^{-1}$
then $\lim_{\omega\to+\infty} G'(\omega) = G + G_1$
and $\lim_{\omega\to+\infty} G''(\omega) = 0$

The system, in this case, has no time to relax and the response is a purely elastic regime[1]. The material is consistent with the rheological behaviour of a Langmuir trough, by the fact that in this regime the molecules do not have time to redistribute and thus none or limited lateral diffusion may take place.

Conversely, if the strain is slow enough $\omega \ll \lambda^{-1}$
then $\lim_{\omega\to0} G'(\omega) = G$
and $\lim_{\omega\to0} G''(\omega) = \lambda_1 G_1$

The diffusion can take into effect, and some or all molecules of the Langmuir trough have time to redistribute completely or partially. In this case some stress is relaxed by viscous dissipation.

The transfer function can be rewritten into:

$$G(\bar{\omega}) = G\frac{1+i\omega/\omega_z}{1+i\omega/\omega_p}, \tag{3.27}$$

[1]From the relation $E = 2G(1+\nu)$ in material science defined by the Hook's law for a homogeneous material, the same transfer function can be written for the Young's modulus E also called the elastic modulus. The mathematical relations and equations are written with the shear modulus to keep consistency.

where ω_p and ω_z are respectively the pole and zero of the transfer function, and $\omega_p = \frac{G_1}{\eta_1}$, $\omega_z = \frac{GG_1}{\eta_1(G+G_1)}$.

and the magnitude:

$$|G(\bar{\omega})| = G\frac{\sqrt{1+(\omega/\omega_z)^2}}{\sqrt{1+(\omega/\omega_p)^2}}, \tag{3.28}$$

The overall response of the SLS system is shown in Figure 3.4 where the comparison of the theoretical transfer function with analytical solution from the model for the following parameter is made. $G = \frac{E}{2(1+\nu)}$ and $G_1 = \frac{\eta_1}{\lambda_1}$ with $E =$ 67 MPa, η_1=0.7 Pa.s and λ=0.06 µs :

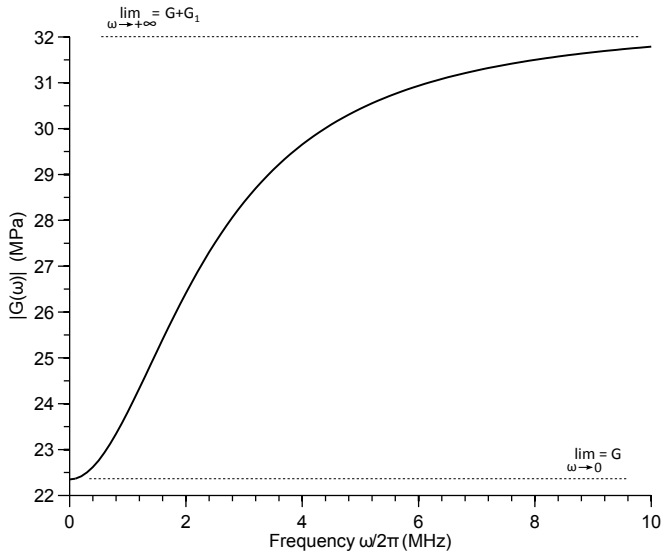

Figure 3.4: Theoretical response of the SLS system of Maxwell form calculated by 3.28. $G = \frac{E}{2(1+\nu)}$ and $G_1 = \frac{\eta_1}{\lambda_1}$ with $E = 67$ MPa, η_1=0.6 Pa.s, λ_1=0.06 µs and $\nu = 0.499$.

In Figure 3.4, low insonation frequencies ($\leq$ 0.5 MHz), the material is put under low loading pressure rates and has time to relax; the shear modulus tends to the value G. Otherwise, at high frequencies ($\geq$10 MHz) the material undergoes high shear rates and cannot relax, the shear modulus tends to the value $G + G_1$.

3.2.3 Acoustic-Solid Interactions

The acoustic-sold interactions are determined by the pressure load $\mathbf{F}$ —previously seen in equation 3.6— and the structural acceleration a on the solid-fluid boundaries. The acoustic pressure exerts a normal load on the solid boundary where $\mathbf{n}$ is the outward-pointing unit normal vector seen from the inside of the solid domain (Ihlenburg, 1998):

$$\mathbf{F} = \mathbf{n}p_t, \tag{3.29}$$

where p_t is the pressure within the gas or the liquid medium (see equations 3.4 and 3.2).

This pressure load is equal to the normal stress component of the material and defines the first boundary condition:

$$\mathbf{s} \cdot \mathbf{n} = \mathbf{n}p_t, \tag{3.30}$$

where $\mathbf{s}$ is the material stress tensor.

The normal acceleration for the acoustic pressure on the boundary is equal to the acceleration a based on the second derivatives of the structural displacement $\mathbf{u}$ with respect to time:

$$a = \mathbf{n} \cdot \ddot{\mathbf{u}}. \tag{3.31}$$

The acceleration a in the acoustic field at the material boundary is defined as the normal component of the total pressure gradient:

$$\mathbf{n} \cdot \left(-\frac{1}{\rho_l} \nabla p_t \right) = \mathbf{n} \cdot \ddot{\mathbf{u}}. \tag{3.32}$$

3.2.4 The perfectly matched layers

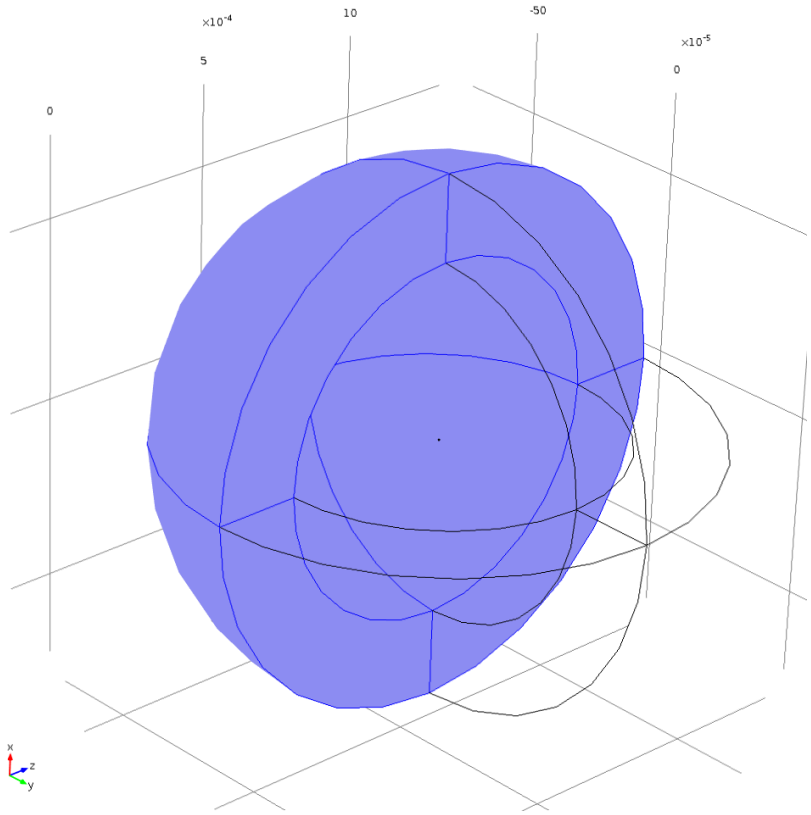

Figure 3.5: A scaled view of the model in Comsol Multiphysics®. Some selected PML domains are highlighted in blue.

To absorb outgoing waves in the frequency domain, perfectly matched layers (PMLs) are drawn domains surrounding the spherical liquid domain as shown in Figure 3.5. The PMLs have the same material properties, but are virtual domains that have scaled coordinates to mimic a much bigger volume. By doing so, a PML is strictly not a boundary condition but an additional domain that absorbs the incident radiation without producing reflections. It provides good performance for wide range of incidence angles and it is not particularly sensitive to the shape of the wave fronts. The implementation of PMLs in Comsol Multiphysics® enables the eventual calculation of the far-field scattered pressure.

The PML formulation can be deduced from the Helmholtz equations by introducing a complex-valued coordinate transformation under the additional requirement that the wave impedance should remain unaffected (Jin *et al.*, 2002).

To apply a coordinate scaling in the direction ξ to a layer of virtual domains surrounding the physical region of interest, the following transformation inside the PML region is used:

$$\xi' = \text{sign}(\xi - \xi_0)|\xi - \xi_0|^n \frac{L}{\delta\xi^n}(1 - i), \tag{3.33}$$

where the parameters ξ_0 and $\delta\xi$ have their values determined from the drawn geometry.

For each orthogonal absorbing coordinate direction, the software automatically determines the coordinate of the inner PML boundary ξ_0, and the drawn width of the PML, $\delta\xi$. The PML scaling factor, $L/\delta\xi$ and the PML order n, are parameters for each PML domain. The default value for n is 1, which gives linear scaling of the elements, that is adapted for most cases. The default value for L is one wavelength, $\lambda = c_{ref}/f$, which is appropriate for acoustic wave propagating along the absorbing coordinate direction, ξ. To preserve the attenuation level for obliquely incident waves, the PML width must be adjusted: for a wave with a wave vector $\mathbf{k}$, the optimal value for L in the coordinate direction ξ is $2\pi/|\mathbf{k} \cdot \mathbf{e}_\xi| = \lambda/|cos(\theta)$, where $\mathbf{e}_\xi$ is a unit vector in the ξ direction, and θ is the angle between $\mathbf{k}$ and $\mathbf{e}_\xi$.

3.3 Calibration Method

Before modelling the effect of microbubbles in the vicinity of a soft membrane mimicking the situation enabling sonoporation, the oscillation amplitude and the resonance frequency must be calibrated. There are two different types of experimental data available in the literature that can provide the necessary information on the microbubbles characteristics for the calibration.

The first common experience used to collect the information is the measurement of the attenuated sound pressure that travelled through a cloud of microbubbles. Similarly the scattered pressure can be measured. Sarkar *et al.* (2005) used this method to find the shell parameters for their Rayleigh-Plesset like equations.

Another, more direct method, is the optical measurement of the radial motion of single microbubbles with a high speed camera. The two most common imaging techniques used to study microbubbles are streak imaging (Morgan *et al.* (2000)) and sequential high-speed imaging (Marmottant *et al.* (2006)). While streak imaging only provides one-dimensional time-frames, sequential high-speed imaging provides two-dimensional time-frames essential to study non-spherical bubble deformations. The former should be restricted to the study of spherical bubble dynamics at low mechanical index, while the latter enables the study of non-spherical bubble deformations.

In this Chapter the qualitative changes of the viscosity η, relaxation time λ, the elasticity E to the resonance frequency and the amplitude oscillations will be presented. Firstly the resonance then the amplitude will be compared to experimental results of SonoVue® from the literature.

The determination methods for the amplitude displacements and the resonance frequency of a microbubble are described here. Firstly, a bubble does not necessarily exhibit its maximal radial displacement at a same specific phase across a studied range of excitation frequencies. Therefore, the phase θ of the acoustic field at which the microbubble is insonified at should be taken into account. For

example, a microbubble can oscillate out of phase with the acoustic field. In this case, the maximal expansion of the shell material does not occur when the lowest pressure of the field hits the microbubble. Fortunately, since complex scalars are used, the calculation of the maximal displacement at a unique surface point i, is the vector norm of the Euclidean complex scalar U, which any phase θ, is expressed as:

$$||U_i|| = \sqrt{\mathbb{R}\left[\mathbf{u}e^{i\theta}\right]^2 + \mathbb{R}\left[\mathbf{v}e^{i\theta}\right]^2 + \mathbb{R}\left[\mathbf{w}e^{i\theta}\right]^2}, \qquad \forall\ \theta \in \{0, 2\pi\}, \tag{3.34}$$

where $U^{\mathrm{T}} = \{\mathbf{u}, \mathbf{v}, \mathbf{w}\}$ and $\mathbf{u}$, $\mathbf{v}$, $\mathbf{w}$ are the complex displacement scalars of the vector space $\mathbf{e_x}$, $\mathbf{e_y}$, $\mathbf{e_z}$, and $\mathbb{R}$ represents the real part of a number. $||U_i||$ is the magnitude of displacement at a unique surface point.

Secondly, since the shell displacements are not necessarily uniform across the bubble surface, an average of the displacement of all the points on the surface is taken. dS_{avg} is the surface average displacement of the microbubble coating by calculating the average of $||U_i||$ over all mesh points i (n total nodes) belonging to the microbubble surface S:

$$\mathrm{dS}_{avg} = \frac{1}{n}\sum_{i=1}^{n} ||U_i||, \qquad \forall i \in S, \tag{3.35}$$

The maximal displacement d_{max} is found by calculating the maximum of dS_{avg} across the frequency range f:

$$d_{max} = \max\left\{\mathrm{dS}_{avg,f}\right\}, \tag{3.36}$$

The resonance frequency f_0 is found by:

$$\text{find } f_0 \in f \text{ such that :} \qquad \mathrm{dS}_{avg,f_0} = d_{max}, \tag{3.37}$$

3.3.1 Resonance

The resonance frequencies of microbubbles in the FE model were found by estimating f_0 in the equation 3.37 of microbubbles ranging in size of 1.25 µm to 3 µm. The estimated resonance frequencies were then compared with the experimental data of SonoVue® resonance frequencies published by Van Der Meer *et al.* (2004). To allow a comparison with the identical acoustic pressure of 130 kPa was used in the FE model. The published experimental data was reproduced by measuring the individual data points that appeared in the Figure 3. p.344 of the journal and are represented in this Section by an asterisk (∗).

Qualitative changes of Young's modulus E

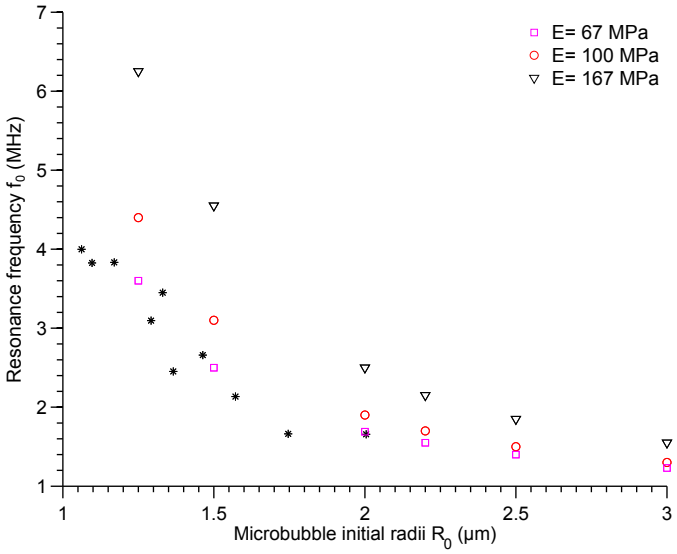

Figure 3.6: Resonance frequencies of SonoVue® microbubbles from experimental data published by Van Der Meer *et al.* (2004) © 2004 IEEE are represented by an asterisk (∗). The resonance frequencies f_0 were estimated using equation 3.37 for R_0 =1.25, 1.5, 2, 2.2, 2.5, and 3 µm radii with η_1=0.7 Pa.s, λ_1=0.06 µs, E=67 to 167 MPa, e=2 nm at p_0 = 130 kPa.

In Figure 3.6, an increase of Young's modulus is accompanied by an increase in the resonance frequency. This affects smaller bubbles more drastically than

larger bubbles. By comparing the simulated results to the experimental data from Van Der Meer *et al.* (2004), it was possible to estimate the elasticity E to be in the range of 50 to 70 MPa.

Qualitative changes of the relaxation time λ_1

The resonance frequency was calculated at different relaxation modulus $\lambda_1 = 0.02, 0.06, 0.1\mu s$ for an elastic modulus of E =67 MPa and a viscosity parameter η =0.7 Pa.s.

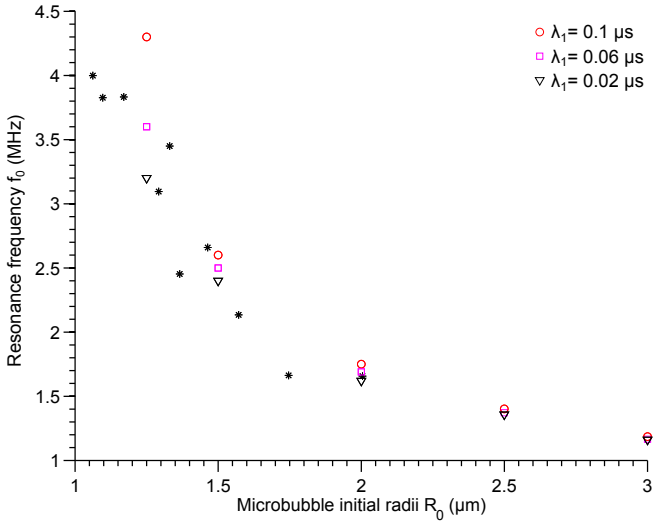

Figure 3.7: Resonance frequencies of SonoVue® microbubbles from experimental data published by Van Der Meer *et al.* (2004) © 2004 IEEE are represented by an asterisk (∗). The resonance frequencies f_0 were estimated using equation 3.37 for R_0 =1.25, 1.5, 2, 2.5, and 3 μm radii with η_1=0.7 Pa.s, λ_1=0.02 to 0.1 μs, E=67 MPa, e=2 nm at p_0 = 130 kPa.

From the results shown in Figure 3.7, the relaxation time parameter has a negligible effect on the resonance frequency for microbubbles of a size greater than 2 μm.

Qualitative changes of the viscosity η_1

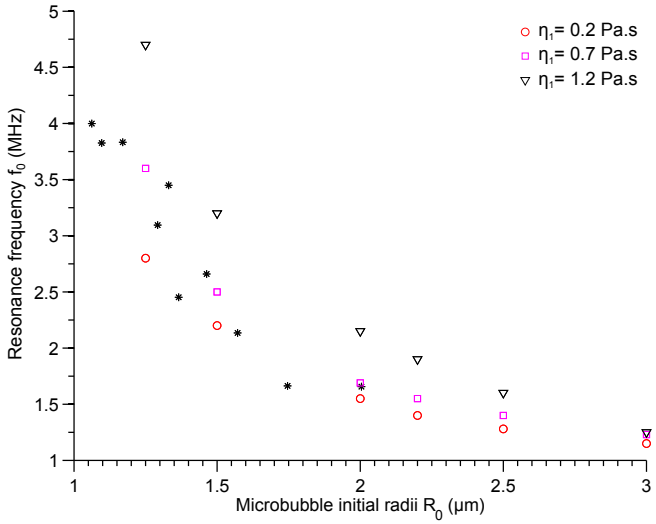

Figure 3.8: Resonance frequencies of SonoVue® microbubbles from experimental data published by Van Der Meer *et al.* (2004) © 2004 IEEE are represented by an asterisk (∗). The resonance frequencies f_0 were estimated using equation 3.37 for R_0 =1.25, 1.5, 2, 2.2, 2.5, and 3 μm radii with η_1=0.2 to 1.2 Pa.s, λ_1=0.06 μs, E=67 MPa, e=2 nm at p_0 = 130 kPa.

In Figure 3.8, the viscosity has a non-negligible impact on the resonance frequency. An increase of the viscosity by 1 Pa.s increases the resonance frequency by $\sim$ 1.2 times at $R_0 = 2.5\mu$m radii while almost doubling ($\sim$ 1.7) at $R_0 = 1.25\mu$m radii.

Resonance frequency calibration of the FE model to SonoVue® microbubbles

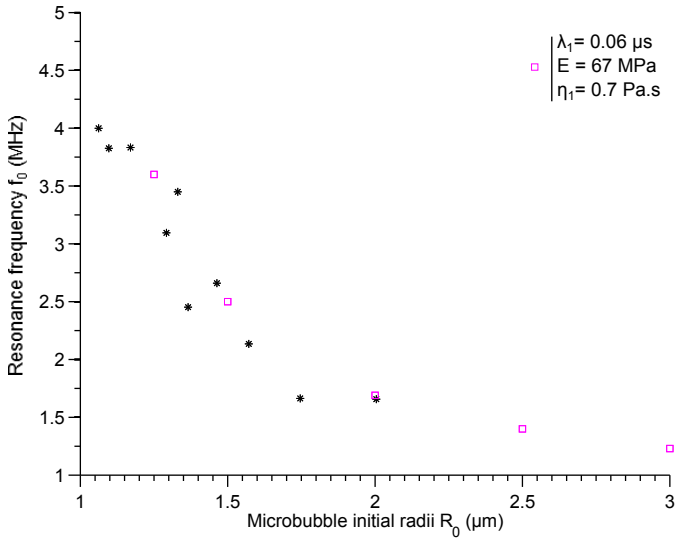

Figure 3.9: Resonance frequencies of SonoVue® microbubbles from experimental data published by Van Der Meer *et al.* (2004) © 2004 IEEE are represented by an asterisk ($*$). The resonance frequencies f_0 were estimated using equation 3.37 for $R_0 = 1.25$, 1.5, 2, 2.5 and 3 μm radii with η_1=0.7 Pa.s, λ_1=0.06 μs, E=67 MPa, e=2 nm at $p_0 = 130$ kPa.

In Figure 3.9, with a viscosity of $\eta_1 = 0.7$ Pa.s, a relaxation time of $\lambda = 0.06\mu$s and an elastic modulus of $E = 67$ MPa some degree of correlation with the experimental data is achieved. For the results shown in this Section, an increase of the elasticity could potentially be counter-balanced by a decrease in the viscosity to attain a similar resonance frequency curve.

3.3.2 Amplitude

To further calibrate the shell parameters, the results from the FE model are compared to published experimental data by analysing the amplitude oscillations. Numerical results are compared to the maximum radial oscillation of the experimental data presented by Vos *et al.* (2009).

Qualitative changes of the viscosity η_1

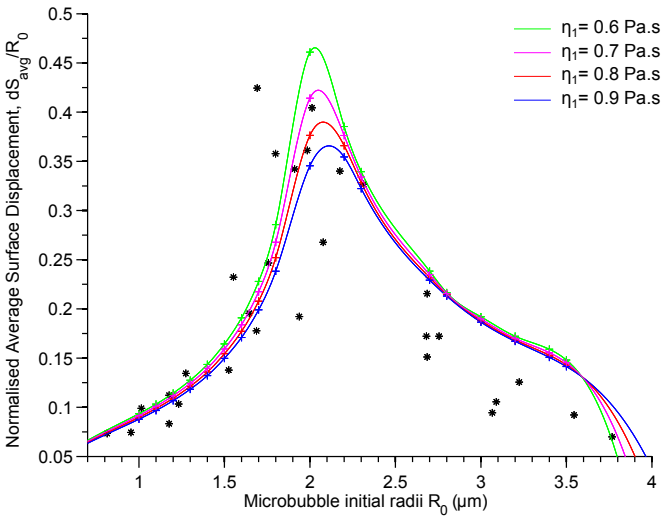

Figure 3.10: The average maximal surface displacement normalised with the initial radii. With η_1=0.6-0.9 Pa.s, λ_1=0.06 μs, E=67 MPa, p_0 = 80 kPa and an insonation frequency of 1.7 MHz. Experimental data points reproduced from Vos *et al.* (2009) © 2009 IEEE are represented by an asterisk (∗).

In Figure 3.10, the average maximal surface displacement d_{max} defined in 3.36 was normalised by the initial radii R_0. An increase of the viscosity decreases the normalised surface average maximum displacement amplitude. The decrease is accompanied by an small increase —0.1 μm— of the initial radii at which the microbubbles become resonant at the excitation frequency of 1.7 MHz. This was previously observed in Figure 3.8 where this change is related to the increase of the resonance frequency.

Qualitative changes of the relaxation time λ_1

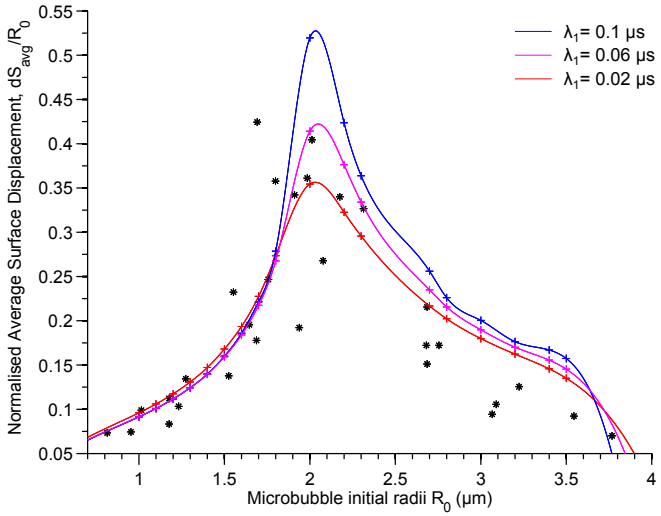

Figure 3.11: The average maximal surface displacement normalised with the initial radii. With η_1=0.7 Pa.s, λ_1=0.02-0.1 μs, E=67 MPa, p_0 = 80 kPa and an insonation frequency of 1.7 MHz. Experimental data points reproduced from Vos *et al.* (2009) © 2009 IEEE are represented by an asterisk (∗).

In Figure3.11, at an excitation frequency of 1.7 MHz, SonoVue® microbubbles with an initial radii of about 2 μm resonate. An increase of the relaxation time, increases the average maximal surface displacement of resonant microbubbles.

3.3.3 Amplitude and resonance frequency calibration of the FE model to SonoVue® microbubbles

In this Section, by varying the viscosity and the relaxation time, the simulated amplitude shown in Figures 3.10 and 3.11 matches the experimental data from Vos *et al.* (2009). This was only possible once the elastic modulus E was calibrated. The modulus is affecting greatly the resonance frequency as presented in the previous Section 3.3.1, where the simulated resonance frequencies were compared against the data presented by Van Der Meer *et al.* (2004). Table 3.1 recapitulates the estimated shell parameters that allowed calibration of the FE model.

Table 3.1: Calibrated simulation parameters

Parameter	Value
Young's modulus, E	67 MPa
Relaxation time, λ_1	0.06 μs
Shear viscosity, η_1	0.7 Pa.s
Poisson's ratio, ν	0.499 (Patil *et al.*, 2010)
Density of lipids, ρ_l	1100 kg/m^3 (van der Meer *et al.*, 2007)
Shell thickness, e	2 nm
Speed of sound in water at 298.15 K, c_m	1480 m/s
Density of water at 298.15 K, ρ_m	997 kg/m^3
Polytropic gas index, γ	1.07

3.4 Discussion and concluding remarks

The following remarks can be made from the results presented in this Chapter:

- An increase of the viscosity η_1 is characterised by a decrease in the oscillation amplitude at resonance and a shift of the resonance frequency f_0 to higher frequencies.
- An increase in the relaxation time λ_1 is accompanied by an increase of the oscillation amplitudes at resonance.
- The effect of the relaxation time λ_1 on the resonance frequency of large microbubbles ($R_0 > 2\mu$m) may be neglected.

The elastic theory of thin spherical shells have a small extent in the thickness of the shell which enables to consider simplifying the interpretation of the calibrated parameters. The value of the Young's modulus given in the table 3.1 is relevant only to a three-dimensional interpretation of the stress-strain relation in the shell. However, the study of microbubble dynamics with Rayleigh-Plesset (R-P) like equations or other method for the surface rheology do not always take in account the thickness of a monolayer interface.

A first approach for a comparison with the literature could be with the Kirchoff-Love plate or the Mindlin-Reissner plate theories which provide the simplification of the surface strain–stress relation without neglecting the shell thickness. Then, the surface strains can be characterised by a two-dimensional Young modulus (Paulose & Nelson, 2013). The two-dimensional elastic modulus Y characterising the shell is defined as:

$$Y = E \times e, \tag{3.38}$$

which may also characterise the bending rigidity of a shell. The thicker the shell, the less bendable it becomes.

The value of Y equals to 134 mN/m with the calibrated Young's modulus E for SonoVue® microbubble from table 3.1. Using atomic force microscopy McKendry *et al.* (2010) had found a value of 25 mN/m for a 3µm radii microbubble similar in composition to the microbubbles in Section 4.2.1 produced by a flow

focusing method using a microfluidic device. However, the estimated values increase for decreasing microbubble radii. This suggests that the estimated elastic modulus is not independent of the surface curvature. Separately, Saulnier *et al.* (2001) studied the elastic properties of Langmuir trough for different amphiphilic molecules at a gas and water interface using a pendent drop mechanism. The following estimated parameters were found: DPPC: 6 ± 2 mN/m, PEG2000: 1 ± 1 mN/m, hen egg white lysozyme 89 ± 5 mN/m. From the discussed values one may find that the estimation of the two-dimensional elastic parameter Y is not independent on the method used and that various amphiphile molecules have a two-dimensional elastic modulus that may take values within broad range. For this reason, only estimated parameters of SonoVue® will be now compared.

A second approach would be to compare the shear modulus and viscosity of the FE model to the variables of Rayleigh-Plesset-like equations. However these equations do not always incorporate a shell thickness and a comparison may be done by employing equivalent material properties: the elastic dilational modulus χ_{eq} and the viscous dilational modulus κ_{eq} which were respectively defined by Marmottant *et al.* (2005) and Doinikov & Dayton (2007) by comparing the models presented in Chatterjee & Sarkar (2003) and Church (1995) to their respective zero-thickness shell model:

$$\kappa_{eq} \approx 3e\eta_1, \tag{3.39}$$

$$\chi_{eq} = e\frac{E_{t0}}{2(1-\nu)} = e\frac{G_{t0}(1+\nu)}{(1-\nu)} \approx 3eG_{t0}, \tag{3.40}$$

where E_{t0} is the total initial elastic modulus which is related to the total initial shear modulus G_{t0} by the formula $E_{t0} = 2G_{t0}(1+\nu)$ as a consequence of Hooke's law for a homogeneous material.

These new parameters are necessary to permit the comparison of the values with the ones found in the literature, since in this work a viscoelastic model with a dissipating shear modulus is used to model the rheological effect. This modulus

is the non-equilibrium shear modulus G_1 previously defined in Sections 3.2.2. The following reformulation of equation 3.40 is preferred:

$$\chi_{eq} = e\frac{(G + G_1)\,(1 + \nu)}{(1 - \nu)} = e\frac{E/2 + G_1(1 + \nu)}{(1 - \nu)} \approx e(E + 3\frac{\eta_1}{\lambda_1}), \tag{3.41}$$

The formula 3.41 resembles to equation 3.38 with the additional terms related to the non-equilibrium shear modulus.

The calibrated parameters from table 3.1 allow to calculate the values $\chi_{eq} = 0.20$ N/m and $\kappa_{eq} = 4.9 \times 10^{-9}$ kg/s. Tu *et al.* (2009) estimated using Rayleigh-Plesset-like equations the elastic and viscous coating parameters of SonoVue®. Using a method of light scattering the experimental data was compared to simulated amplitude oscillations to find the following calibrated parameters: $\chi_{eq} = 0.22$ N/m and $\kappa_{eq} = 2.5 \times 10^{-9}$ kg/s. Additionally Van Der Meer *et al.* (2004) estimated a value of $\chi_{eq} = 0.26$ N/m by using solely the measured resonance frequency of SonoVue microbubbles. This permits to conclude that the estimated shell parameters using the FE model are within a comparable order of magnitude of those that were published for the same type of microbubble and that the assumptions taken for the FE model to simulate the microbubbles at low acoustic pressures are valid.

Chapter 4

Microbubble surface modes

4.1 Introduction

Stress propagates in mediums as an elastic deformation that can be observed along the surface of a medium similarly to a wave on the surface of water after being disturbed. When the medium becomes sufficiently thin, the propagation of the stress is observable not only on the top surface but also on the bottom one. Lamb (1917) investigated the propagation of elastic waves in thin plates and observed extensional waves and flexural waves whose modes are dependent on the thickness of the plate. To solve the problem of Lamb waves, one must find the solution to the linear acoustic wave equation subjected to the boundary conditions that define the surfaces. In acoustics, guided waves is the modern term for the analysis of Lamb waves.

Surface modes occur as a result of the existence of Lamb waves in the microbubble shell Baker (1961). These modes can be categorised by the number of wavelengths n of the distortions that span the bubble's circumference. Different modes can exist concurrently and include the breathing mode (n=0), which accounts for the bubble periodic spherical contractions and expansions also known as a monopole oscillation. In the dipole mode (n=1), accounts only for bubble translational oscillations. P. Marmottant describes the translational oscillations normal to a nearby wall as the primary mechanism with the radial oscillations to cause local microstreaming Marmottant *et al.* (2006). In the quadrupole mode

(n=2), the shape alternates between a prolate and oblate spheroid. At higher mode order, bubbles resemble shapes that can be approximated to a tetrahedral shape (n=3), a cube (n=4), a pentagonal bipyramid (n=5), an icosahedron (n=6), etc. Dollet *et al.* (2008) suggested the notable feature of these non-spherical shape oscillations is that they might be accompanied by sub-harmonic behaviour which enables to enhance the contrast between the blood and tissues in ultrasound imaging. However, as noted by Leighton (1997), using a linearised theory of bubble dynamics of Lamb (1993) it can be shown the acoustic pressure from the shape oscillations rapidly decay at a rate of $d^{-(n+1)}$ for an increasing distance d away from the bubble surface. Similarly Neppiras (1980) discussed three different possible explanations for the generation of sub-harmonics signals for bubbles under stable cavitation, of which the ones generated by the surface modes ($n \geq 2$) are only weakly coupled to the liquid since they are not involved in a change of area. The weakly coupled pressure field was observed for 5.7 µm microbubble and is depicted in Figure 4.1. Within 3 micrometers of the microbubble vicinity, the positive pressure that accompanied the shape mode is dispersed.

Observation of surface modes occurrences using FE modelling of polystyrene micro-spheres and BR-14 (Bracco Imaging Italia srl, Milan , Italy) microbubble type was carried out by Falou (2011). The two-dimensional axi-symmetrical model faired well to model surface modes of polystyrene micro-spheres, but the model exhibited modes not higher than $n = 1$ —the breathing mode ($n = 0$) and the forward-backwards 'rocking motion' ($n = 1$)— for the modelled microbubble type. Although an amount of displacement was observed to occur in the shell, these were multiplied by a factor of 3.5×10^5 to 1.5×10^7 for visualisation purposes. O. Falou presented the results previously in (Falou *et al.*, 2010), however the shell displacements were not discussed. A direct cause of the weak amplitude displacements cannot be given with certainty with the details on the mesh elements provided in their published work. One of the two possible explanations is that although their model used the shell material parameters of a BR-14 from the literature, the resonance frequencies of a range of microbubble diameters were calibrated with a shell thickness of 3 nm and the subsequent studies of the modes

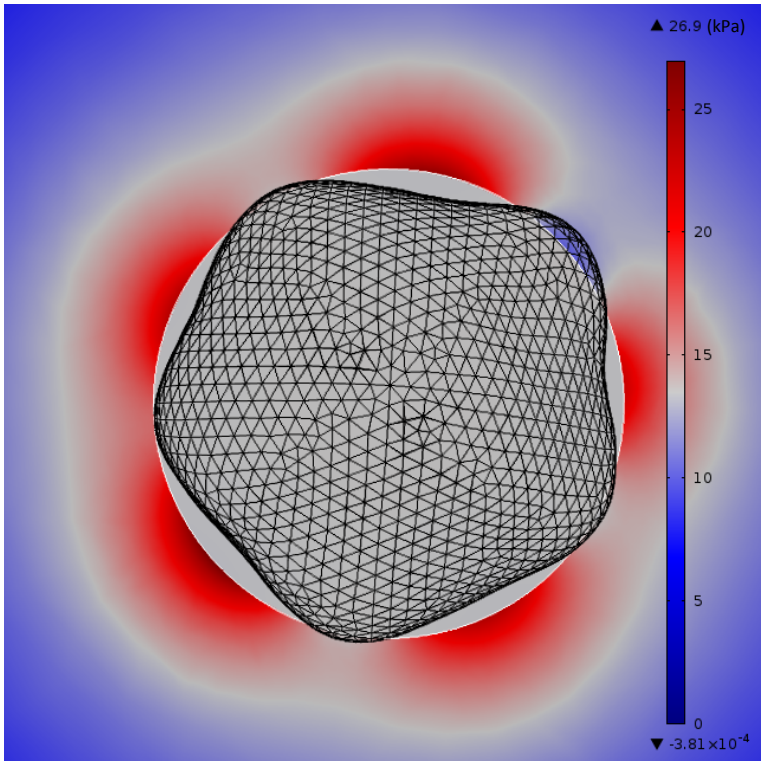

Figure 4.1: A 5.7 μm microbubble subjected to a 20 kPa plane wave acoustic field at 0.65 MHz. E=130 MPa, λ_1=0.01 μs, η_1=0.6 Pa.s

were estimated with a model with a 100 nm shell thickness with different resonance characteristics. Since the stiffness of the shell which can be represented by the dilation elasticity modulus $\chi_{eq\approx}3eG \approx eE$ is proportional to the shell thickness, at $e = 100$ nm the stiffness may have become too high to enable shell mode deformations for the given pressure field due to a high bending stiffness. The relation between the shell thickness and the bending stiffness was discussed in Section 3.4. The other possible explanation is the element locking phenomenon that was introduced in Section 2.2.1. The studied shell with a thickness ranging from 3 to 100 nm might have been too thin for the mesh generator to accommodate a sufficient amount of elements across the shell thickness. The study fails to mention if enough care was taken to allow the shell to bend which would have allowed the occurrence of surface modes of the order higher than 1.

The onset of mode resonance was previously studied for microbubbles by B.Dollet in Dollet *et al.* (2008), where modes were found dependent on the insonation pressure and bubble radii at a given excitation frequency of 1.7 MHz. Nonspherical deformations were found to develop preferentially at bubble resonance, but also found often accompanied by surface modes for insonation pressures above 100 kPa at 1.7 MHz for BR-14 microbubbles (Bracco Imaging Italia srl, Milan , Italy).

The study of non-spherical vibration of Definity (Bristol Myers Squibb MI, N. Billerica, MA, USA) contract agent in contact of a wall were studied by Vos *et al.* (2008) Jetting phenomena were observed at pressures of 140 kPa. This motivated to study surface modes at pressures below this phenomenon would occur.

The mechanical index (MI) permits to evaluate the potential mechanical effect of an acoustic wave on biological tissues. The MI is defined as (De Jong, 2002):

$$\mathrm{MI} = \frac{P_-}{\sqrt{f}}, \tag{4.1}$$

where P_- is the peak negative pressure in MPa and f is the frequency in MHz. This value should remain below 1.9 to limit the risks of tissue damage in medical

applications.

Optical observations of the sonoporation mechanics of human histiocytic lymphoma cells (U937) by Moosavi Nejad *et al.* (2011) showed that at a low acoustic pressure of 70 kPa at 0.834 MHz a significant amount of cell material was displaced. A microbubble was placed in the vicinity of a cell and the low acoustic pressure (MI=0.077) was sufficient to displace the cell membrane towards the radially linearly oscillating microbubble by 2.85 μm in 8 ms. The positive fluorescent staining confirmed that the local protrusion was accompanied by an increase of permeability of the cell membrane without cell lysis. Additionally micro-beads confirmed local increase in micro-streaming in the presence of microbubbles in comparison to ultrasound alone. The study suggested the shear-stress generated by the liquid micro-streaming is the main cause to the deformation of the cell membrane during sonoporation. Although the study used a cell type whose membrane is relatively soft compared to cells from vascular wall, malignant cells of tumour tissue also have a soft membrane.

Microbubbles with an additional layer of oil beneath the lipid shell are capable of carrying a lipophilic therapeutic payload. Such agents were employed by Shortencarier *et al.* (2004) to study the effect of radiation forces as a method to enhance the adherence of fluorescently labelled oil to a monolayer of human melanoma cell (A2085). Although the study distinguished the method used (radiation force) from sonoporation, the study did not put in place a methodology to avoid sonoporation. The use of radiation force to bring the agents in contact to the cells was also likely to exert some degree of sonoporation since sonoporation is concomitant of microbubbles oscillating in the vicinity of cells. In the study, the radiation force was exerted by a 10 million cycles sine tone burst at 3 MHz and 50 kPa. The signal enabled a tenfold increase fluorescence intensity compared to a signal of three 5 cycles at 1.5 MHz and 2 MPa (MI=1.6) separated by 20 μs intended for microbubble destruction. The combination of both signal increased the fluorescence transfer by a further 50% successfully proves radiation force helps deposition of the labelled oil, however the study does not explain the presence of fluorescent cells when using the signal intended for radiation force. Although the

presence of sonoporation is debatable, if leakage of oil from the agents is involved at such relatively low acoustic pressures (MI=0.03), the mechanical stresses on the agents and the local medium must be of a non-negligible intensity.

4.2 Experiment

4.2.1 Preliminary experiment and results

In-house lipid coated microbubbles were produced to have similar acoustic properties to Definity microbubbles (Lantheus Medical Imaging Inc., N. Billerica, MA) (Faez *et al.*, 2011; McLaughlan *et al.*, 2013). The lipids (*e.g.* DPPC (1,2-Dipalmitoyl-sn-3-phosphocholine), DPPE (1,2-Bis(diphenylphosphino)ethane) and DPPA (Diphenylphosphoryl azide)) come within a solution of chloroform at a concentration of 20 mg/L and are kept in a $-20°C$ environment. Several types of lipids can be mixed together in a vial using a micro-pipette or a micro-litre graduated syringe. A mixture of $19\mu L$ of DPPC (1,2-Dipalmitoyl-sn-3-phosphocholine) and $6.5\mu L$ of DSPE-PeG2000 Biotin (1,2-distearoyl-sn-glyco-3-phosphoethanolamine-N-[biotinyl(polyethylene glycol)-2000] (ammonium salt)) was employed. The mixture was dried by evaporation of the organic solvent (chloroform) using a vacuum chamber for at least an hour for $50\mu L$ of lipids per vial. The lipids can also be dried using pure nitrogen gas, by blowing continuously the gas for at least 30 minutes in the vial for the same amount of lipids per vial. After evaporation of the chloroform, a thin film deposit is observable at the bottom. In this form the lipids can be kept frozen for a several weeks for storage. Then the lipids were suspended in an aqueous solution via vortex (BV1000 Bench-Mixer, Benchmark Research Products) for 30 seconds followed by bath sonication (Ultrawave U50, Ultrawave Ltd., Carfiff, UK) for minimum of one hour. At the suspension stage, before vortex and sonication, eventually other components (*e.g.* macrogol 4000, polyethylene glycol (PEG), palmitic acid, glycerine) can be added to the solution to modify the microbubble characteristics. 1 mL of saline solution for each vial is employed in the suspension stage necessary. The composition of the saline solution is described in the table 4.1 and was prepared by mixing all the components until the Na-Cl crystals were completely dissolved.

The microbubbles were produced by employing a shaking method, whereby, firstly the air headspace of each 2ml vials was purged with 10 mL of octafluoropropane (C_3F_8) gas prior to the refrigerated storage to bring the pre-microbubble

Table 4.1: Composition of the saline solution

Component	Amount
De-ionised water	$250mL$
Na-Cl crystals	$10g$
Glycerine	$2.5mL$

lipid suspension to room temperature. Secondly, using a mechanical shaker (CapMix^{TM}, 3M ESPE AG., Seefeld, Germany) the viols are shaken for a duration of 60 seconds to form the microbubbles to create an emulsion from the pre-microbubble lipid suspension. Eventually, an excess of lipids and other aqueous components can be achieved via flotation, a process whereby mild centrifugation is used. The microbubbles can last a few hours within the viol and have a poly-dispersed size distribution of 2 to 10 μm. Additionally, they can be reactivated by replacing the air headspace with new gas and shaking the viols for 60 seconds.

The in-house produced microbubbles were diluted with de-ionised Milli-Q water (Millipore Corporation, Billerica, Massachusetts, USA) and injected into a μ-Slide I$^{0.4}$ Luer Ibidi® (Ibidi GmbH, München, Germany) chip with a single 400μm deep, 5mm wide and 50mm long channel. Observations were made under an inverted Nikon Eclipse Ti microscope (Nikon corporation, Tokyo, Japan) with a 200 × optical magnification coupled onto the ocular system with a Shimadzu HPV-1 (Shimadzu Europa GmbH) monochrome high-speed camera. 100 frames were recorded at 1 Mfps (million frames per second) after being triggered 55 μs after the signal was generated by a waveform generator Agilent 33250A Arbitrary Waveformer (Agilent Technologies Inc., Loveland, Colorado, USA). A 0.5 MHz, 30 cycles sinusoidal signal was amplified with an E&I A150 power amplifier (Electronics & Innovation Ltd., Rochester, NY, USA) to provide a 55dB voltage gain and drive an A310S transducer (Olympus NDT Inc., MA, USA) to

generate 100 kPa in peak negative pressure.

Although in this preliminary experiment only two microbubbles were observed undergoing surface modes, it was found that the larger microbubble of 10 µm depicted in Figure 4.3 exhibited a 4^{th} order mode, and the smaller microbubble of 6 µm depicted in Figure 4.2 exhibited a 3^{rd} order mode at the same insonation frequency. Since only the microbubble radii varied between the two observations, their size was observed to have a direct relation to their mode order. The observations confirmed the dependence on the resonance frequency made by Dollet *et al.* (2008) for coated microbubbles and by Versluis *et al.* (2010) for uncoated air bubbles. The preliminary results also provided an approximate acoustic pressure in the range of the 100 $^{\text{th}}$ of kPa to allow the occurrence of the surface modes of sufficient amplitude to be compared with FE modelling results. This was necessary as noted by Dollet *et al.* (2008) the amount of surface deformation was observed to be approximately 4 times lower in the presence of a rigid boundary.

To allow comparison of the experimental results with the calibrated parameters from the table 3.1 of the previous chapter 3.3.3, the experiment would have to employ SonoVue® microbubbles instead of the in-house manufactured ones. Additionally, although the images acquired were of reasonable quality for analysis, they required post-processing to enhance their brightness and contrast and their resolution was insufficient to allow the study of smaller microbubbles. The blurriness observed in the captured frames is sought to be attributed to the duration of the exposition since the microbubbles when in focus prior and post ultrasound exposition. Another factor limiting the experimental setup to the study of large microbubble radii is the maximum frame rate of 1 Mfps. Since the FE analysis estimated the appearance of the modes to be close to the resonance frequency. The smaller the bubble, the higher the excitation frequency is necessary to evaluate the appearance of modes. 1 Mfps corresponds to a frequency of 1 MHz and thus limiting the excitation frequencies to a maximum of 0.5 MHz if a minimum of 2 frames per oscillation cycle is chosen to avoid temporal aliasing. From Figure 3.7 it can be determined an approximate minimum radii of 5 µm to provide a resonance frequency of 0.5 MHz and was a determining factor limiting the study

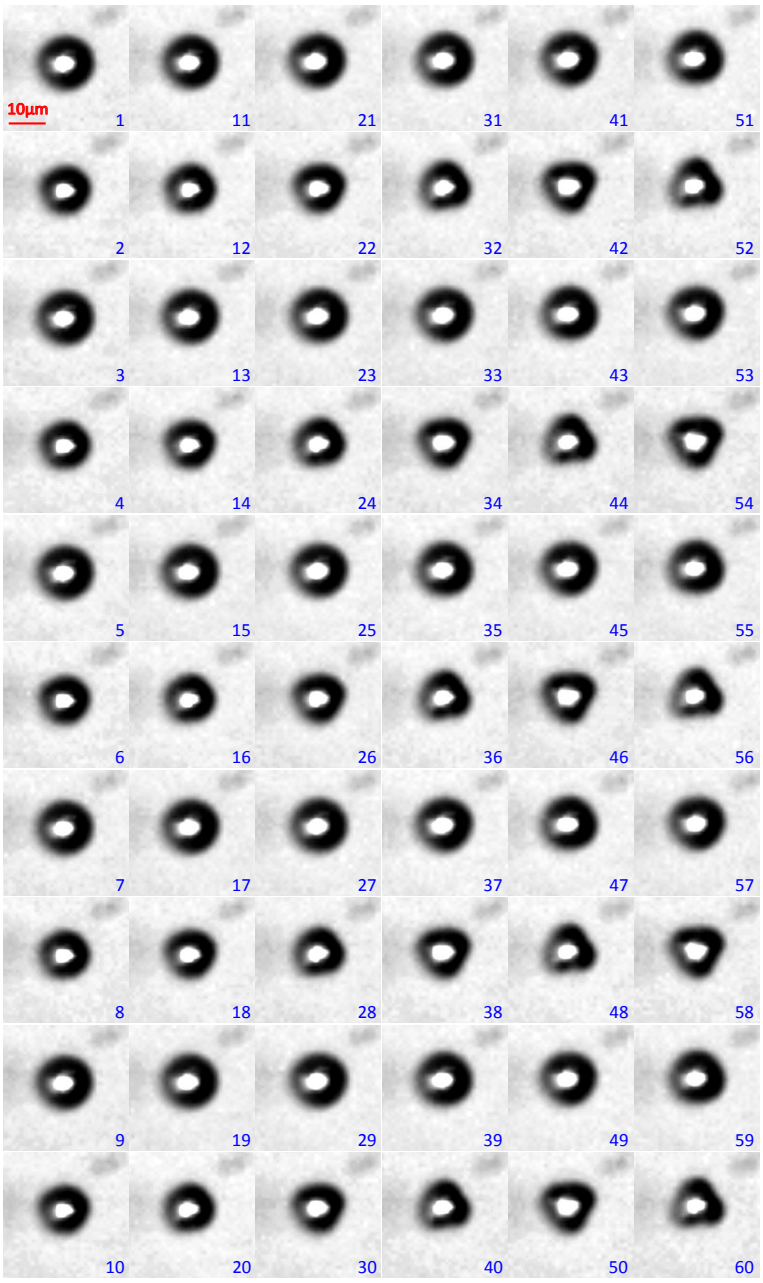

Figure 4.2: A 6 µm microbubble subjected to an acoustic field of 0.5 MHz,100 kPa peak negative pressure.

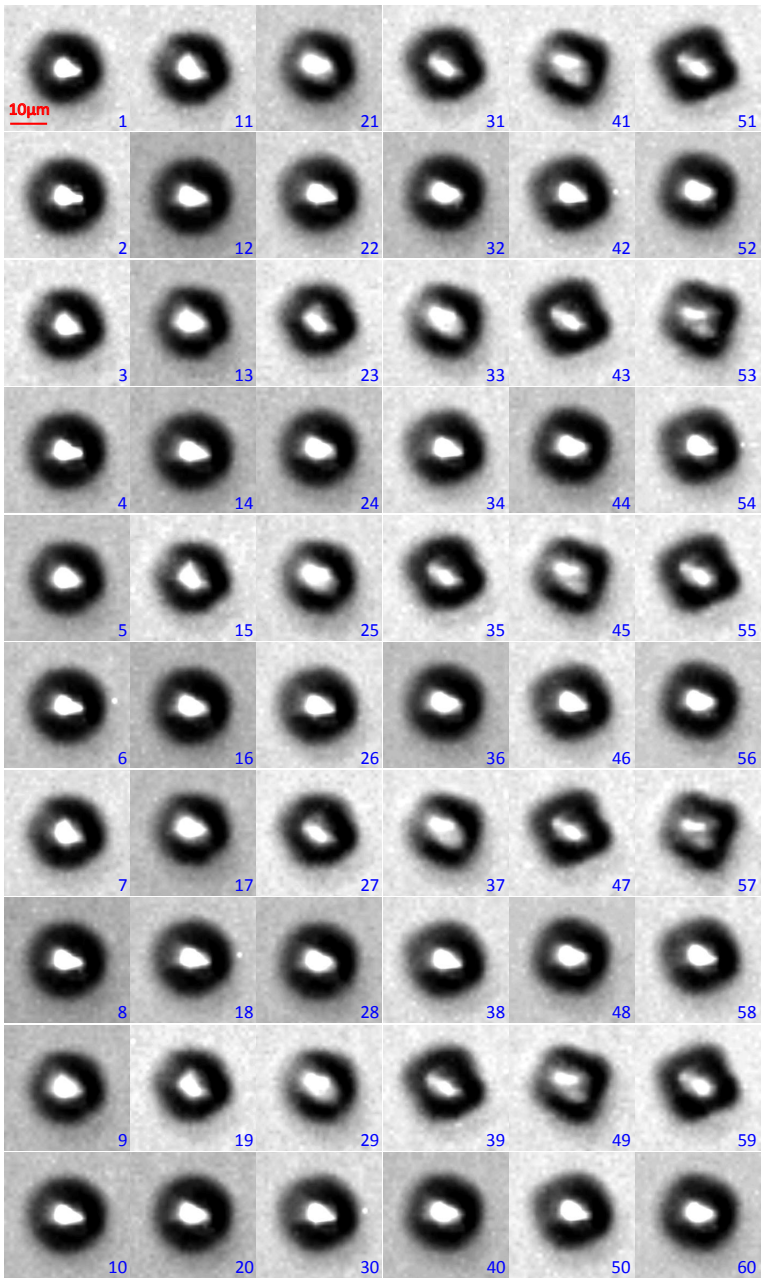

Figure 4.3: A 10 µm microbubble subjected to an acoustic field of 0.5 MHz,100 kPa peak negative pressure.

to large microbubbles.

The observations made in this preliminary experiment also raised an issue if these results where to be compared to FE results. The model's mesh would become inadequate for large bubble radii above 5 µm. An adequate mesh could not be rendered for these large sizes due to the amount of elements necessary to model the thin spherical shell becoming too large to allow the FE problem to converge to a solution with the computation power provided by the hardware. Due to the limitations of the processing power and the ones due to the experimental setup adjustments were necessary. The following Sections introduce the necessary hardware modifications to allow smaller microbubbles to be observed with a wider range of excitation frequencies at an increased resolution and light sensitivity.

4.2.2 Materials and methods

A commercial preparation of 25 mg lyophilised SonoVue® microbubbles were re-suspended by adding 5 mL of sodium chloride (9 mg/mL) solution in the septum-sealed vial containing sulfur hexafluoride (SF_6) gas. The microbubble contrast agents were activated by vigorously manually shaking a SonoVue® viol for 30 seconds to form a homogeneous milky white suspension of lipid coated SF_6 microbubbles.

µ-Slide $I^{0.4}$ Luer Ibidi®(ibidi, Thistle Scientific, Glasgow, UK) chip with a single 400µm deep, 5mm wide and 50mm long channel were employed. A bottom thickness of 180µm allows high resolution microscopy for inverted microscopes. The microbubbles were diluted with de-ionized milli-Q water (Millipore Corporation, Billerica, Massachusetts, USA) to a concentration of approximately $9 \times 10^5 \pm 3 \times 10^5$ microbubbles per millilitre.

Using a circular 13 mm in diameter unfocused Olympus V303 (Olympus NDT Inc., MA, USA) immersible transducer with a peak transmitting frequency of 1 MHz, ultrasound pressure waves were applied at 45 degree angle towards the Ibidi® chip (Ibidi GmbH, München, Germany). A 20 µs ultrasound signal is generated by an Agilent 33250A Arbitrary Waveformer (Agilent Technologies Inc., Loveland, Colorado, USA) and amplified by an E&I A300 (Electronics & Innovation Ltd., Rochester, NY, USA) broadband power amplifier which provides a 55dB voltage gain+-1.5dB before being applied to drive the transducer. The focal length of a transducer is the distance from the transducer to the point in the sound field with the maximum amplitude. For an unfocused transducer this occurs at a distance close to the end of the transducer's near field. The Near field length is the region of the ultrasound field affected by constructive and destructive wave interferences. It is generally accepted the near field ends at the furtherest maxima, which is the focal length.

A theoretical approximation of the near field length for a transducer is given in equation 4.2.

$$d_{NearField} = \frac{D^2 f}{4c}, \tag{4.2}$$

where D is the diameter of the piezo-electric element of the transducer, f is the frequency of the driving signal and c is the sound velocity in the medium.

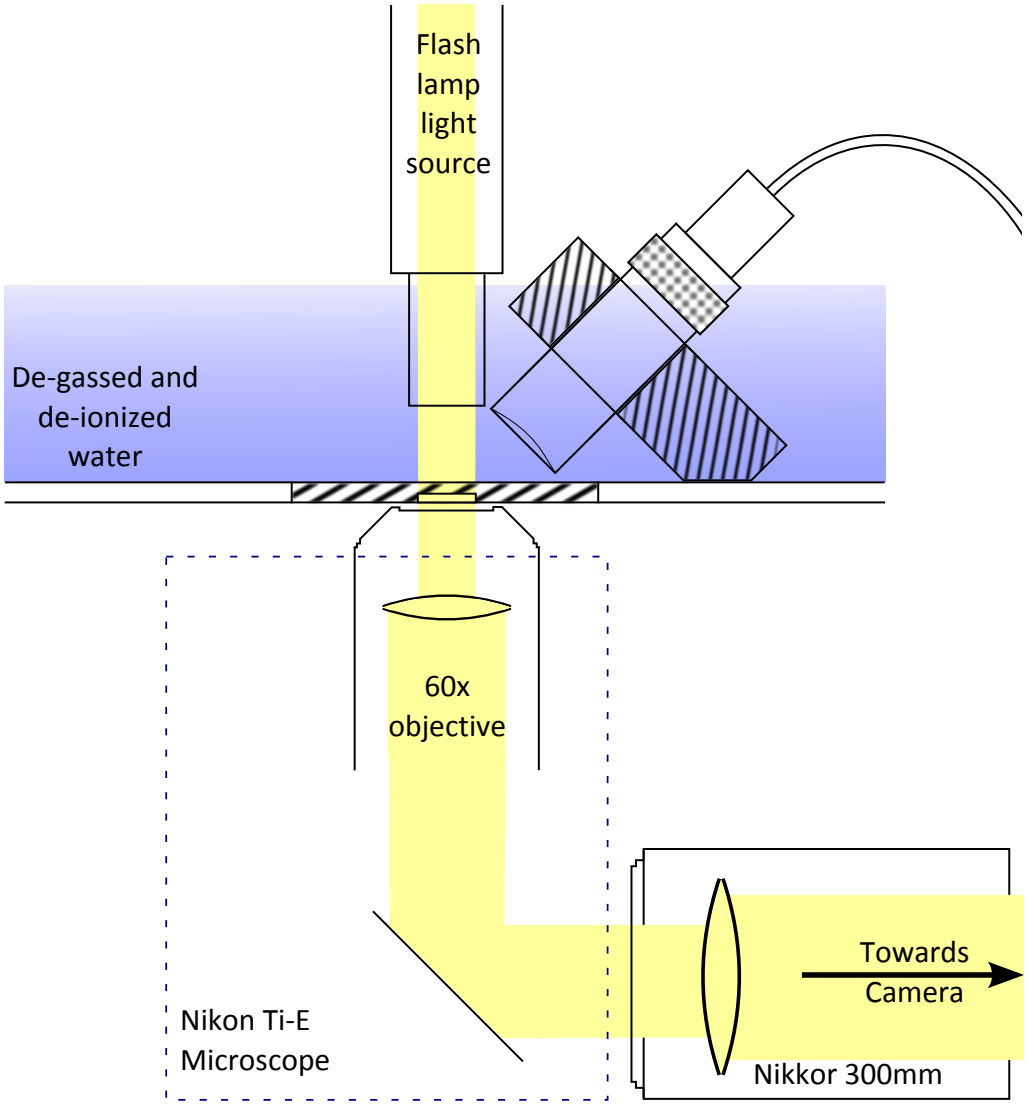

Figure 4.4: The Ibidi μ-slide I Luer is positioned beneath the guided light source. A 1-MHz ultrasound transducer is placed at 45° angle from the bottom.

The analytical solution of equation 4.2 using the previously given parameters gives a near field distance of 28 mm at 1 MHz. Using a 0.20mm needle hydrophone (Precision Acoustic Ltd., Dorchester, United Kingdom), a focal length of 20.5 mm from the transducer was estimated. Care was taken to position the chip at a distance close to the focal length. The amplitude calibration was performed to provide an uniform pressures across the 0.6-1.4 MHz range at the focal length. Please refer to the tables in the appendix A for the calibrated voltage values in millivolts that were estimated to provide a pressure of 80 kPa across the frequency range.

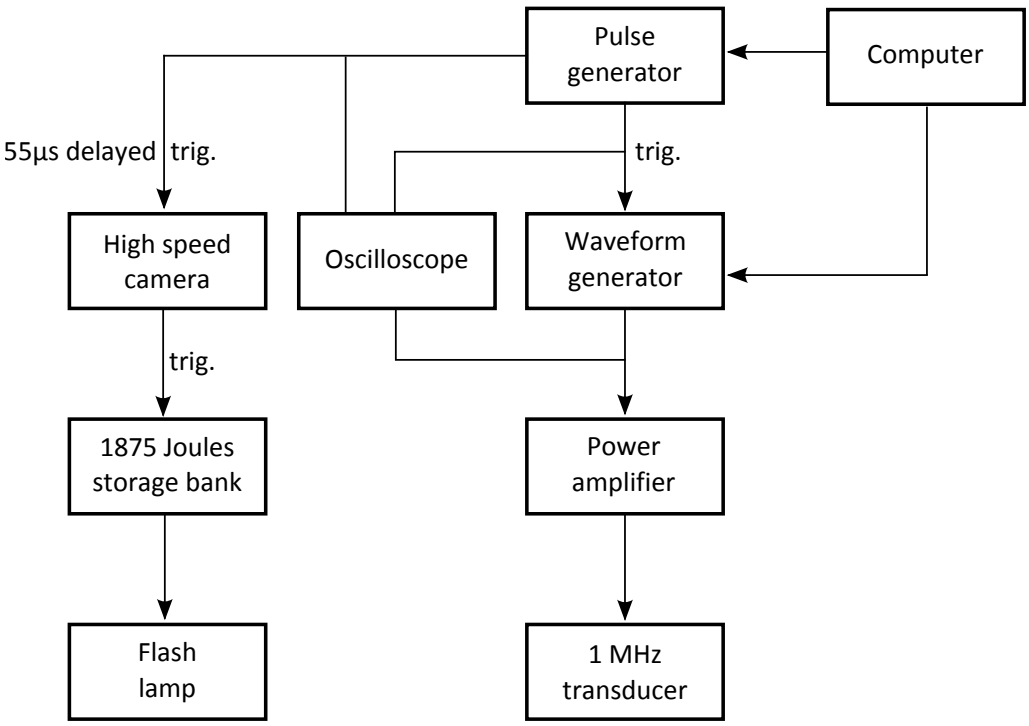

Figure 4.5: Schematic view of experimental setup for the triggering and the signal generation.

To investigate the shape modes, a high speed camera, the Cordin 550-62 (Cordin Company, Salt Lake City, Utah, USA), is combined with the acoustic setup described previously. The camera has a circular array of 62 charge-coupled

devices (CCD) illuminated in series by a light beam reflected by a rotating mirror. Compressed Nitrogen gas was used to rotate the mirror with a gas turbine and operate the camera at 0.8 million frames per second (Mfps). Compressed Helium gas was used to operate the camera at the high frame rates of 2.0 Mfps and 2.5 Mfps. In each series of 1000 by 1000 pixels images, 64 frames were recorded, of which 2 are void frames.

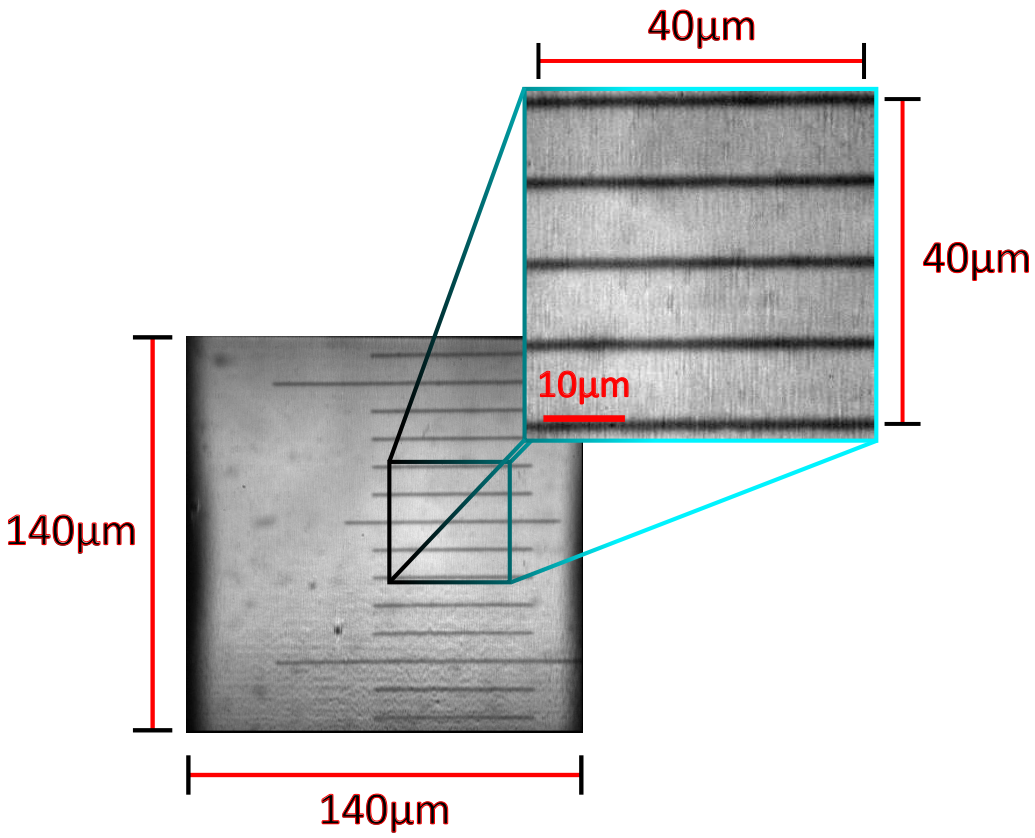

Figure 4.6: A 140µm^2 area of the Ibidi µ-slide I Luer chip is captured by the high frame rate Cordin 550 camera. Images captured by the CCDs have 1000 × 1000 pixels. A 40 µm^2 crop area from each series of frames is analysed.

A schematic view of the optics is shown in Figure 4.4. It consists of the high speed camera which is coupled to an inverted Nikon Eclipse Ti microscope (Nikon corporation, Tokyo, Japan) with a 300 mm focal length Nikkor lens (Nikon

Corporation, Tokyo, Japan). A light beam is guided with a fibre optic from a Cordin flash lamp model 607 towards the top of the Ibidi® chip and observed from beneath with a 60× microscope objective. A storage bank of 1875 Joules is discharged in the flash lamp at 5 kV direct current in 200 milliseconds.

A 9520 digital delay pulse generator (Quantum Composers Inc., Bozeman, Montana, USA) operated via a computer running Matlab (The MathWorks, Inc., Cambridge, United Kingdom) triggers the arbitrary waveform generator and the high-speed camera which is delayed by 55 µs in order to provide time for the ultrasound to travel through the medium. A schematic view of the combined setup is shown in Figure 4.5.

The camera was calibrated with a transparent graduated ruler with indentations measuring 10µm wide. For analysis a 40 by 40 µm crop area, with the microbubbles centred in the middle, is examined in each series of frames 4.6.

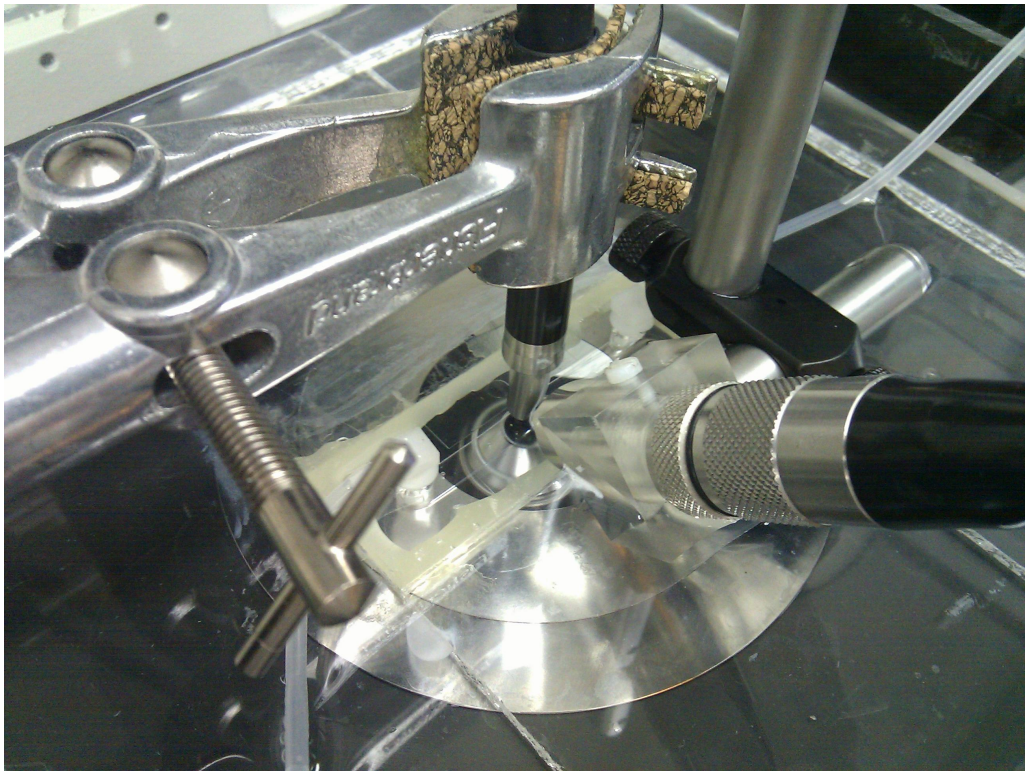

Figure 4.7: The Ibidi μ-slide I Luer is positioned beneath the guided light source. A 1-MHz ultrasound transducer is placed at 45° angle from the bottom.

4.2.3 Results

The high speed camera acquires 64 frames, however since it has 62 CCD sensors cameras due to space limitations, 2 frames per series of 64 frames are void frames. Additionally, some CCDs do not always capture a frame probably due to faulty voltage gain or faulty memory. These issues are out of the users control and therefore could not be alleviated.

Due to the limits on the frequency range of the transducer, not all mode orders can be covered for each studied bubble sizes. Optical tweezers, such as those employed by Prentice *et al.* (2005) can trap single microbubbles with a minimal amount of force to prevent them rising due to their buoyancy. In this experiment this effect was not counteracted and microbubbles were rising to the bottom boundary of the top glass of the chip. This is believed to have limited the maximum possible amount of acoustic pressure without the microbubbles being driven in a jetting phenomenon. In some cases this is believed to have brought the microbubble sightly out of focus after a single tone burst insonation. However the most problematic feature was the acoustic pressure reradiated by the vibrating top glass boundary during insonation, which was thought to bring the the microbubbles towards or away from the boundary in some cases.

Surface modes estimation of a $\sim 4\mu$m radii microbubble

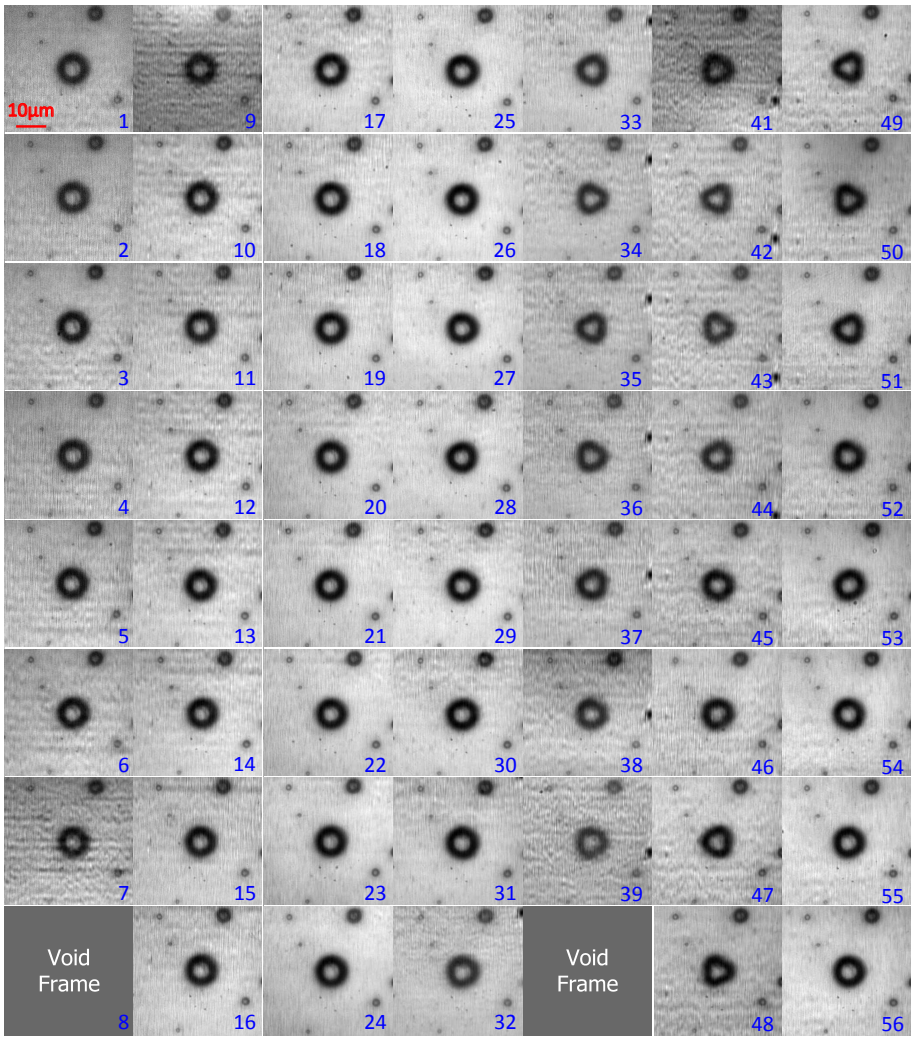

Figure 4.8: 56 first captured images from a series of 64 images. Mode 3 at 0.7 MHz and 25 kPa (40 mV) of a $\sim 4\mu$m SonoVue® microbubble at 0.8Mfps.

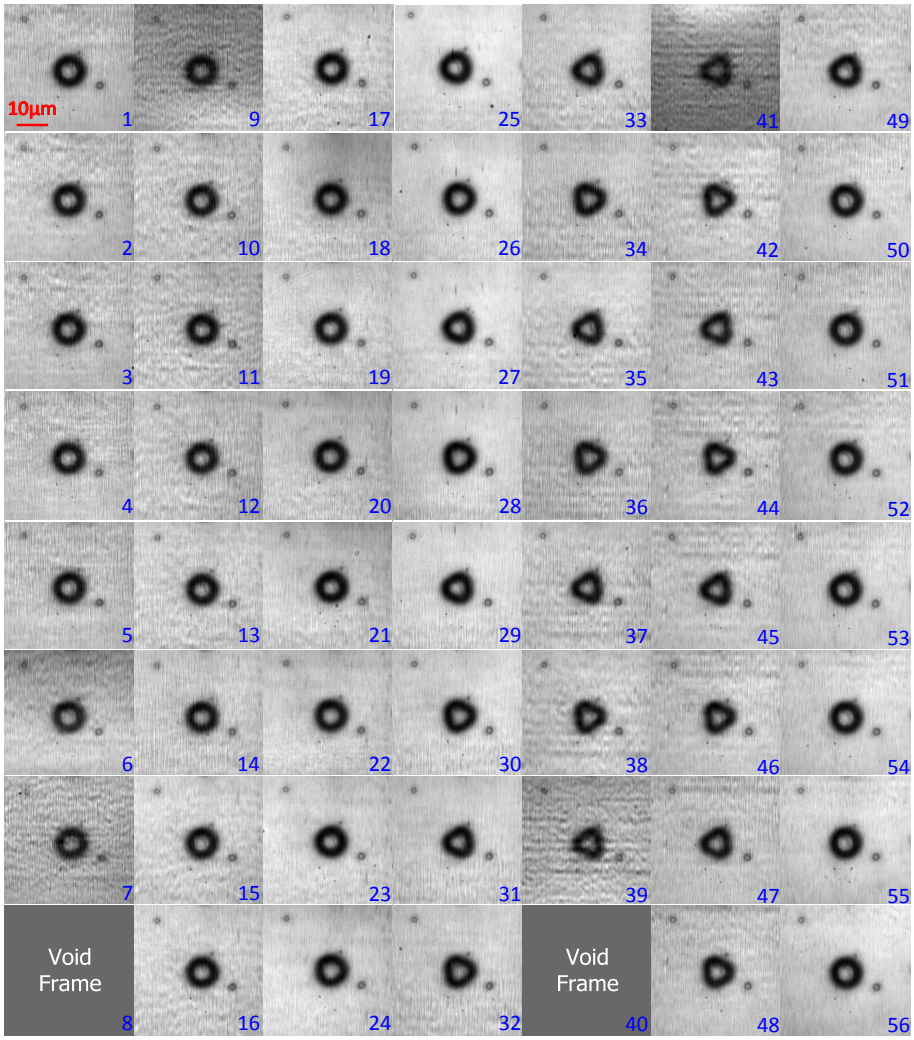

Figure 4.9: 56 first captured images from a series of 64 images. Mode 3 at 0.8 MHz and 25 kPa (30 mV) of a $\sim$ 4µm SonoVue® microbubble at 0.8 Mfps.

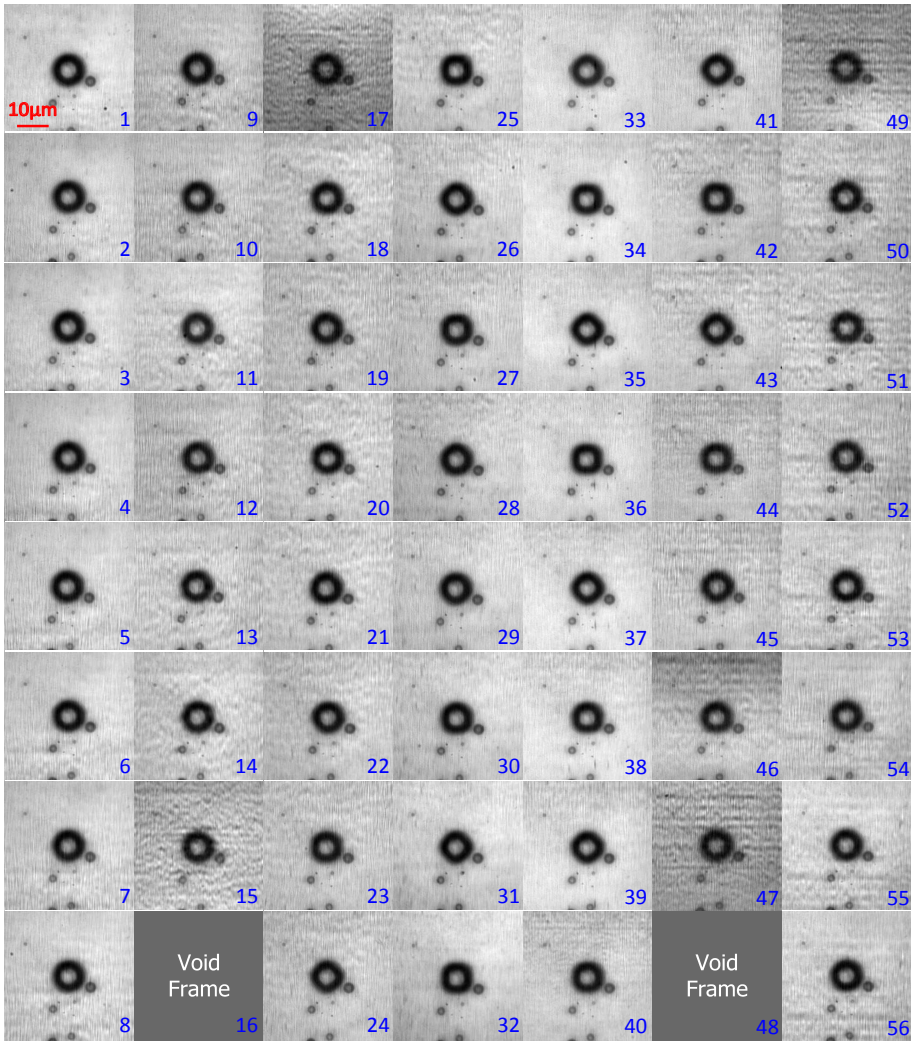

Figure 4.10: 56 first captured images from a series of 64 images. Mode 4 at 0.9 MHz and 25 kPa (25 mV) of a $\sim$ 4µm SonoVue® microbubble at 0.8 Mfps.

Surface modes estimation of a $\sim 5\mu$m radii microbubble

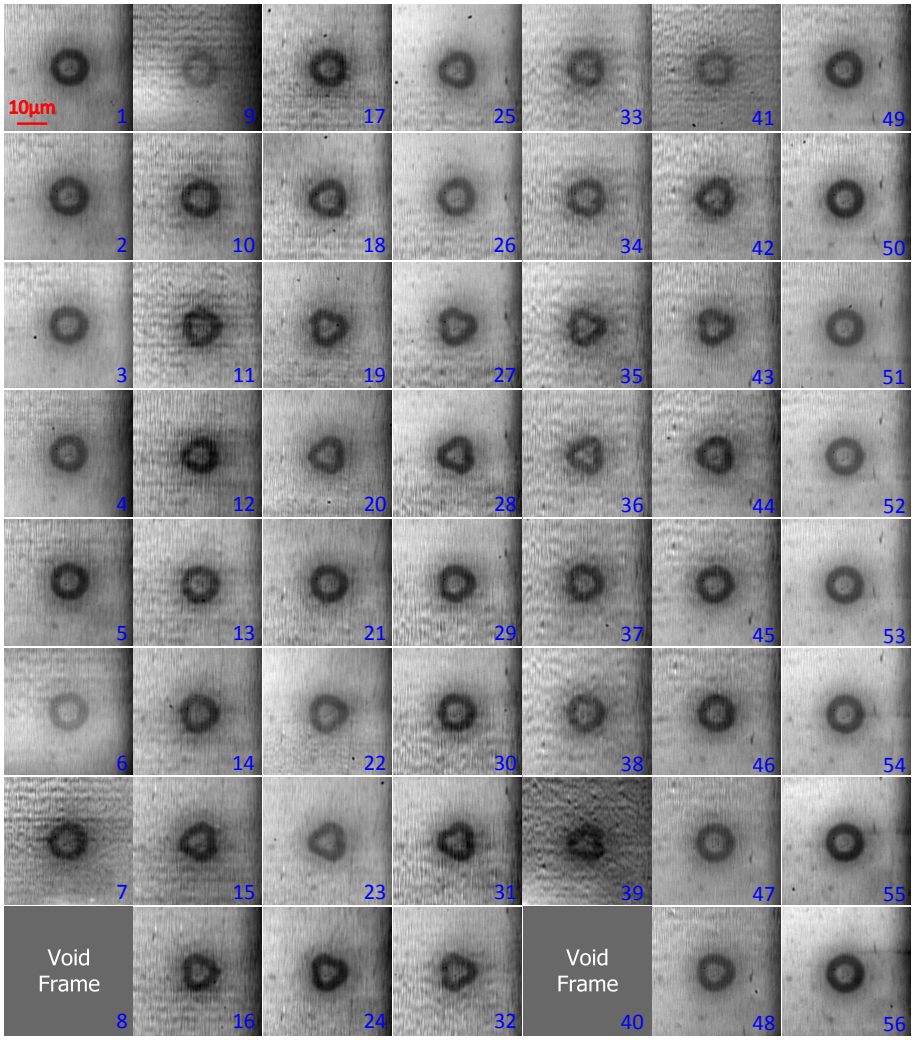

Figure 4.11: 56 first captured images from a series of 64 images. Mode 3 at 0.6 MHz and 50 kPa (130 mV) of a $\sim 5\mu$m SonoVue® microbubble at 0.8 Mfps.

In Figure 4.12 the microbubble undergoes mode 4 oscillation in frames 9 to 15. However, in frame 21 to 24 the bubble shape oscillation does not retain its mode and goes into transition. From frame 28 until the end of the excitation pressure, the bubble maintains a mode 3 shape oscillation. A loss in gas volume does not explain such transient non-linearity, as a bubble which underwent

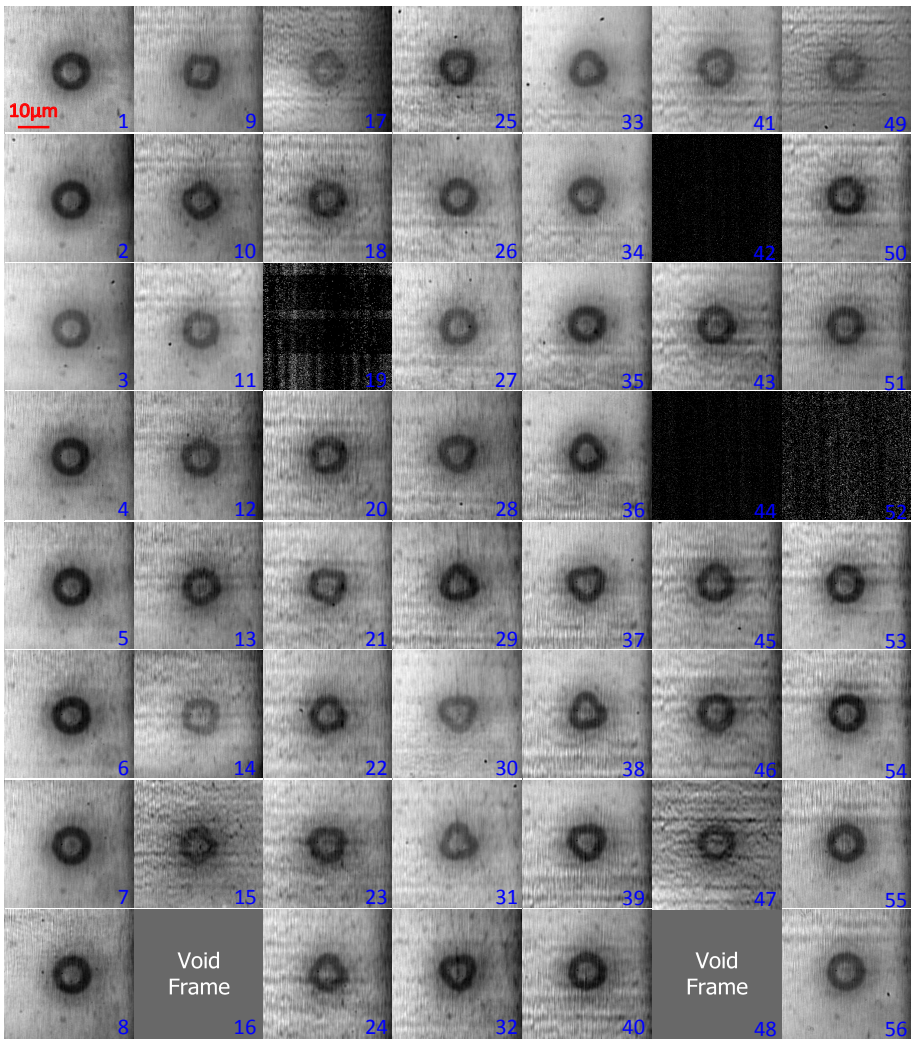

Figure 4.12: 56 first captured images from a series of 64 images. Mode 3 and 4 at 0.7 MHz and 50 kPa (105 mV) of a $\sim$ 5µm SonoVue® microbubble at 0.8 Mfps.

shrinkage would reduce its resonance frequency. If it had reduced in size, it could only change from mode 4 to 5. A change from mode 4 to 3 can be explained by either an instability in the coating or an increase in the gas volume. The latter could be possible with a sharp rise in temperature. However, at 35 kPa, heat generation from the gas compression is not expected provide such energy.

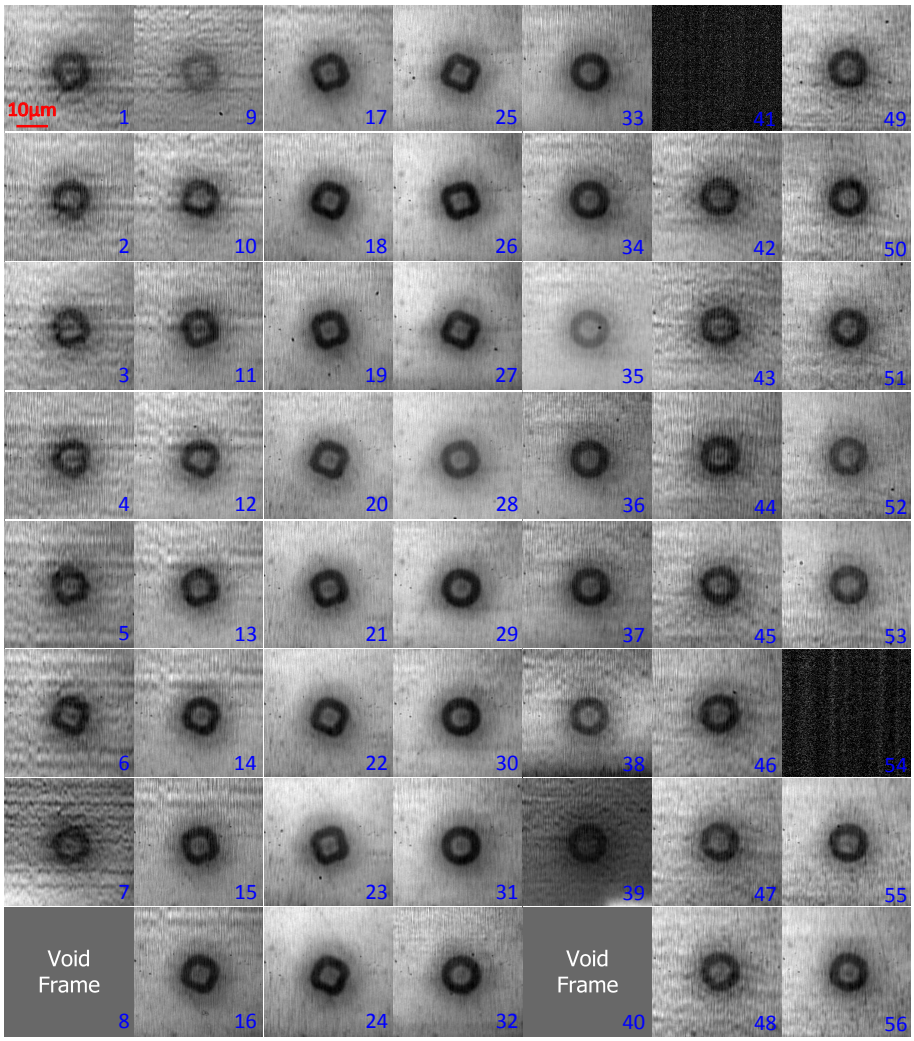

Figure 4.13: 56 first captured images from a series of 64 images. Mode 4 at 0.8 MHz and 50 kPa (100 mV) of a $\sim$ 5µm SonoVue® microbubble at 0.8 Mfps.

In Figure 4.13, although it is not straightforward to estimate the modes in

frames 1 to 16 due to artefacts which might have been caused by vibrations in the mirror rotating at 2500 rps. the following frames show clear rectangular pattern of the oscillation mode 4.

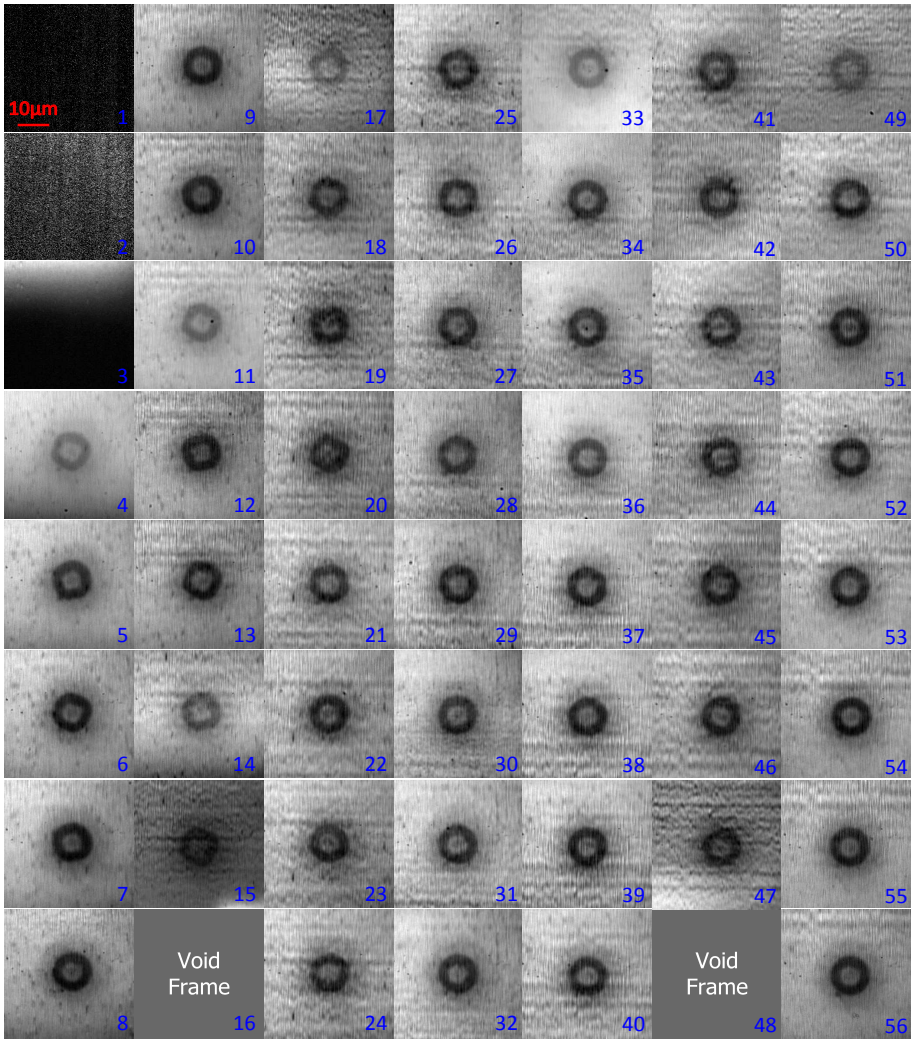

Figure 4.14: 56 first captured images from a series of 64 images. Shape oscillation at 0.9 MHz and 50 kPa (95 mV) of a $\sim$ 5µm SonoVue® microbubble at 0.8 Mfps.

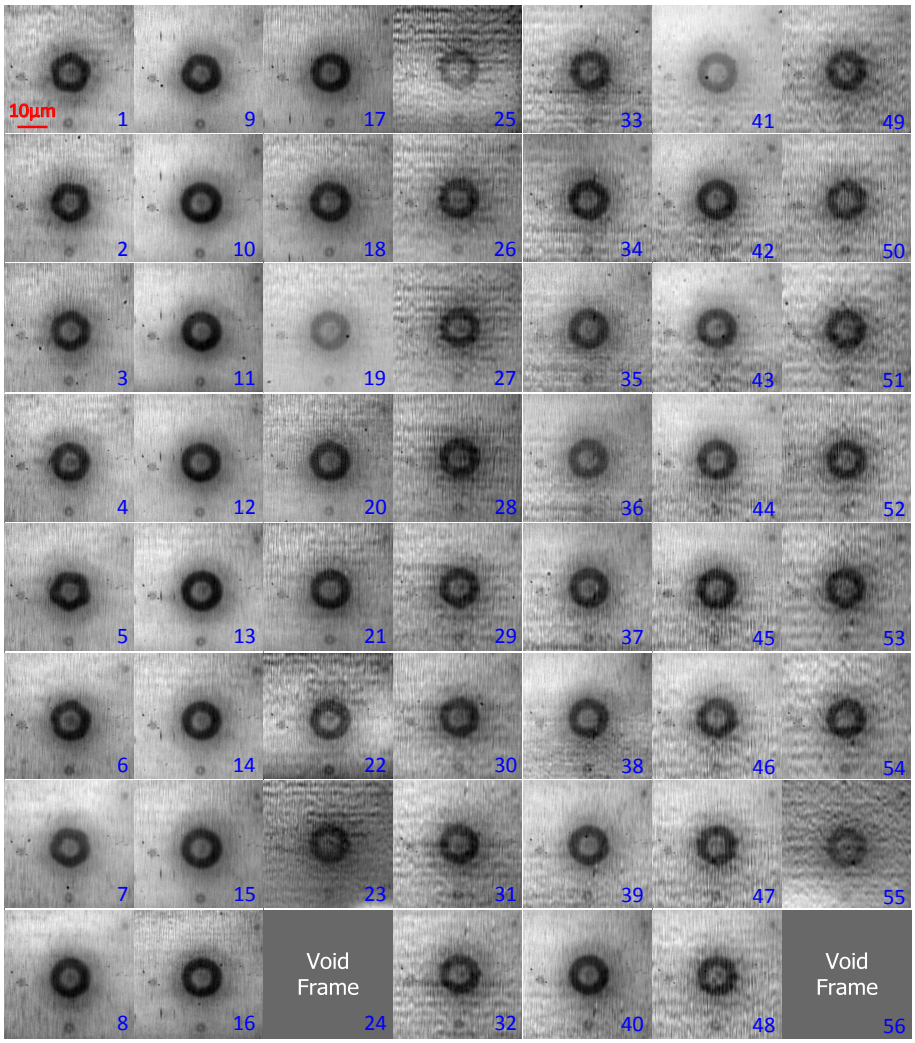

Figure 4.15: 56 first captured images from a series of 64 images. Mode 5 at 1.0 MHz and 50 kPa (90 mV) of a $\sim$ 5µm SonoVue® microbubble at 0.8 Mfps.

Surface modes estimation of a $\sim 7.5\mu$m radii microbubble

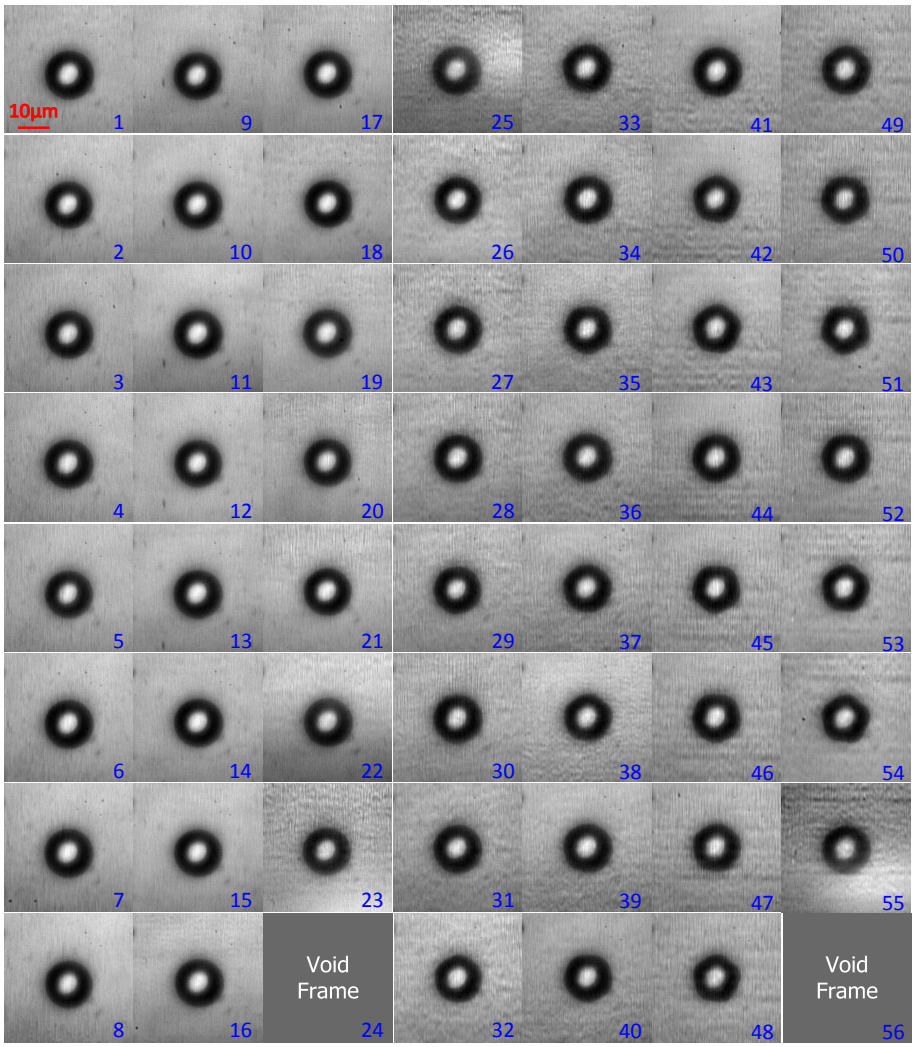

Figure 4.16: 56 first captured images from a series of 64 images. Mode 5 at 0.7 MHz and 50 kPa (105 mV) of a $\sim 7.5\mu$m SonoVue® microbubble at 2.0 Mfps.

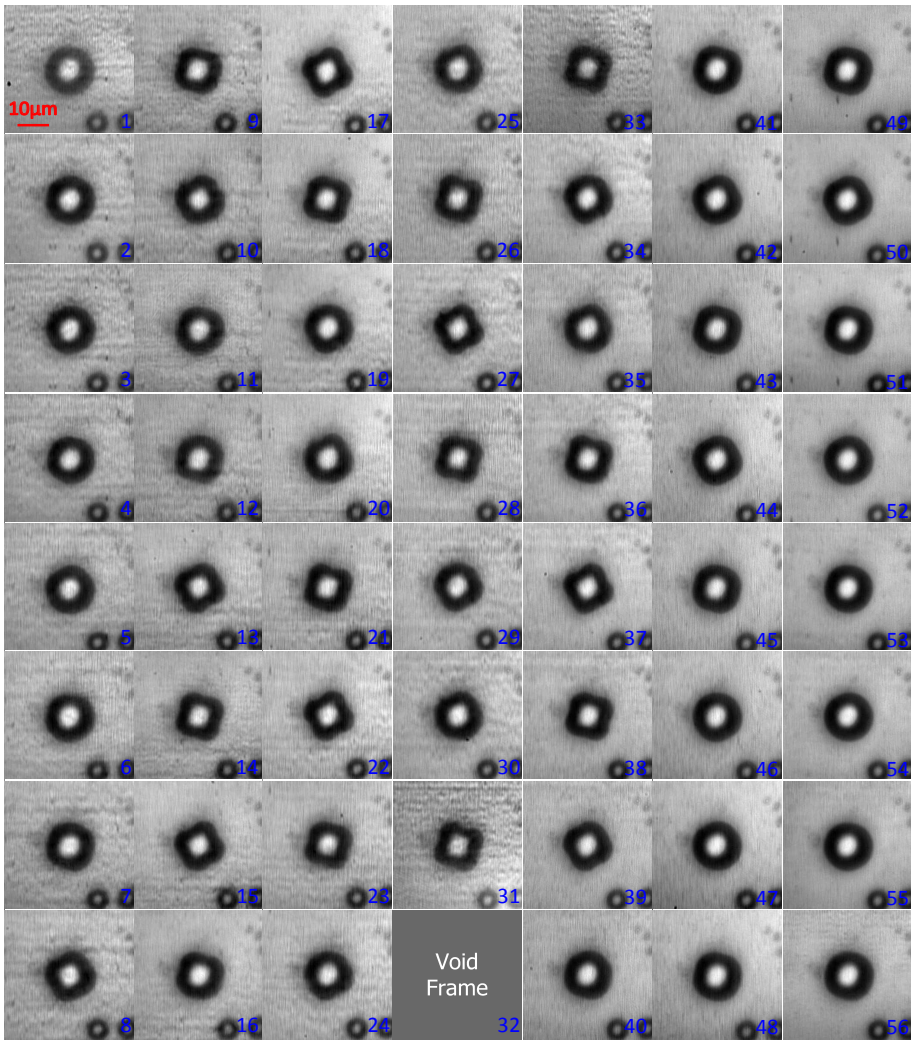

Figure 4.17: 56 first captured images from a series of 64 frames at 0.8 Mfps. Mode 4 at 0.65 MHz and 50 kPa (115 mV) of a $\sim$ 7.5µm SonoVue® microbubble.

Surface modes estimation of a $\sim 4.3\mu$m radii microbubble

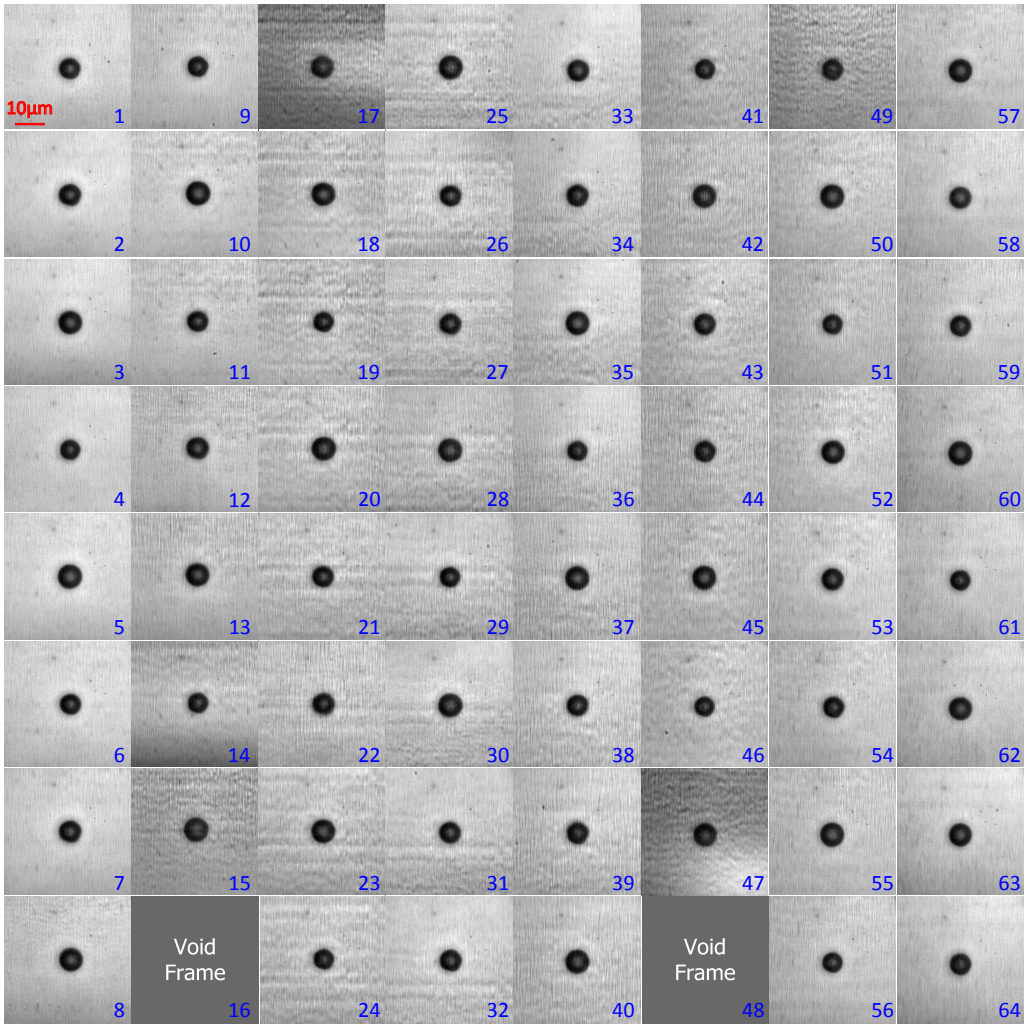

Figure 4.18: Captured images from a series of 64 frames at 2.5 Mfps. Mode 5 at 1.0 MHz and 72 kPa (130 mV) of a 4.3µm SonoVue® microbubble.

Surface modes occurring in the shells of microbubbles of the following sizes 4; 4.3; 4.5; 5 and 7.5 µm radii were estimated from optical observation. All the microbubbles probed exhibited surface modes if exited across a sufficient frequency range. The modes arose preferentially at acoustic pressures below ~100 kPa. The modes became more apparent in Figure 4.23 at 60 kPa compared to 72 kPa

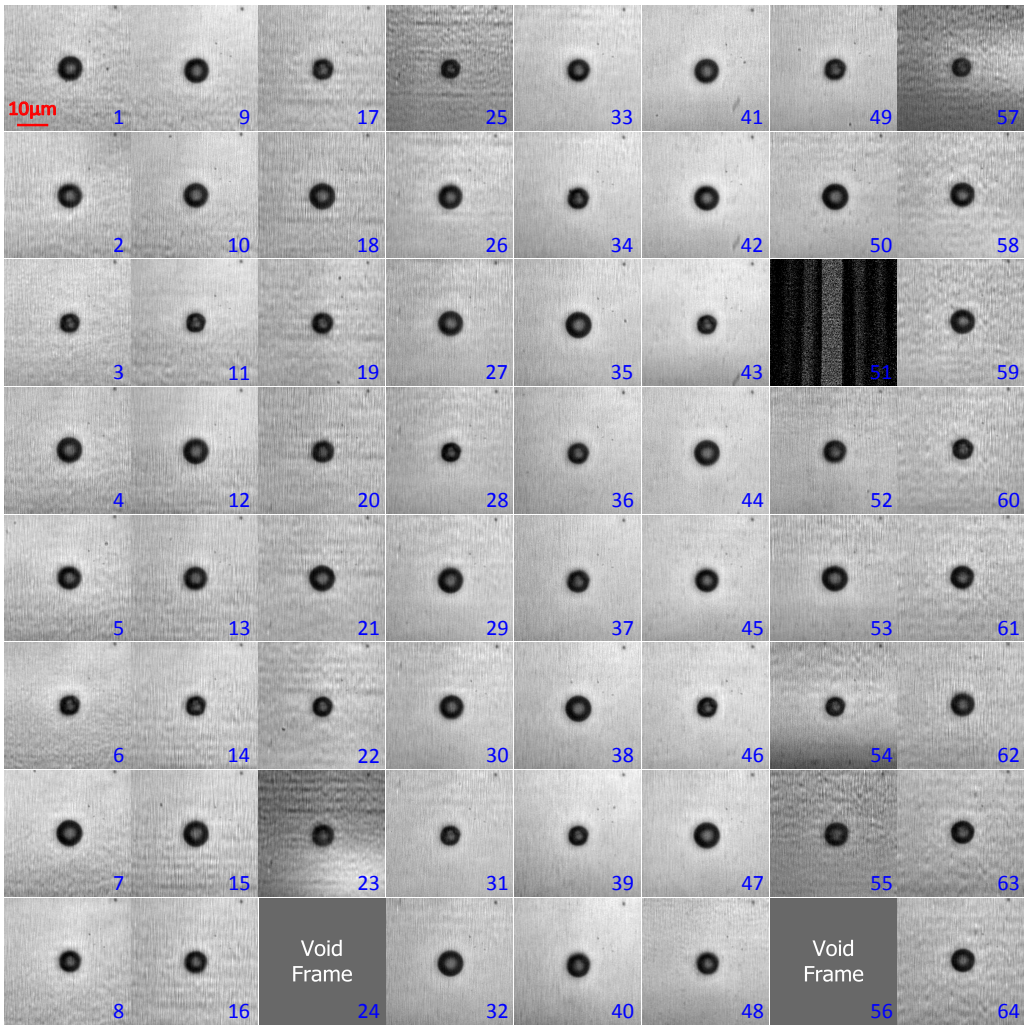

Figure 4.19: Captured images from a series of 64 frames at 2.5 Mfps. Oscillations at 0.9 MHz and 72 kPa (136 mV) of a 4.3µm SonoVue® microbubble.

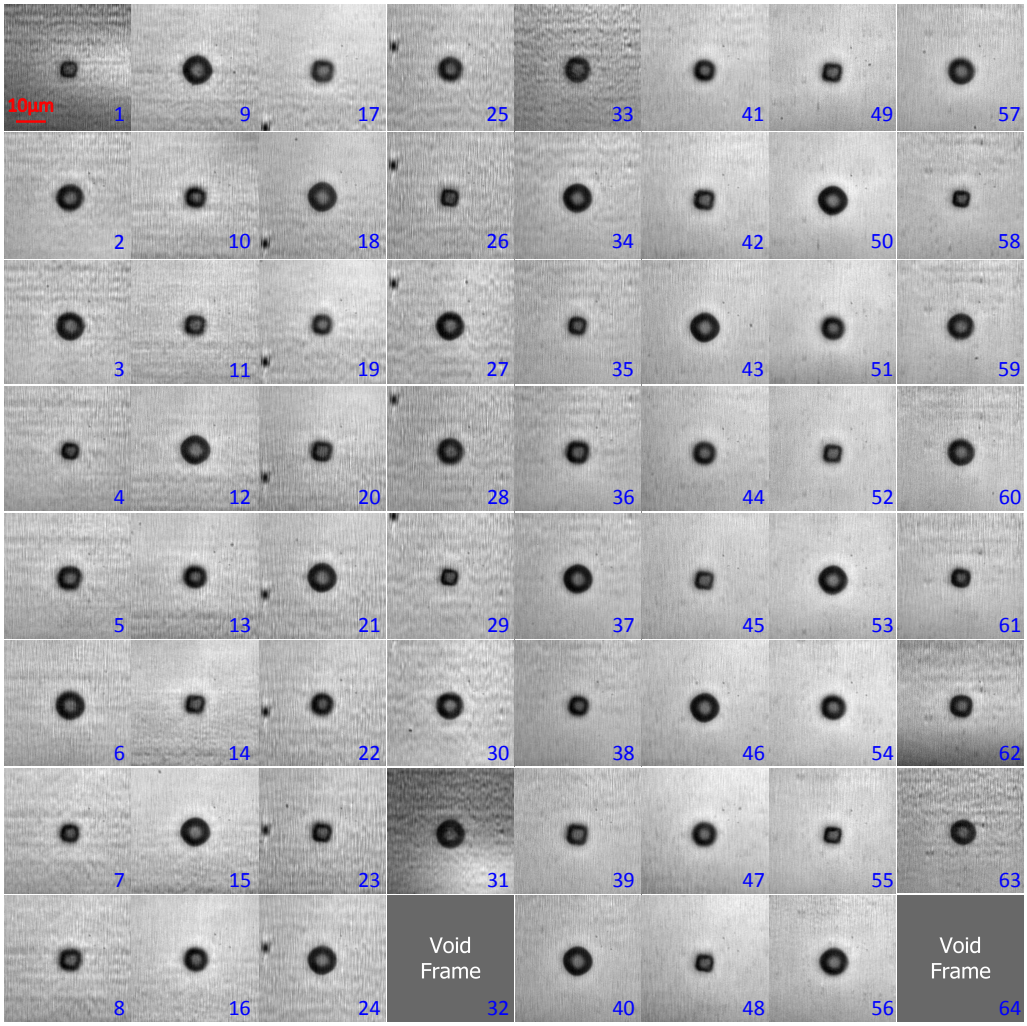

Figure 4.20: Captured images from a series of 64 frames at 2.5 Mfps. Mode 4 at 0.8 MHz and 72 kPa (140 mV) of a 4.3µm SonoVue® microbubble.

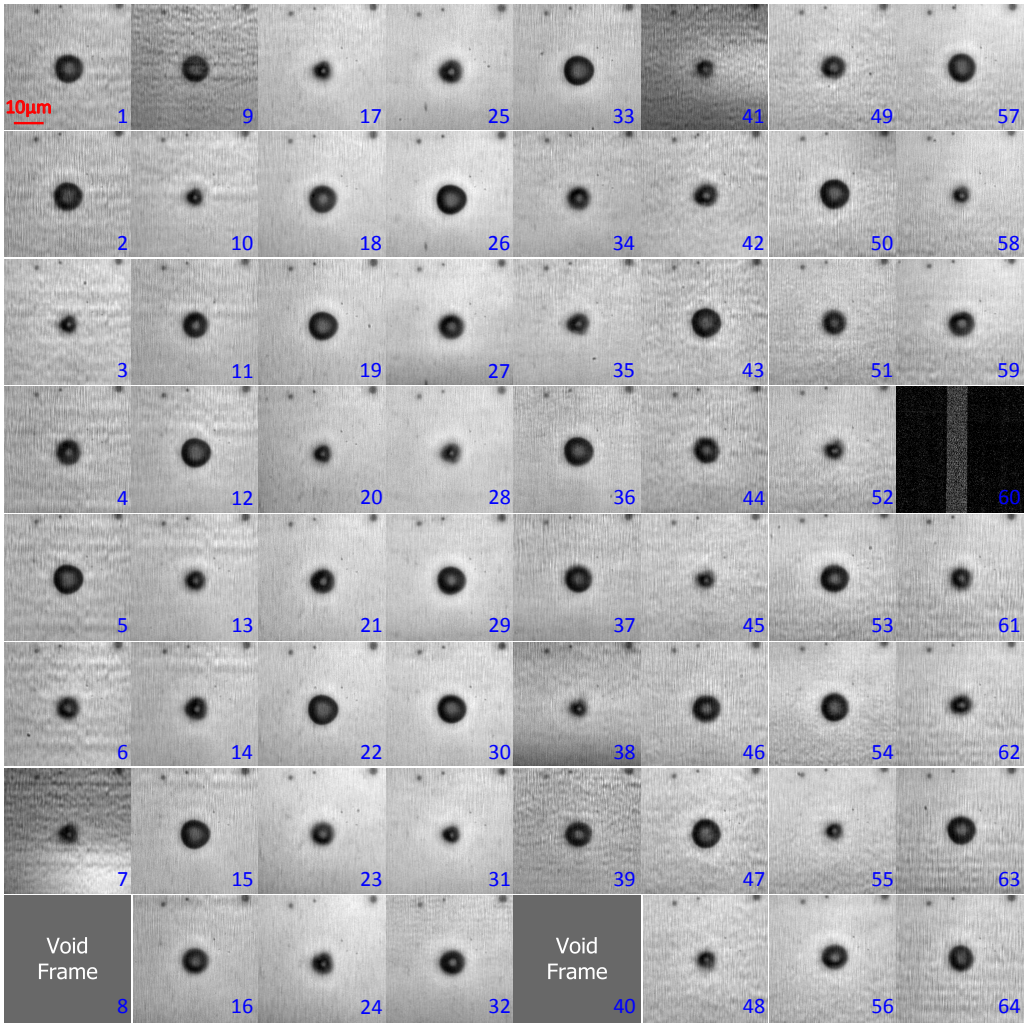

Figure 4.21: Captured images from a series of 64 frames at 2.5 Mfps. Mode 3 at 0.75 MHz and 72 kPa (141 mV) of a 4.3µm SonoVue® microbubble.

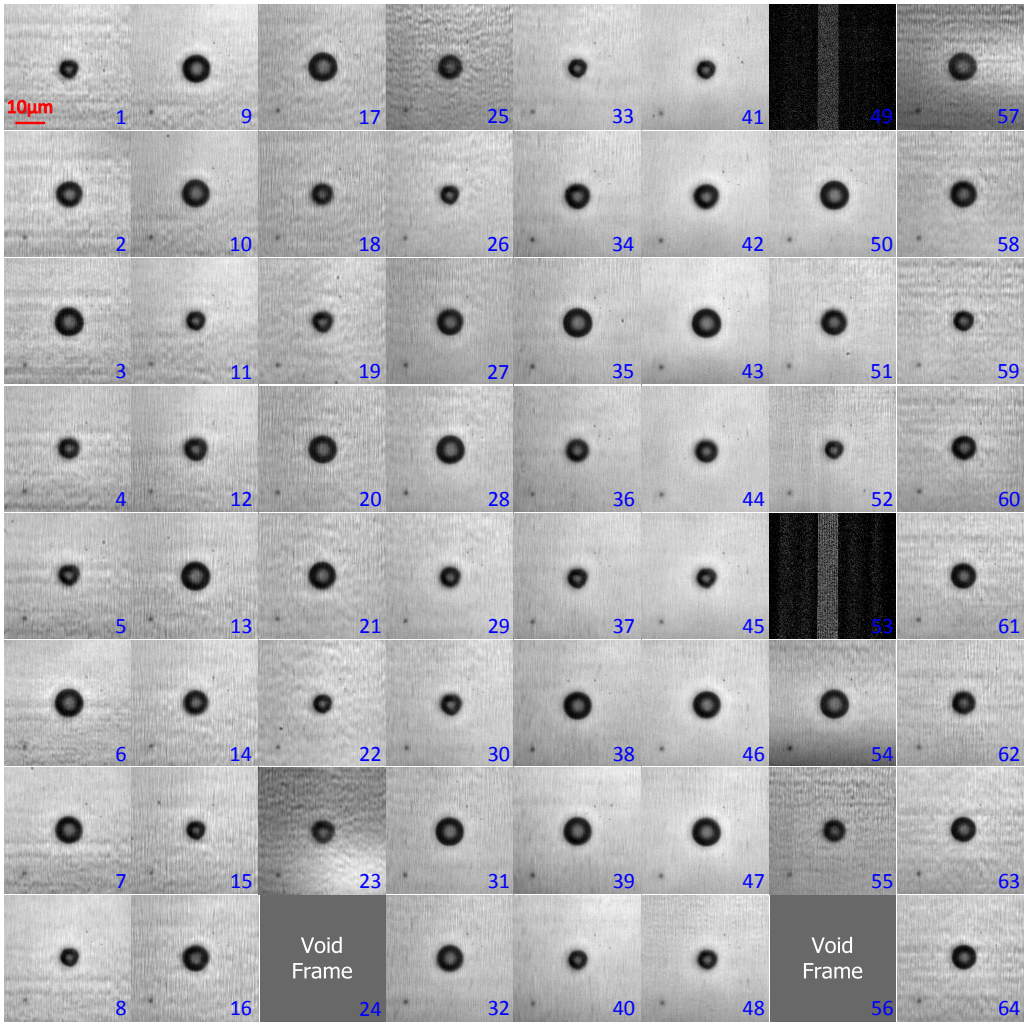

Figure 4.22: Captured images from a series of 64 framesat 2.5‘Mfps. Mode 3 at 0.7 MHz and 72 kPa (143 mV) of a 4.3µm SonoVue® microbubble.

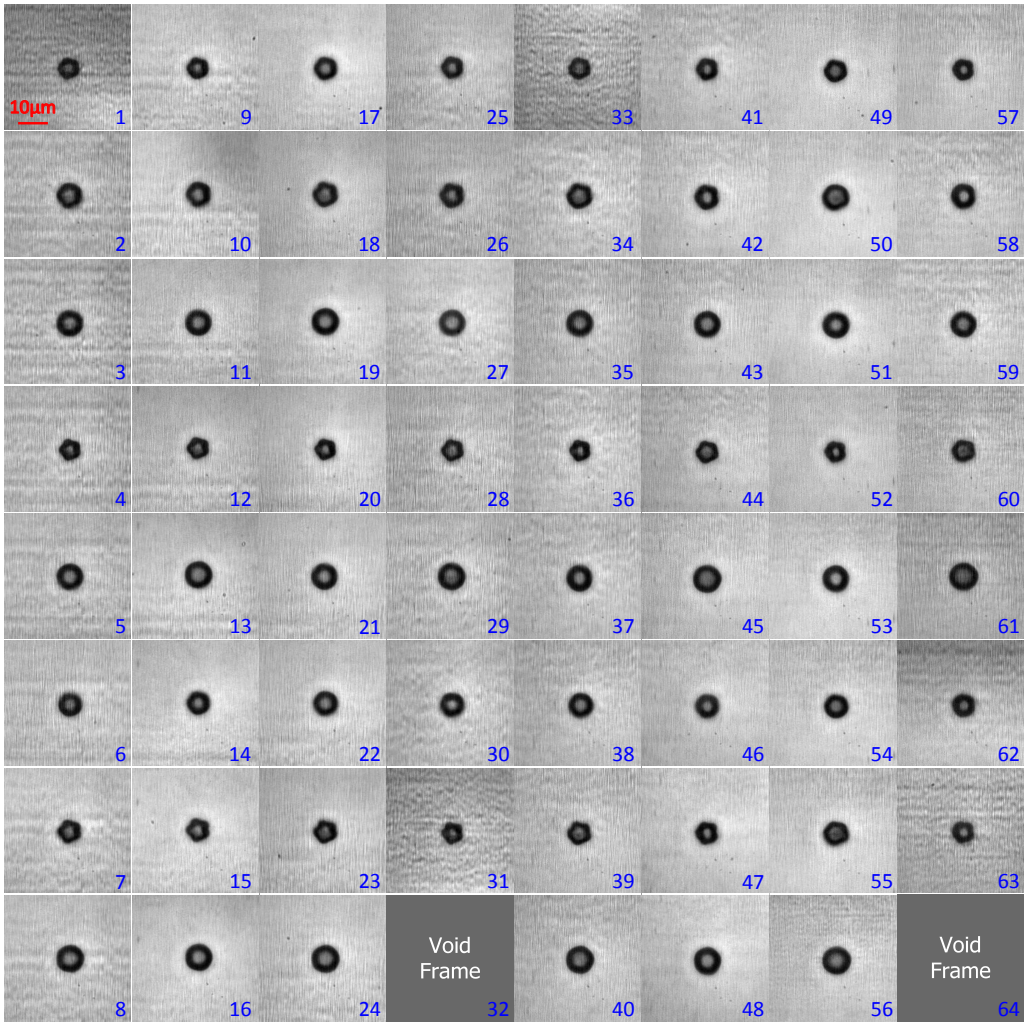

Figure 4.23: Captured images from a series of 64 frames at 2.5 Mfps. Mode 5 at 1.0 MHz and ∼60 kPa (110 mV) of a 4.5µm SonoVue® microbubble.

in Figure 4.18, although a slightly different bubble size was estimated in the latter Figure. The effect of the pressure on the microbubble surface mode becomes more apparent when the mode amplitudes from the Figures 4.18 to 4.21 are compared to Figures 4.11 to 4.15 as the 50 kPa acoustic pressure was more effective at producing the modes than the 72 kPa acoustic pressure . However, at lower acoustic pressure of 25 kPa observed in the Figures 4.8 to 4.10, although modes of comparable amplitudes than of those at 50 kPa were produced, the modes appeared only in the last 16 frames before the end of the 50µs insonating tone burst of 40 cycles. At 0.8 Mfps, a duration of 1.25 µs lasts between each frame, therefore during the first 30µs, 60% of the insonation time, no modes or oscillation were observed. At the higher pressure of 50 kPa, in Figures 4.11 and 4.12, surface modes were observed for 40µs corresponding to a 60% and 70% of the insonation time. This emphasizes the number of excitation cycles necessary before modes are observable depends on the applied pressure. An increase in pressure contributes to a higher proportion of the insonation time to generate observable surface modes. An exact increase is however not estimated due to the limited statistical sample and to the time aliasing occurring at 0.8 Mfps for a 0.6 to 0.8 MHz insonation frequency. Additionally, the camera does not trigger the CCDs sensors with sufficient accuracy to obtain observable results, and often clipping the onset of modes (see Figure 4.13, 4.14 and 4.15).

In Figure 4.24, the observations of the 9 individual SonoVue® using high-speed imaging are recapitulated. The observed surface mode order n is plotted against the excitation frequency f. Microbubbles which did not undergo through a stable surface mode oscillations are annotated with a black circle. Those measurements include the microbubbles that had non-spherical oscillations that did not correspond to a mode order. The occurrence of surface modes has an observable relation to the resonance frequency; with modes of the larger microbubbles occurring at lower frequencies than modes of the smaller ones. Thus, under the same environment and excitation field the occurrence of a mode number can become predictable. In Figure 4.23, a 4.5 µm was excited with a 60 kPa 1.0 MHz 20 µs tone burst. The microbubble underwent surface modes of the 5^{th} order, a mode previously observed in Figure 4.18 at 72 kPa although the microbubble

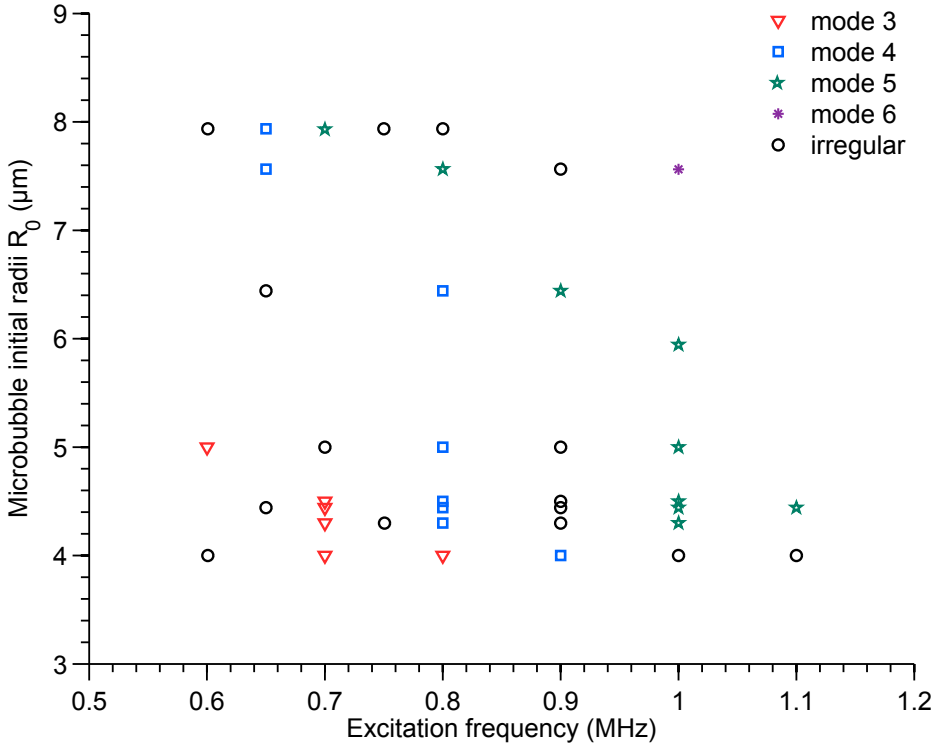

Figure 4.24: Estimated frequencies at which the surface modes occurred for microbubbles of sizes 4; 4.3; 4.5; 5 and 7.5 μm in radii

had a slightly smaller radii of 4.3 μm, which might explain the difference in amplitude of the mode observed. This will be confirmed by the observation made analytically in Section 4.3.2.

Gelderblom (2012) estimated the error in radii measurement of single microbubbles with fluorescence imaging 4 times lower than with bright field imaging. Also, when the method of focusing was not refined enough, the out-of-focus error for bright field measurements would be larger than with fluorescence imaging. Gelderblom found a systematic offset of 0.25 μm in the microbubble measurement independent of the measured microbubble size. Gelderblom attributed this offset to the light diffraction and scattering with the microbubble's lipid shell and inner gas. However the offset was expected to be dependent on the optical system of the experimental setup and could not be a referential value applicable to other studies.

4.3 Finite element modelling of surface modes

Using a 80 kPa plane wave ultrasound acoustic field, the appearance of modes in the microbubble coating were observed using the model described in the chapter 3. The averaged surface displacement dS_{avg} defined in equation 3.35 is employed here to study the shell amplitude displacements of microbubbles undergoing surface modes oscillations. In the following Figures 4.25 and 4.26, dS_{avg} is normalized by the initial radii R_0. The excitation frequency was swept from 0.5 MHz to 1.4 MHz using an increment of 0.0125 MHz.

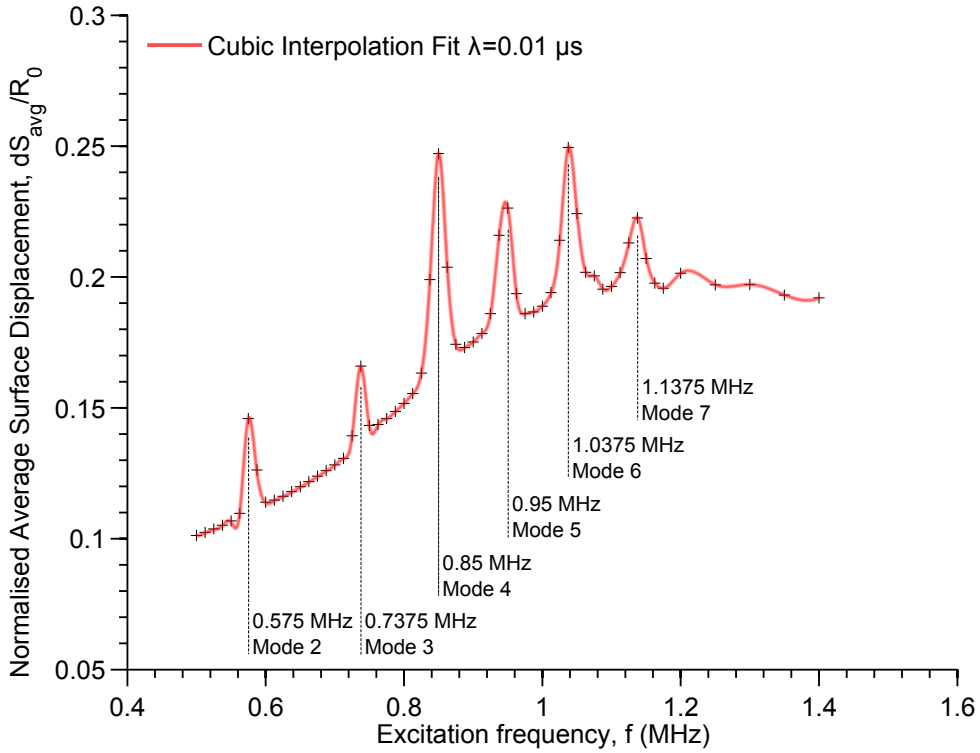

Figure 4.25: Normalised absolute average surface displacement of a 4.0 μm radii microbubble at p_0=80 kPa. The following simulation parameters were used: E=115 MPa, λ=0.01 μs, η=0.45 Pa.s. Each point is calculated with the formula 3.35 at a frequency f. The microbubble surface modes corresponding to each annotated peak displacement are shown in figures 4.27 and 4.28.

The normalised and averaged surface displacement dS_{avg}/R_0 increases as a

microbubble exhibits a surface mode, thus enabling the estimation of the frequencies at which surface modes appear. The mode order can observed through a 3-dimensional displacement plot of the coating material.

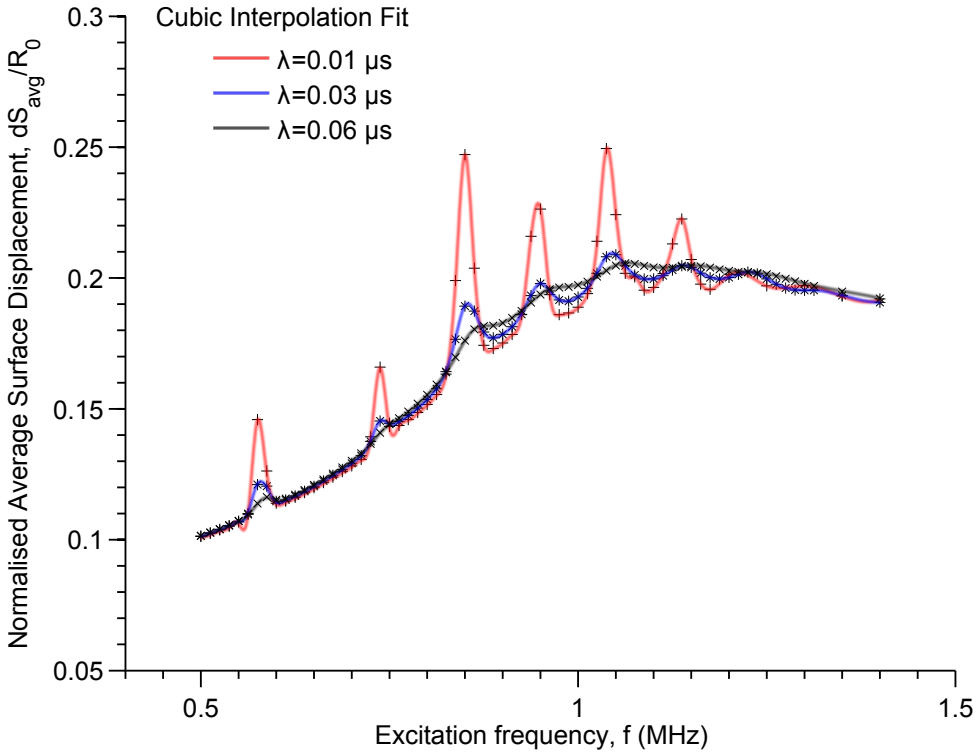

Figure 4.26: Normalised absolute average surface displacement of a 4.0 μm radii microbubble at p_0=80 kPa. The following simulation parameters were used: E=115 MPa, η_1=0.45 Pa.s. $+$: λ_1=0.01 μs, $*$: λ_1=0.03 μs, $\times$: λ_1=0.06 μs.

In Figure 4.27, the lower mode orders 2, 3, 4 and 5 were observed at the phases of 0 rad and π rad of the acoustic field. The higher orders 6, 7 and 8 are shown in Figure 4.28. Each surface modes correspond to a peak displacement observed in Figure 4.25.

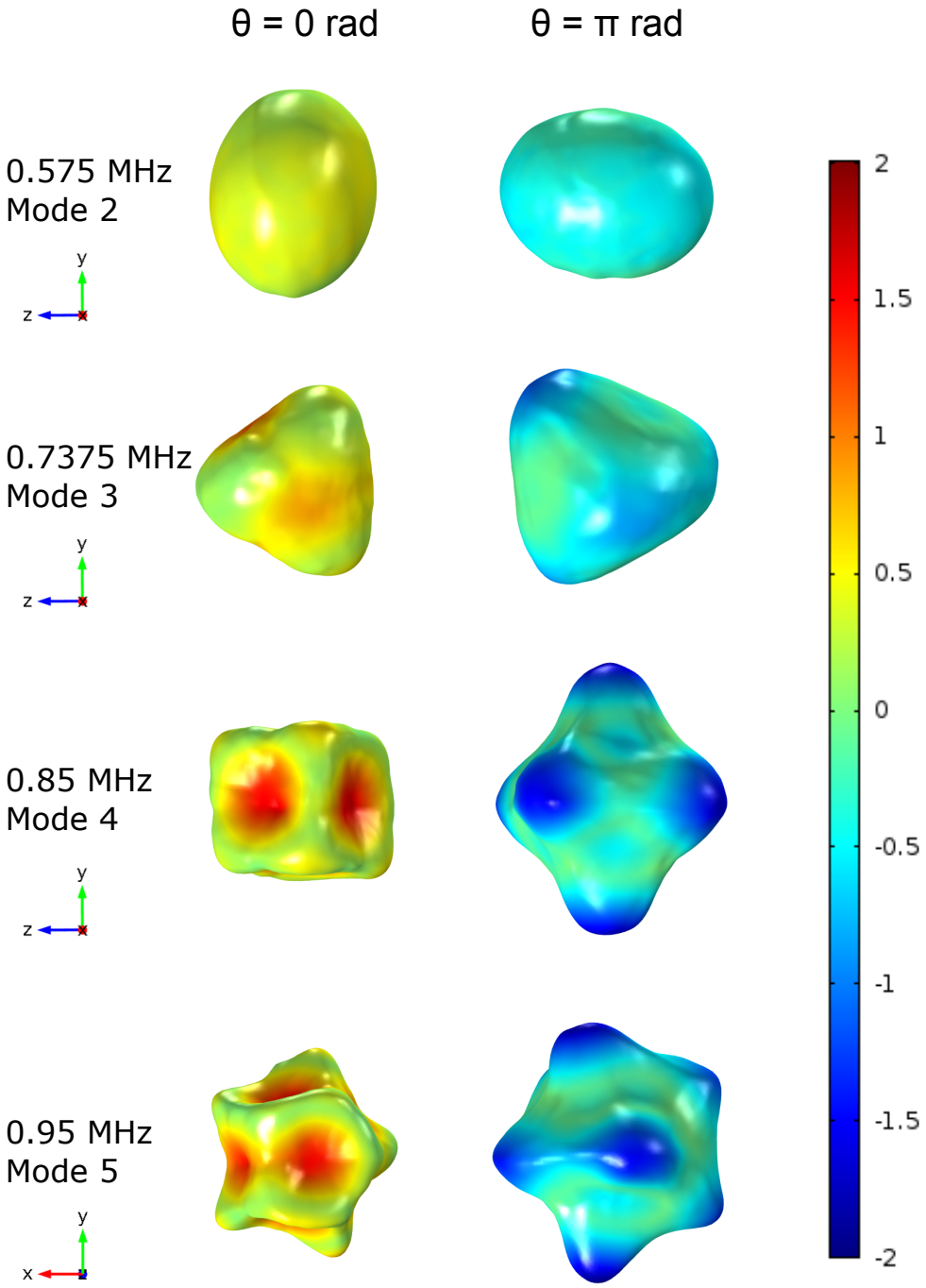

Figure 4.27: Surface amplitude displacement in μm of a 4.0 μm radii microbubble at 80 kPa. The following simulation parameters were used: E=115 MPa, λ_1=0.01 μs, η_1=0.45 Pa.s .

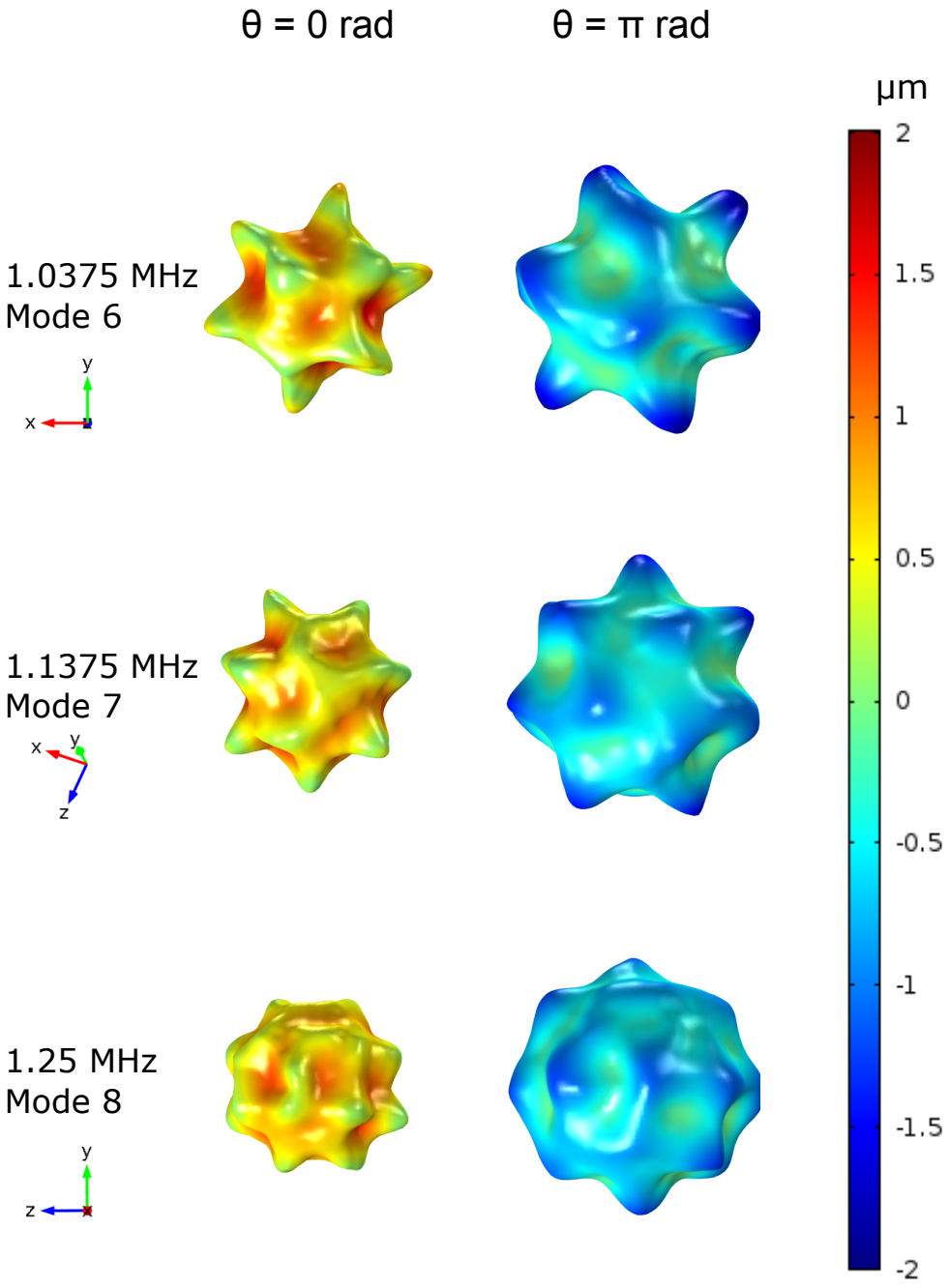

Figure 4.28: Surface amplitude displacement in μm of a 4.0 μm radii microbubble at 80 kPa. The following simulation parameters were used: E=115 MPa, λ_1=0.01 μs, η_1=0.45 Pa.s .

4.3.1 The effect of the relaxation time λ_1 on the surface modes

In Figure 4.29, an observation of the excitation at 0.5 MHz of a 5.4 μ radii microbubble reveals its characteristics. It was discussed previously in chapter 3 the resonance of a microbubble is maintained when the relaxation time λ varies. The microbubble oscillation mode shape becomes more defined for small relaxation times since the mode amplitude becomes increasingly elevated.

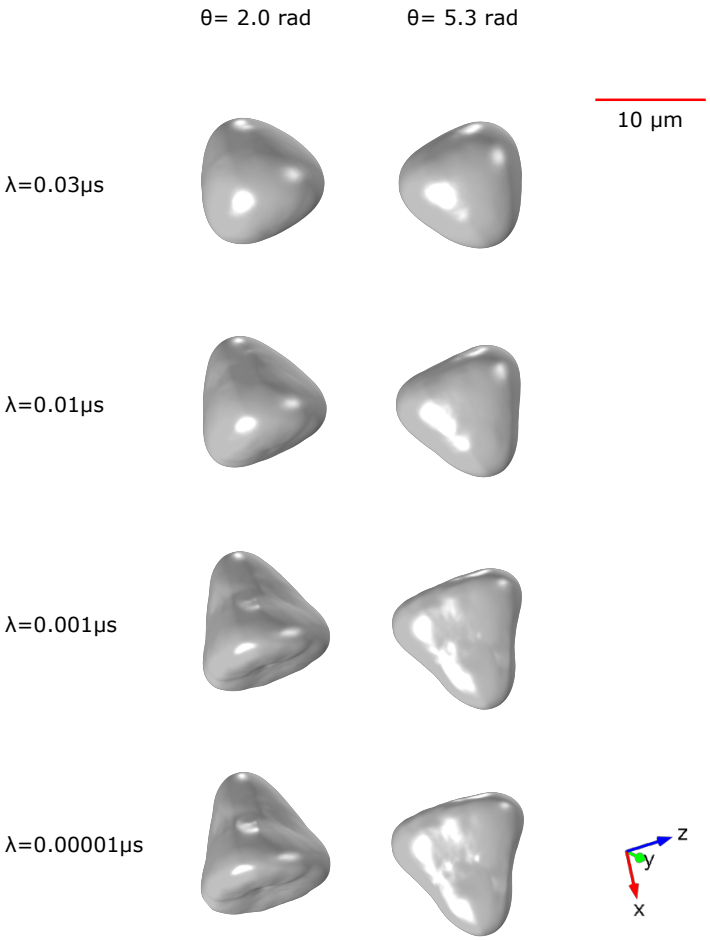

Figure 4.29: Oscillation mode of a 5.4 μm radii microbubble at 0.5 MHz and an excitation pressure of 100 kPa. For a decreasing relaxation time λ_1, the mode amplitudes increase.

This relation between the mode amplitude and the relaxation time is related to the viscous and elastic behaviour of the shell. As presented in chapter 2, the relaxation time defines the time required to the molecules to reach an equilibrium. Remembering that the viscosity is related to the non-equilibrium shear modulus G_1 and the relaxation time λ_1 with $\eta_1 = G_1\lambda_1$. The relaxation time λ_1 is therefore related to the viscosityη_1 which represents the amount of shear flow resistance. For small relaxation times, η_1 is smaller compared to longer relaxation time. In Figure 4.29, as the relaxation time becomes smaller, the viscosity of η_1 is reduced. Therefore the shell of a microbubble is less viscous at a relaxation time of 0.001 µs than at 0.03 µs. Ultimately, further reduction of the relaxation time from 0.001 µs to 0.00001 µs has a small impact on the mode amplitude. With shorter relaxation times the rheological material becomes less viscous similar to a non-viscous liquid whose molecules diffuse rapidly with limited resistance to shear flow.

4.3.2 Estimation method for surface mode order

To estimate the modes of a microbubble in an acoustic field, the angular displacement of the shell $R_{disp}(\theta)$ is calculated from each cross Sections normal to the vectors (1,1,1), (0,0.5,0.5) and (0.5, 1, 0.5) of the Cartesian coordinate system; with the centre of the microbubble at the origin of the coordinate system. The aim is to ensure modes are estimated with sufficient accuracy since a single cross Section may fail to display the correct mode order at some frequencies. With $\hat{R}(n) = 1/2\pi \int_0^{2\pi} R_{disp}(\theta) e^{in\theta} d(\theta)$ the Fourier spectrum was calculated (Dollet *et al.*, 2008):

$$|An| = \sqrt{\hat{R}(n)\hat{R}(n)^*} \tag{4.3}$$

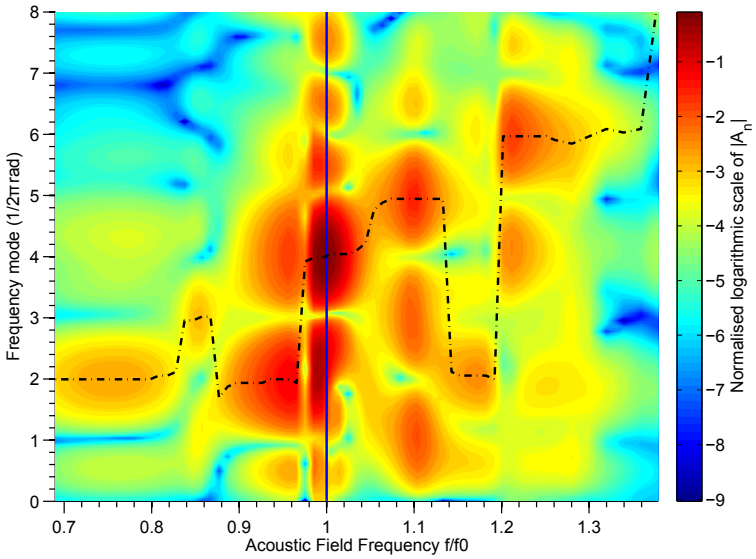

Figure 4.30: Amplitude of the modes for a range of acoustic frequency of f/f_0 with χ_{eq}= 0.58 N/m and $\kappa_{eq} = 3.6e^{-9}$ kg/s. The black dotted line represents the maximum at each acoustic field insonation frequency.

4.4 Finite element modelling of shell modes near boundaries

The change of resonance frequency of a bubble near a hard boundary is well documented in the literature. The resonance frequency and the modes eigenfrequencies decrease for a decreasing separation distance d between a bubble and a rigid boundary (Xi *et al.*, 2014). This effect is non-negligible for distances d smaller than the bubble radii R_0 as the boundary reflects the acoustic pressure re-emitted by the oscillating bubble similarly to a mirrored bubble oscillating in phase (Payne *et al.*, 2005). However, in this Section the microbubbles are positioned near an elastic or viscoelastic boundary. Doinikov *et al.* (2011) demonstrated while the resonance of microbubbles are reduced in the presence of a rigid boundary, the opposite happened in the presence of an elastic boundary. Likewise, an increase of the resonance frequency and the modes eigenfrequencies is expected for a microbubble near a viscoelastic boundary.

4.4.1 The microbubble in the vicinity of a thick elastic boundary

The overall conditions used in the experiment can be compared to a bubble near a vibrating plate. The ultrasound hits the Poly(methyl methacrylate) (PMMA), which in turns re-emits sound by vibrating vertically, normal to the plate. The boundary acts as a plate and the solutions to its mechanical behaviour are those of guided wave propagation.

Methods

In the experimental setup, an Ibidi® chip with a single channel is used. The chip has 1 mm thick top layer through which the ultrasound propagates before insonating the microbubbles underneath. The ultrasound is this instance necessary re-emitted through the vibrations of the PMMA layer to liquid medium beneath it. A thickness of $e_{\text{PMMA}} = 180\mu\text{m}$ is chosen to model the material instead of the

1 mm of the experimental conditions encountered in chapter 4.2.2. The aim is to reduce the computational complexity of the finite element model since modelling the effects contributed by 1 mm thick boundary would contribute to not less than quadrupling the necessary volume to accommodate enough space for the acoustic wave field to travel through the liquid medium before driving the material layer. As a result, the aforementioned problem assumes the thickness of the modelled PMMA layer has a negligible impact on the results. The simulation parameters that were adopted are listed in table 4.2.

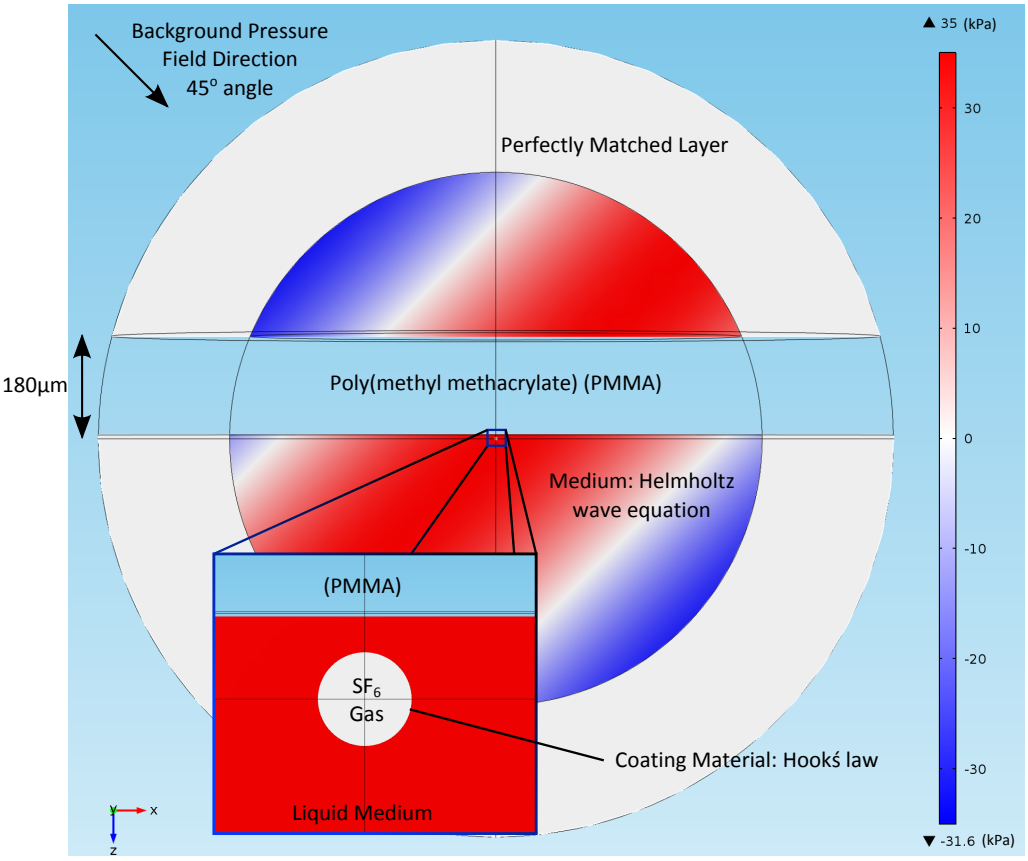

Figure 4.31: Planar cut of the 3 dimensional Comsol Multiphysics® model.

Table 4.2: Simulation Parameters

Entity	Value
Microbubble shell Young's modulus, E	115 MPa
Microbubble shell viscosity, η_1	0.45 Pa.s
Microbubble shell relaxation time, λ_1	0.01 µs
Pmma Young's modulus, E_{PMMA}	3 GPa
Pmma layer thickness, e_{PMMA}	180 µm
Separation distance, d	2 µm

FE modelling results and comparison to experimental results

Comparison of the experimental data to the finite element modelling results is feasible with the optical frames of the 4.0 µm radii microbubble discussed in Section 4.2.3 and the computed surface displacement of the model using the identical viewing angle —*i.e.* the vertical direction $\mathbf{z}$ pointing downwards, towards the observation point—.

The comparison to the experimental results with the solutions of the model is shown in Figure 4.32 at the insonation frequency of 0.8 MHz, and in Figure 4.33 at the insonation frequency of 0.9 MHz. The selected frames were taken from experimental data previously displayed in Figures 4.9 and 4.10. In the FE model, the ultrasound direction was computed for the direction $\{\mathbf{x}, \mathbf{y}, \mathbf{z}\} = \{1, 1, 1\}$. The model's observation plane was rotated to conform with the experimental observation taken relative to the ultrasound direction. Both Figure show good agreement for an interval of 3 rad $\approx \pi$ rad which corresponds to the time interval between the two successive frames taken by the high speed camera at 0.8 Mfps.

The results allow to conclude that the correct assumptions were taken to model the physics of the surface modes. However, the elevated elastic parameter E of 115 MPa compared to the value found in the Section 3.3.3 could be due to the reduced thickness of the Pmma layer of 180 µm instead of the 1 mm present

in the experiment. Similarly, the effect of the layer elasticity E_{PMMA} was not accessed, but could have affected the results. Moreover, the separation distance d between the microbubble and the boundary was not assessed and an assumed value of 2 μm was used. A smaller separation distance could have avoided the elevated elastic parameter.

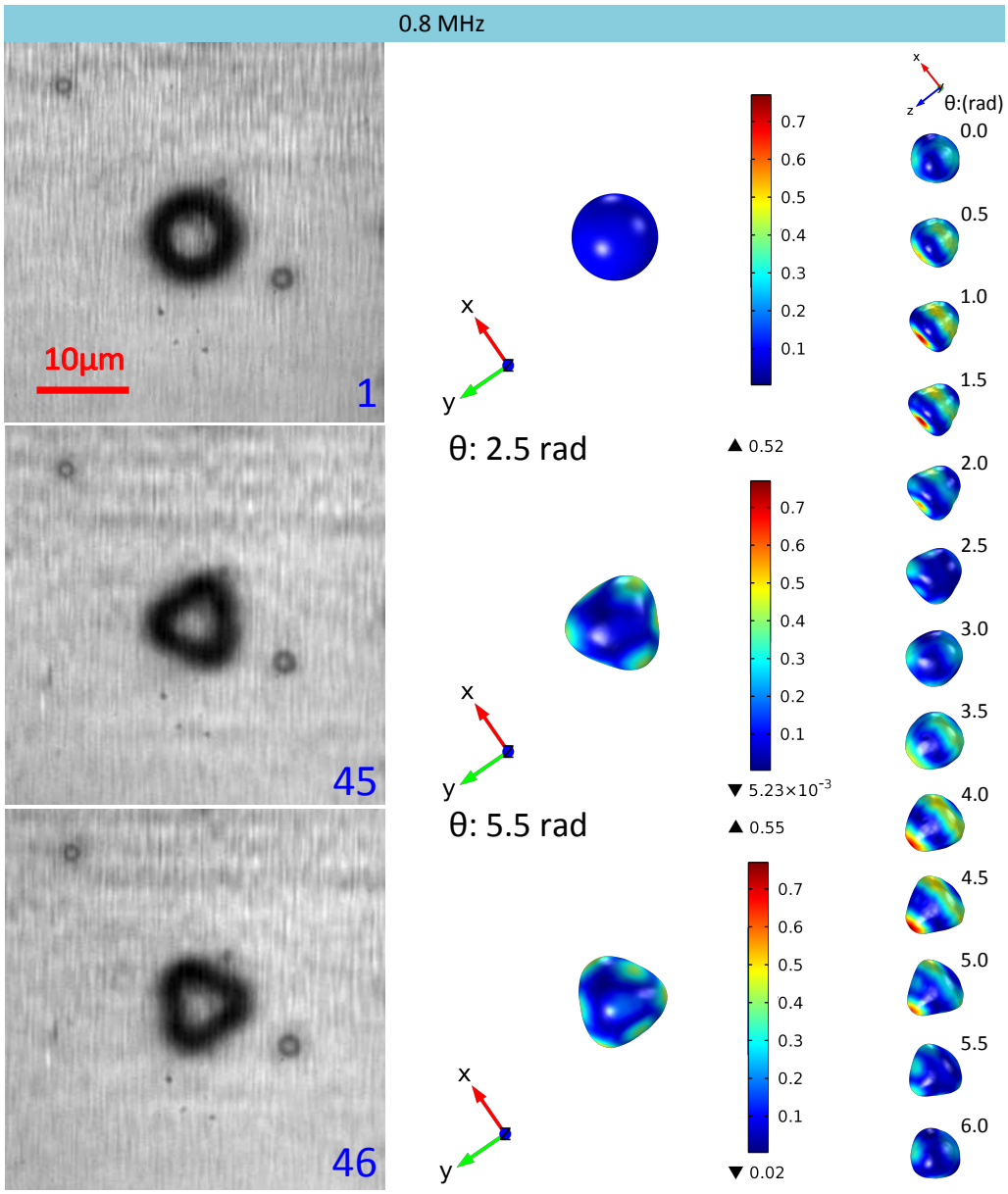

Figure 4.32: A 4 µm radii microbubble at 0.8 MHz. Frames 1, 45 and 46 from the experimental data previously presented in Section 4.2.3, Figure 4.9. The microbubbles were both observed from the bottom view. Used simulation parameters are presented in table 4.2.

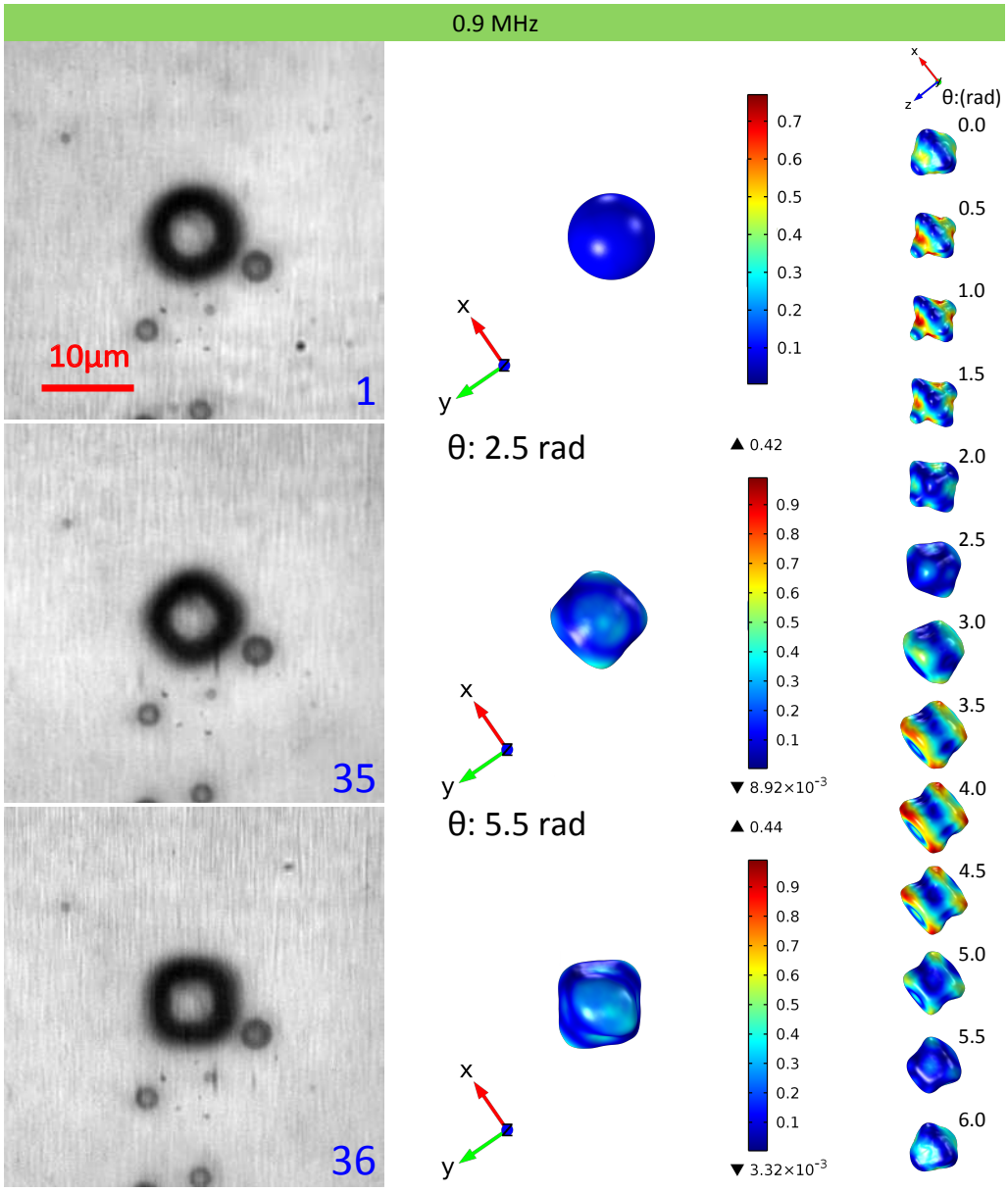

Figure 4.33: The identical 4 µm radii microbubble from Figure 4.32 at 0.9 MHz. Frames 1, 35 and 36 from the experimental data previously presented in Section 4.2.3, Figure 4.10. Used simulation parameters are presented in table 4.2.

4.4.2 The microbubble in the vicinity of a thin viscoelastic boundary

The effect of viscoelastic membrane in the vicinity of a microbubble is still poorly understood. Doinikov *et al.* (2009a) analysed the theoretical dynamics of microbubbles in the vicinity of a rigid boundary and the identical boundary was modelled in the case of a cell membrane (Doinikov & Bouakaz, 2010a). This Section will firstly present the assumption taken for the viscoelastic boundary for modelling a cell membrane and secondly discuss the effect of the distance separating from a microbubble to the a viscoelastic membrane on the microbubble dynamics.

Methods

Table 4.3: Simulation Parameters

Entity	Value
Microbubble shell Young's modulus, E	115 MPa
Microbubble shell relaxation time, λ_1	0.07 µs
Microbubble shell viscosity, η_1	0.6 Pa.s
Membrane Young's Modulus, E_{mem}	3773 Pa
Membrane relaxation time, $\lambda_{1,mem}$	0.1 µs
Membrane shear viscosity, $\eta_{1,mem}$	1.3 Pa.s
Membrane thickness, e_{mem}	500 nm

The viscoelastic membrane is modelled with the SLS of Maxwell form previously presented in chapter 3 and similarly to the modelling of the Pmma layer, the membrane spans across the whole simulation domain. The model simulation parameters are listed in the table 4.3. In addition to the thin thickness of $e_{mem} = 500$ nm, the viscoelastic membrane was chosen to have a relative

low elastic parameter of E_{mem} = 3773 Pa to mimic the presence of a flexible membrane. This approach is taken in the view of the two-dimensional elasticity $Y = E_{mem} \times e_{mem}$ previously discussed in Section 3.4, which is dependent of the thickness and the elasticity. The smaller the elastic modulus and the thinner the membrane, the more bendable the membrane becomes. The relaxation time $\lambda_{1,mem}$ value was determined to allow convergence to a solution across the wide range of frequencies of 1 to 6 MHz. The parameters $\lambda_{1,mem}$ and $\eta_{1,mem}$ are of the same order of magnitude of the values measured experimentally ($\lambda_{1,mem} = 0.18\mu s$ and $\eta_{1,mem} = 0.9$Pa.s) using the displacement of a vessel wall and the SLS model of Maxwell form (Hosseinkhah *et al.*, 2013).

Results

A decrease of the distance between the bubble and the viscoelastic membrane is accompanied by an increase of the resonance frequency (see Figure 4.36). The increase of the resonance frequency is associated with a small gain of the modes eigenfrequencies (from 1.9 MHz to 2.0 MHz for the surface mode n=2).

Additionally, this increase is accompanied by an increase in the preponderant surface mode order. The preferred mode order at d=4.8 µm is n=2 (Figure 4.34 a)) across most insonation frequencies, while at the distance d=0.3 µm the preponderant mode order increases to n=6 at the frequency of 3.5 MHz or n=7 at the frequency of 3.6 MHz (Figure 4.35 b)).

However, the magnitude of the mode order n=2 remains the nearly same for all separation distances d. This observation demonstrates microbubbles can exhibit a combination of surface modes near viscoelastic membrane if the separation distance is small. In the case of a 1.725 µm radii microbubble the combination of surface modes appeared to begin for distances less or equal to 1.2 µm. This is comparable to the results presented by Xi *et al.* (2014), where a non-negligible effect on the modes was observed for distances d smaller than R_0 the radii of an uncoated bubble.

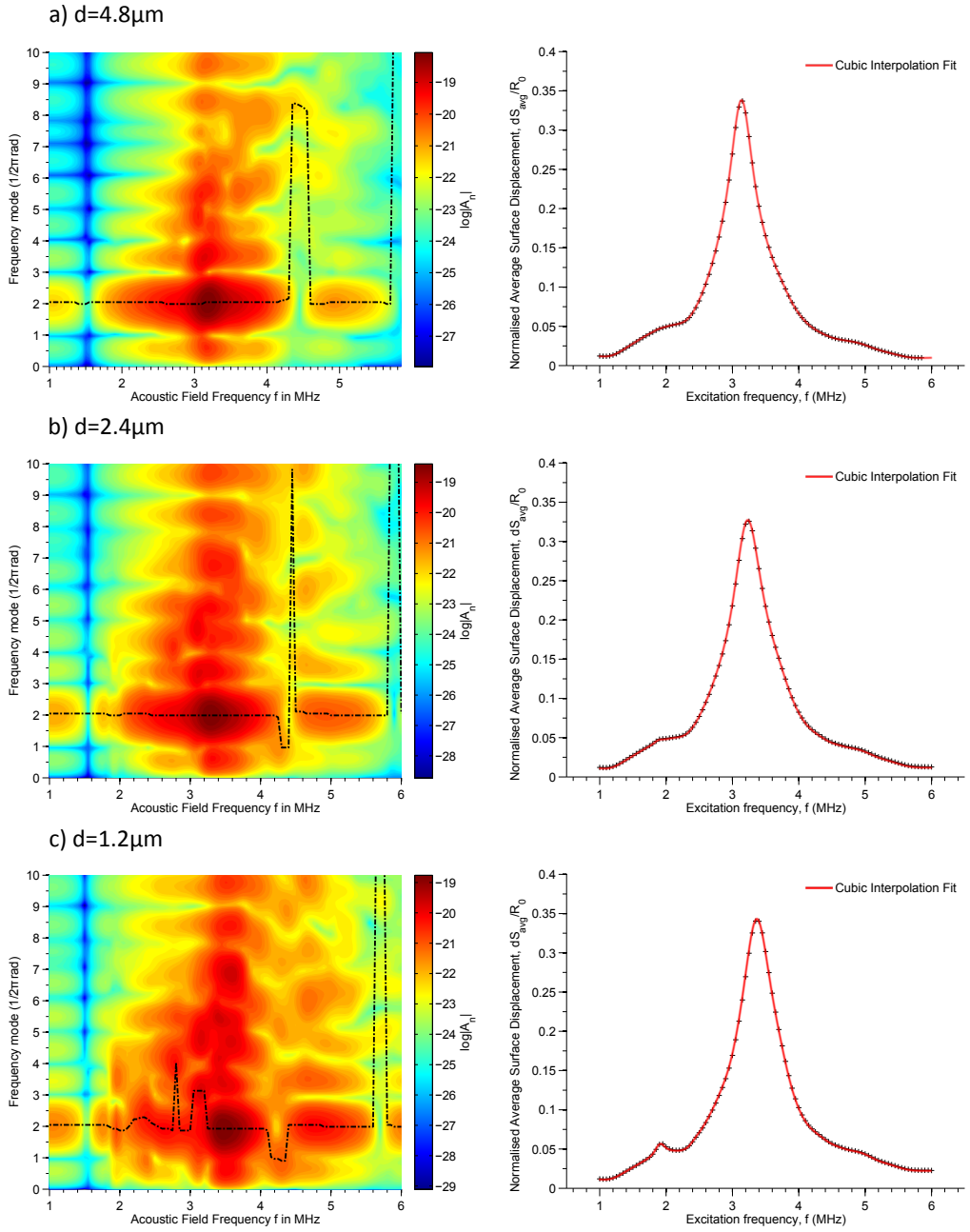

Figure 4.34: Mode spectrogram of a 1.725 µm radii microbubble for a range of distances d from a viscoelastic membrane at 40 kPa. a) d=4.8 µm, b) d=2.4 µm, c) d=1.2 µm. The dashed black line indicates the prevalent mode order at each insonation frequency. On the right are the normalised absolute surface displacement of each mode spectrogram using equation 3.35. Surface mode amplitudes were calculated using equation 4.3.

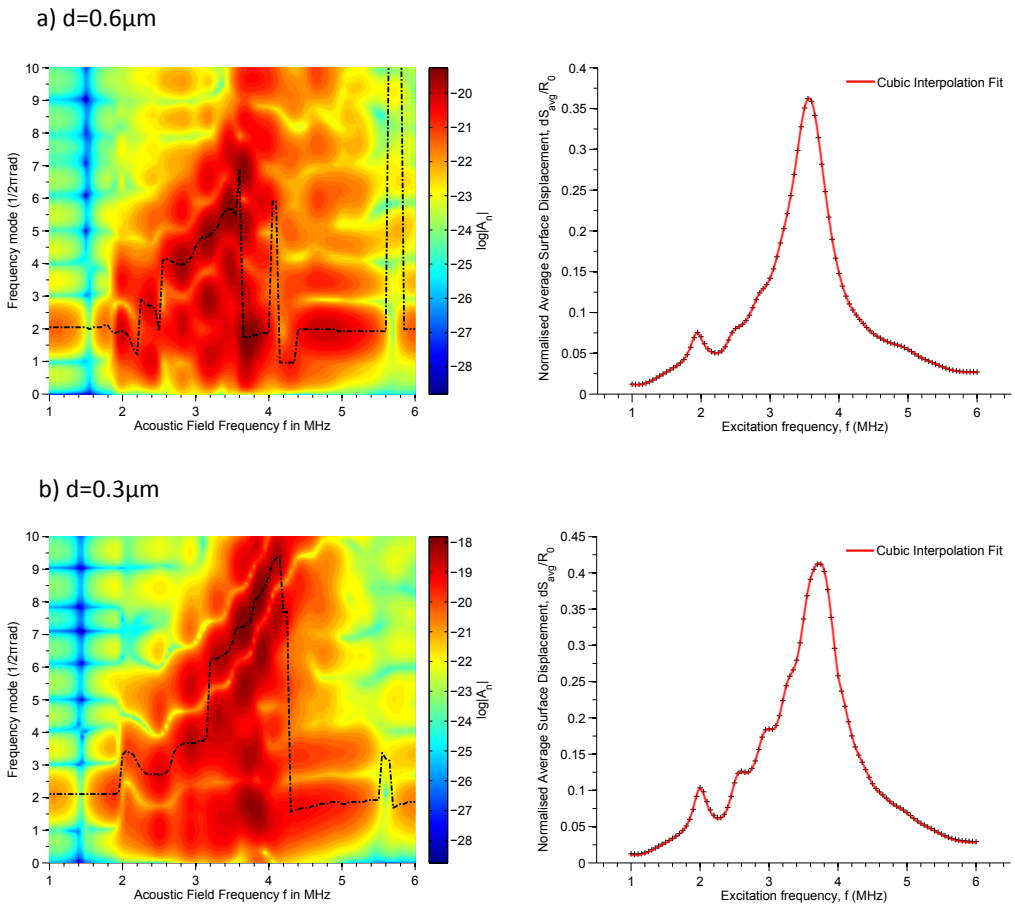

Figure 4.35: Mode spectrogram of a 1.725 µm radii microbubble for a range of distances d from a viscoelastic membrane at 40 kPa. a) d=0.6 µm, b) d=0.3 µm. The dashed black line indicates the prevalent mode order at each insonation frequency. On the right are the normalised absolute surface displacement of each mode spectrogram using equation 3.35. Surface mode amplitudes were calculated using equation 4.3.

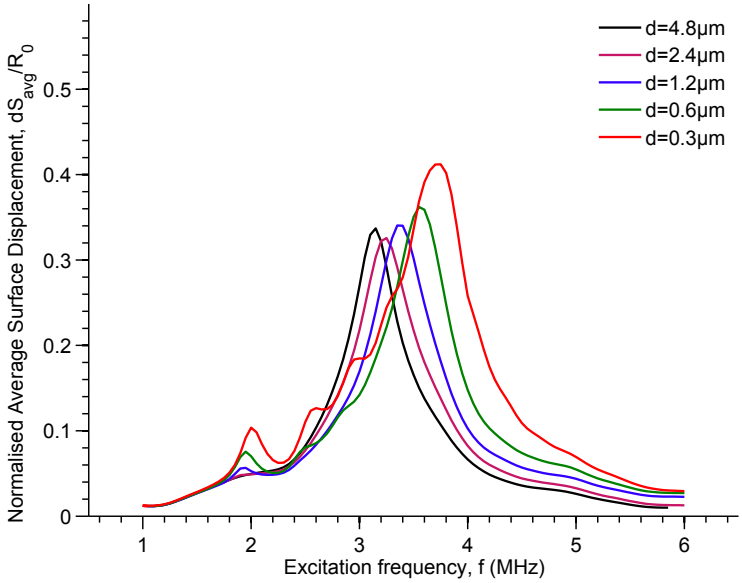

Figure 4.36: Comparison of the normalised average surface displacement from Figures 4.34 and 4.35 (equation 3.35). A 1.725 μm radii microbubble for a range of distances d from a viscoelastic membrane. The increase of the resonance frequency is associated with a small gain of the modes eigenfrequencies (from 1.9 MHz to 2.0 MHz for the surface mode n=2).

The results would be more relevant if the parameters used were those of a cell membrane or a vessel wall. However, the determination of the parameters from experimental results depends on the employed method, the viscoelastic model and the assumed thickness of the boundary Balocco *et al.* (2010) Hochmuth *et al.* (1973). The evaluation of cell membrane viscoelastic parameters are further discussed in Section 5.2 where modelled results with updated parameters from the literature are presented.

4.5 Discussion and concluding remarks

Surface modes were observed using high-speed imaging to appear at low acoustic pressures and at specific insonation frequencies. Larger microbubbles require a smaller frequency step to exhibit a different surface mode order compared to smaller microbubbles. This could allow to study the properties of the materials coating different type of microbubbles. Nonetheless, the model must be sufficiently accurate in terms of modelling physical phenomena to enable the comparison to experimental data. In this chapter, it was shown that the mode amplitude is intricately related to the material relaxation time. The shorter the relaxation time gets, the higher the mode amplitude becomes and *vice versa*. Interestingly, the relaxation time is specifically related to the amplitude of the surface modes for the relative large microbubble sizes ($R_0 > 4\mu m$) studied in this chapter. Thus, the modification of other model parameters — namely the Young's modulus and the viscosity of the coating material — was not necessary when the relaxation time was modified. This correlates with the results from chapter 3, where the change in the resonance frequency was negligible for a varying relaxation time for microbubbles with a radii larger than $2\mu m$.

In the presence of a viscoelastic membrane it was found that the increase of the resonance frequency of a microbubble reaching towards the membrane is accompanied by a increase of the order of the *prevalent surface mode*. Additionally, a combination of surface modes may exist. The numerical results were able to show that the increase in the resonance frequency as the distance separating a microbubble to a viscoelastic membrane decreases does not translate in an increase of the *surface modes eigenfrequencies*. Further research is required to find if this discorrelation remains for microbubbles near a hard boundary. Such behaviour would permit to have the eigenfrequencies of the modes estimated with high-speed imaging in Figure 4.24 independent of the separation distance d.

Additionally, it was found the magnitude of the surface modes increased for a decreasing separation distance d. This could have an implication is the understanding of the mechanisms of the sonoporation phenomenon with cells. It was

discussed in the introductory chapter 1 that Tho *et al.* (2007) observed microstreaming velocities increased during the presence of surface modes of order superior to $n = 1$. Therefore with the increase in the mode amplitude observed in the numerical results presented in this chapter, a potential increase in the microstreaming velocity is expected for a diminishing separation distance d from a flexible membrane. This mechanism provides clues to the efficacy of sonoporation at low acoustic pressures.

Chapter 5

The stress exerted by an oscillating microbubble on a nearby cell membrane

5.1 Introduction

The evaluation of the stress exerted by an oscillating microbubble on a nearby cell membrane can be found in the literature. Doinikov & Bouakaz (2010a) proposed a theoretical study on the sonoporation efficiency of a microbubble and cell mixture in a liquid medium by employing a Rayleigh-Plesset like equation. To achieve sonoporation a necessary lateral shear threshold of 12 Pa was assumed. The threshold was determined experimentally by Wu *et al.* (2002) whose study employed Jurkat lymphocyte cells and where the stress generated during sonoporation was assumed to be solely from of the microstreaming effect. The threshold theory was developed by Williams *et al.* (1970) and Rooney (1970) who attributed the forces necessary to induce cell lysis exclusively to a streaming shear stress. The streaming shear stress was defined with a dependency on the bubble oscillation amplitude, which, with sufficient oscillation amplitude, was observed to provide the necessary streaming shear above the lateral shear threshold. In this theory, the acoustic pressure generated by the oscillating bubbles near the cells was neglected. These studies attribute all biological effects, which includes the cell lysis, to the microstreaming. Since the shear threshold was established

without taking into account other possible mechanisms, the shear threshold value of 12 Pa is necessarily underestimated. The theoretical studies such as the one from Doinikov & Bouakaz (2010a) used the theory determined by Nyborg (1958) to estimate the shear induced by the liquid motion. However, the study assumed an underestimated shear threshold and thus the interpretation of the sonoporation efficiency by the exerted microstreaming flow should be taken with caution.

In a separate study, Doinikov & Bouakaz (2010b) found that a microbubble of 1.5 μm radii at 2.5 MHz undergoing a translational mode ($n = 1$) and the radial oscillations contributed mostly to the streaming velocity. The estimated a stress generated by the acoustic microstreaming was of the order of 20 to 60 Pa. Other studies discussing the shear induced by oscillating microbubbles have taken a different approach. The findings of Vos *et al.* (2011) estimated shear stress in the range of 25 to 350 kPa from high-speed optical imaging of oscillating microbubbles attached to a wall. The stress range was estimated using a potential flow theory and is higher than those calculated by Forbes *et al.* (2008) and Wu *et al.* (2002) that respectively found 17 kPa and 9 kPa using the theory defined by Rooney (1972).

The literature brings various suggested theories that try to elucidate the provenance of sonoporation. However the broad range of shear stress values found indicates an unanimous explanation for sonoporation has not yet been reached. This correlates to the lack of discernible mechanical aspects involved during sonoporation which was discussed in chapter 1. High-speed fluorescence imaging (Gelderblom, 2012) could provide additional observations on the interaction between microbubbles and cell membranes during the sonoporation process since in bright field imaging those interactions are difficult to be observed.

In this chapter, the finite element model introduced and discussed in the previous chapters is adapted to model the interaction between a microbubble and a viscoelastic membrane which models the endothelial surface layer of the inner capillaries. Firstly, a model of the endothelial cell lining will be introduced in

Section 5.2 and the necessary assumptions to model it will be discussed. Secondly, the theory to calculate the shear stress from the exerted acoustic pressure is expressed in Section 5.3. Finally, the results will be presented in Section 5.4 and discussed in Section 5.5.

5.2 The cell membrane model

Microbubbles are necessarily injected in the blood vessels via a syringe; they roam freely in the blood plasma along bigger cells such as erythrocytes, *i.e.* red blood cells. In this regard, the blood should not be regarded as a pure fluid, but a composite fluid. The viscosity of the blood varies with the hematocrit, the concentration of erythrocytes, thrombocytes and leukocytes in the blood (Chien *et al.*, 1966). As blood flows into small vessels, erythrocytes are known to aggregate and deform, and rotational viscometric studies by Chien *et al.* (1970) showed that the apparent viscosity of blood depends on the concentration of erythrocytes and the increases are due primarily to their aggregation (Bishop *et al.*, 2001). Since microbubbles have a size range of 0.7 to 10 µm in diameter (Gorce *et al.*, 2000; Kooiman *et al.*, 2014) and SonoVue® contrast agents were found to have mean diameter of 2.5 µm and more than 90% of the entities have a size of less than 8 µm (Schneider, 1999) in diameter which is on average smaller than the erythrocytes which have a width ranging from 8 to 10 µm (Barman *et al.*, 1993). In this regard, the liquid medium separating the cells composing the blood from the microbubbles is the blood plasma. The latter should be the medium modelled for studying the interaction of microbubbles and nearby cells or vessel walls.

In this chapter the liquid medium modelled is the plasma which is composed of water, a range of proteinous mixture and electrolytes (Krebs, 1950). The blood plasma has a viscosity in the range of 1.1 to 1.30×10^{-3} Pa.s at 37°C (Késmárky *et al.*, 2008). Therefore the viscosity is of the same order than the one of water at 25°C (298.15K) 0.9×10^{-3} Pa.s which in the previous chapters was neglected. The difference in viscosity between water at 25°C and the plasma at 37°C is negligible and the liquid medium is assumed non-viscous and incompressible in the

same manner as it was defined in chapter 3.2.1.

The endothelial surface layer lining the inner surface of capillaries was estimated by Pries *et al.* (2000) to have a thickness of 0.3 µm. However the estimation of the thickness is not straightforward as noted by Pries & Secomb (2005) the layer thickness may vary with the diameter of the capillaries. In the latter publication the thickness of the endothelial layer surface was estimated to vary from 0.2 to 2 µm.

Balocco *et al.* (2010) estimated the viscoelastic parameters of a vascular wall with the identical three-element Maxwell model presented in chapter 3 using experimental data gathered from ultrasound Doppler imaging to measure the blood flow and the wall displacements. The model was compared and adjusted to fit the experimental results to find the following parameters: $E = 7337$ Pa, $E_1 = 6826$ Pa, $\eta_1 = 883$ Pa.s. The latter two parameters can be used to estimate the equivalent relaxation time: $\lambda_1 = 2 * \eta_1(2 + \nu)/E_1 \simeq 0.385$ s. In another study, using atomic force microscopy Mathur *et al.* (2001) measured the elastic properties of cardiac muscle, skeletal muscle and endothelial cells. The determined elastic modulus of the endothelial cells varied depending on the location probed, the elastic modulus was 6.87±0.4 kPa over the nucleus, 3.37±0.2 kPa over the cell body in the proximity to the nucleus, and 1.47±0.1 kPa over the cell body near the edge. While the latter study measured the elastic properties of the endothelial cells, these values were estimated using for a purely elastic model. The relatively low elastic modulus lead to convergence issues in the FE model for a purely elastic material representing the cell lining. These values are of the same order to the elastic parameter estimated by Balocco *et al.* (2010). However, atomic force microscopy has the disadvantage to be limited to the estimation the compressional behaviour of the cells whereas a method using Doppler imaging allows the estimation of the displacements within a two dimensional image plane —compression and extension— of the tissue in its natural environment. The parameters used to model the cells lining a capillary are described in the table 5.1.

5.3 Theory of surface traction and surface shear

The surface shear is the force tangential to a surface which may include the exerted viscous shear stress from a fluid and the resultant tangential force from the material deformation caused by an acoustic pressure p. In this work, the viscous shear is not computed and therefore the calculated stress is limited to the effects of the acoustic pressure on the material. The exerted forces result in the stress $\mathbf{s}$ within the material which can be computed with help of the equation 3.6 presented in Section 3.2.2.

The traction vector $\boldsymbol{\tau}$ represents the stress of the material at its surface which is defined by the normal $\mathbf{n}$, however, the resultant force per area is not necessarily normal to the surface:

$$\boldsymbol{\tau} = \mathbf{sn}, \tag{5.1}$$

where $\mathbf{n}$ is the unit vector normal to the boundary and $\mathbf{s}$ is the total stress tensor.

The surface traction vector $\boldsymbol{\tau}_S$ tangential to the surface of the boundary, is determined from the traction vector by subtracting its normal component to the surface (Oshima *et al.*, 2001):

$$\boldsymbol{\tau}_S = \boldsymbol{\tau} - (\boldsymbol{\tau} \cdot \mathbf{n})\mathbf{n}, \tag{5.2}$$

Due to the oscillatory nature of a time-harmonic study, the mean value of the shear stress τ_{mean} defined by:

$$\tau_{mean} = \left\| \frac{1}{2\pi} \int_0^{2\pi} \boldsymbol{\tau}_S(\theta) \, \mathrm{d}\theta \right\|, \tag{5.3}$$

has an equivalent value of zero.

Therefore the study of the magnitude of the surface traction τ_{mag} is proposed, which is expressed by the Euclidean norm of the complex vector field:

$$\tau_{mag} = \|\tau_S\| = \sqrt{\|\boldsymbol{\tau}_{S|_x}\|^2 + \|\boldsymbol{\tau}_{S|_y}\|^2 + \|\boldsymbol{\tau}_{S|_z}\|^2} \tag{5.4}$$

The local surface shear τ_{shear} is equivalent to the arithmetic mean of the function 5.4 over the harmonic period 2π:

$$\begin{aligned}\tau_{shear} &= \frac{1}{2\pi}\int_0^{2\pi} \tau_{mag}(\theta)\ \mathrm{d}\theta \\ &= \frac{1}{2\pi}\int_0^{2\pi} \sqrt{(\|\boldsymbol{\tau}_{S|_x}(\theta)\|^2 + \|\boldsymbol{\tau}_{S|_y}(\theta)\|^2 + \|\boldsymbol{\tau}_{S|_z}(\theta)\|^2}\ \mathrm{d}\theta, \end{aligned} \tag{5.5}$$

where $\|\boldsymbol{\tau}_{S|_j}(\theta)\| = \|\boldsymbol{\tau}_{|_j} e^{i\theta} - (\boldsymbol{\tau}_{|_j} e^{i\theta} \cdot \mathbf{n}_{|_j})\mathbf{n}_{|_j}\|$ for $j = \{x, y, z\}$. Thus 5.5 defines the local lateral shear intensity on the boundary over an excitation cycle.

5.4 Results

Table 5.1: Cell lining parameters

Parameter	Value
Cell Young's Modulus, E_{cell}	7337 Pa (Balocco *et al.*, 2010)
Cell relaxation time, $\lambda_{1,cell}$	0.385 s
Cell shear Modulus, $G_{1,cell} = \eta_{1,cell}/\lambda_{1,cell}$	2293.5 Pa
Cell thickness, e_{cell}	800 nm
Microbubble shell Young's modulus, E	115 MPa
Microbubble shell viscosity, η_1	0.45 Pa.s
Microbubble shell relaxation time, λ_1	0.01 µs

The geometry of a capillary cell lining was simplified to a cylinder of a thickness e_{cell} and a radii $R_{cell} = 40\mu$m in order to limit the complexity of the mesh and allow convergence to a solution to be reached within 15 minutes at the probed frequency of 0.5 MHz. Other excitation frequencies were probed; however the convergence rates to a solution were impractical.

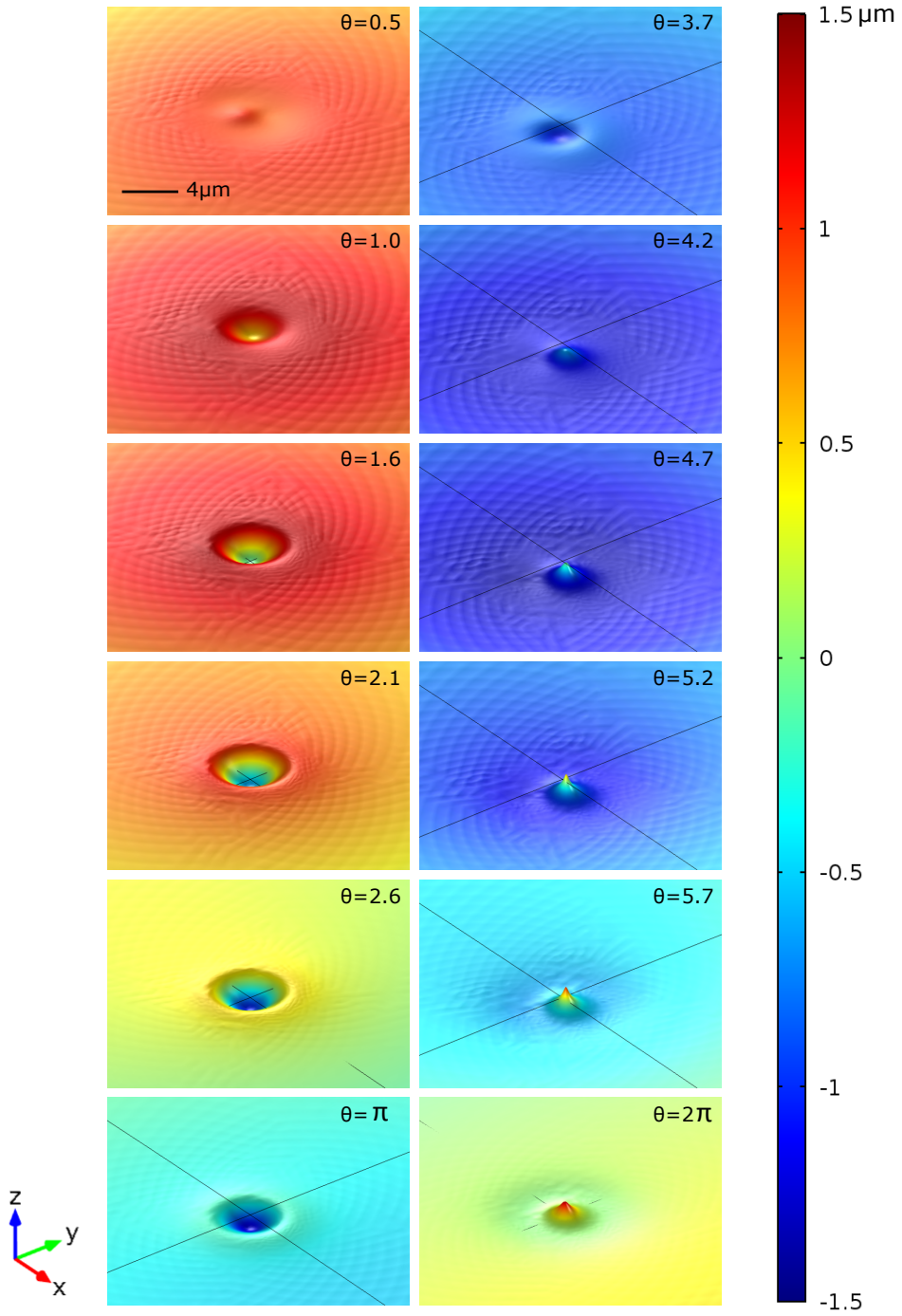

Figure 5.1: Cell membrane amplitude displacement in micrometers in the z axis (normal to the cell membrane). Used simulation parameters are presented in table 5.1, $p_0 = 80$ kPa and an insonation frequency $f = 0.5$ MHz.

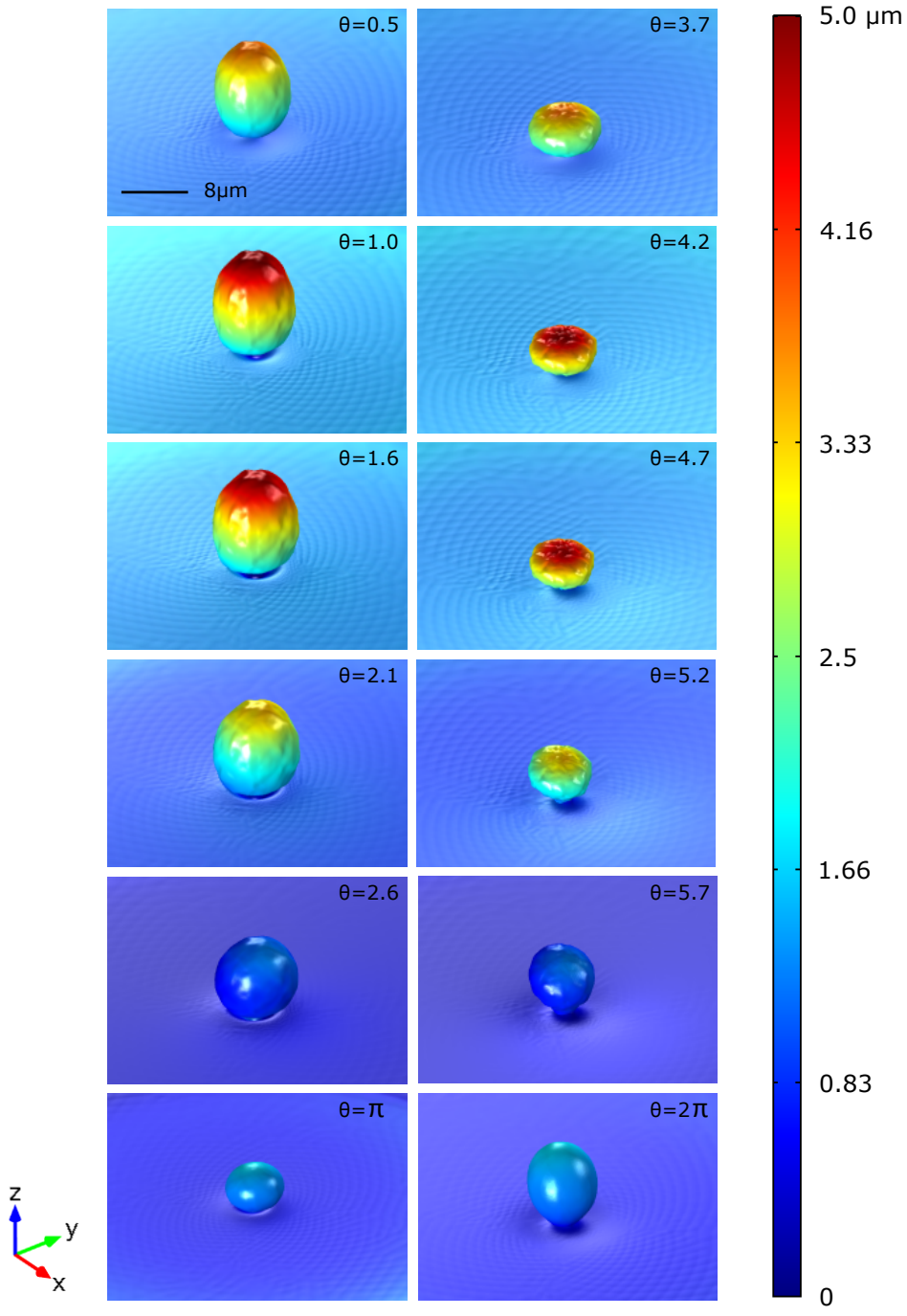

Figure 5.2: Bubble and cell membrane absolute amplitude displacement in micrometers. Used simulation parameters are presented in table 5.1, $p_0 = 80$ kPa and an insonation frequency $f = 0.5$ MHz.

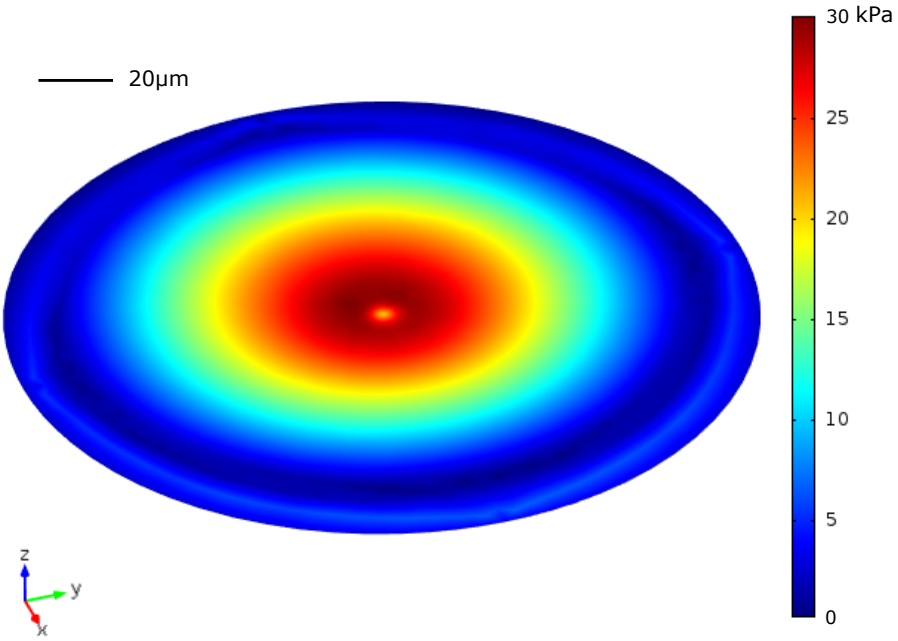

Figure 5.3: Mean shear stress tangential to the cell membrane (equation5.5). Used simulation parameters are presented in table 5.1, $p_0 = 80$ kPa and an insonation frequency $f = 0.5$ MHz.

The displacements of the cell membrane near an oscillating 4 μm radii microbubble are shown in Figure 5.1. An inward protrusion is followed by and outward protrusion. The microbubble was observed to undergo a mode order of $n = 2$ (Figure 5.2). The calculated mean surface shear stress is shown in figure 5.3. An estimated mean surface shear of the order of the 10^{th} of kPa and a local gradient the in mean shear stress can be observed in the region displaced. The cause of the local gradient can be explained using the surface traction plotted in Figure 5.4. In this Figure, the surface traction is represented by a vector field. One can observe, that at the phases $\theta = \pi$ and $\theta = 2\pi$, the surface traction at the centre is in opposite direction with the surface traction existing surrounding it. The measured surface traction is significant, with values of the order of 500 Pa at the centre of the formation of the protrusion, while surface traction of the order of 1000 Pa is exerted in the opposite direction. These opposing forces demonstrate

the acoustic pressure can cause a tearing effect on the surface of endothelial cells. This is accompanied by a protrusion which is apparent to a pore formation of an endothelial cell lining.

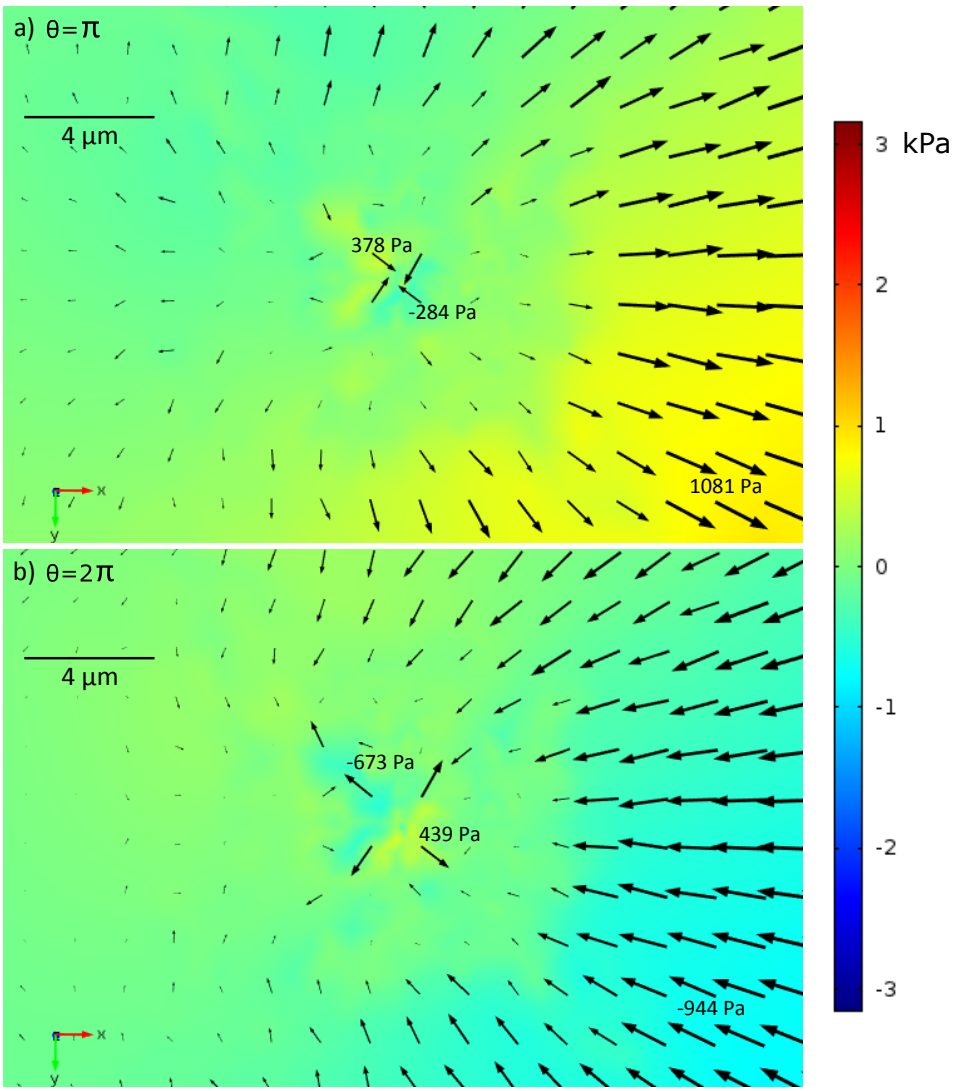

Figure 5.4: The surface traction tangential to the cell membrane (equation5.2). Used simulation parameters are presented in table 5.1, $p_0 = 80$ kPa and an insonation frequency $f = 0.5$ MHz.

5.5 Discussion and concluding remarks

The acoustic pressure was found to displace significantly a membrane modelling an endothelial cell lining. The displacement caused significant stress within the material and results in a tearing effect due to opposing surface traction in the region of the forming protrusion. The effect was observed for a microbubble of 4 μm in radii undergoing a surface mode of the second order. The mean shear stress of the order of 10^{th} of kPa is comparable to the values found by Vos *et al.* (2011) (25 to 350 kPa of steady acoustic shear stress), Forbes *et al.* (2008) (17 kPa of viscous shear stress due to microstreaming) and Wu *et al.* (2002) (9 kPa of viscous shear stress due to microstreaming).

However the value of the mean shear stress presented in this work is significantly higher than the shear stress of the order of 10^{th} of Pa (2 μm radii microbubble at 2 MHz and 200 kPa in contact with a rigid wall) estimated by Doinikov & Bouakaz (2010a) who considered only the microstreaming to calculate the shear.

While most discussed values found in the literature are those of the shear stress caused by the microstreaming, the results presented here provide additional data showing the forces exerted by the acoustic pressure between a microbubble and a cell is not negligible and cause significant shear stress. This was observed at pressure of 80 kPa, which is a relative low acoustic pressure at the considered frequency of 0.5 MHz (MI=0.11). The mean shear stress in addition to the shear stress exerted by the microstreaming provides strong clues to the origin of the mechanisms during the sonoporation phenomenon.

Chapter 6

Summary and conclusion

Chapter 1 introduced the ultrasound contrast agent's role in ultrasound imaging and their versatile use in therapeutic drug delivery. In the presence of ultrasound, several mechanical effects have been observed in the vicinity of microbubbles that have the potential to allow formation of a pore in a nearby cell: The jetting, the acoustic microstreaming and the radiated acoustic force phenomena. Whereas one or a combination of these mechanical effects are involved during the sonoporation phenomenon is still not well understood. While the jetting phenomenon occurs at high acoustic pressures, sonoporation can be observed at low acoustic pressure. However, low acoustic pressures have more practical uses in clinical applications since it can be achieved by a broader range of ultrasonic devices and poses fewer risks to the patient. It is in this scope, this work aimed to elucidate the principles of sonoporation.

In order to attain those answers, a finite element was proposed in this study. In Chapter 2, the rheological properties of the amphiphilic molecules at the gas-liquid interface of a microbubble were discussed and the standard linear solid of Maxwell form was found to be suitable to model their viscoelastic properties. The shear deformations in thin shells were presented and the assumption of infinitesimal strain–stress necessary for the Hooke's law was shown sufficient to model non-spherical deformations when implemented with a suitable method. The thin structure modelling the molecules of the microbubble was designed with sufficient degrees of freedom to allow the occurrence of bending and shearing within the

shell. In Chapter 3, this model permitted the comparison of the results against published experimental data to demonstrate the validity of the assumptions. The originality in implementing rheological properties within a thin shell allowed modelling the microbubble surface modes in the three-dimensional space.

In Chapter 4, high-speed imaging was employed to measure the occurrences of surface modes near an elastic layer. The surface modes of larger microbubbles were found to require a smaller frequency step to exhibit a different surface mode order compared to smaller microbubbles. Additionally, the FE model was compared to the frames acquired with the high-speed imaging system and enabled to demonstrate that the model is capable of successfully reproducing the microbubble dynamics near the elastic body. A shorter relaxation time of the viscoelastic shell was found to increase the surface mode amplitude, and *vice versa*. Furthermore, surface modes where found to increase in amplitude for a decreasing distance between microbubble and a viscoelastic membrane which was found concomitant to the increase of the order of the preponderant of surface mode. An increase in amplitude of the surface modes has the potential to enhance the local microstreaming velocity which in turn would exert increased shear stress on a nearby cell membrane. This mechanism contributes to the elucidation of the efficacy of the sonoporation at low acoustic pressures.

Although other phenomena are coupled to the oscillations such as the acoustic microstreaming, in Chapter 5, a method to estimate the mean shear stress caused by the acoustic pressure was proposed. This allowed estimating the stress exerted by a microbubble oscillating with a surface mode of second order. The deformation of the modelled endothelial lining was found significant and the value of the mean shear stress was found comparable to values found in the literature of the shear stress exerted by microstreaming. This emphasises the importance of the acoustically radiated pressure by a microbubble during the sonoporation phenomenon. The shear stress exerted by the acoustic pressure in combination of the shear stress caused by the microstreaming could explain the sonoporation phenomenon at low acoustic pressures.

One important limitation of the model is that the linear acoustic assumption should be satisfied. Perhaps, a moving mesh could be implemented to better account for the topological changes. This would enable to model the microbubble dynamics with better precision. However, the computational costs would increase remarkably.

Appendix A

Acoustic amplitude calibration

The following tables were the calibrated voltages used for the Agilent 33250A (Agilent Technologies Inc., Loveland, Colorado, USA) arbitrary waveform generator prior amplification by an E&I A300 (Electronics & Innovation Ltd., Rochester, NY, USA) broadband power amplifier. The pressures were estimated at a distance of 20.5 mm from the transducer in de-ionized milli-Q water (Millipore Corporation, Billerica, Massachusetts, USA) with a 0.20mm needle hydrophone (Precision Acoustic Ltd., Dorchester, United Kingdom) connected to an oscilloscope through a DC coupler.

Table A.1: For 100 kPa in free field

Frequency in MHz	Voltage in mV (peak positive)
0.6	440
0.65	390
0.7	340
0.8	330
0.9	310
1.0	300
1.1	320
1.2	370
1.3	410
1.4	450

Table A.2: For 80 kPa in free field

Frequency in MHz	Voltage in mV (peak positive)
0.6	260
0.65	230
0.7	200
0.8	200
0.9	190
1.0	180
1.1	190
1.2	220
1.3	250
1.4	270

Table A.3: For 72 kPa in free field

Frequency in MHz	Voltage in mV (peak positive)
0.6	186
0.65	164
0.7	143
0.8	140
0.9	136
1.0	130
1.1	136
1.2	157
1.3	179
1.4	193

Table A.4: For 50 kPa in free field

Frequency in MHz	Voltage in mV (peak positive)
0.6	130
0.7	105
0.8	100
0.9	95
1.0	90
1.1	95
1.2	110
1.3	125
1.4	135

References

Aus, G. (2006). Current status of hifu and cryotherapy in prostate cancer-a review. *European urology*, **50**, 927–934. 1

Baert, A. (2008). *Encyclopedia of diagnostic imaging*. Springer Verlag. 3

Baker, W.E. (1961). Axisymmetric modes of vibration of thin spherical shell. *The journal of the Acoustical society of America*, **33**, 1749. 75

Balocco, S., Basset, O., Courbebaisse, G., Boni, E., Frangi, A.F., Tortoli, P. & Cachard, C. (2010). Estimation of the viscoelastic properties of vessel walls using a computational model and doppler ultrasound. *Physics in medicine and biology*, **55**, 3557. 130, 136, 139

Barman, B., Ashwood, E. & Giddings, J. (1993). Separation and size distribution of red blood cells of diverse size, shape, and origin by flow/hyperlayer field-flow fractionation. *Analytical Biochemistry*, **212**, 35 – 42. 135

Birkin, P.R., Offin, D.G., Vian, C.J.B., Leighton, T.G. & Maksimov, A.O. (2011). Investigation of noninertial cavitation produced by an ultrasonic horn. *The Journal of the Acoustical Society of America*, **130**, 3297–3308. 12

Bishop, J.J., Nance, P.R., Popel, A.S., Intaglietta, M. & Johnson, P.C. (2001). Effect of erythrocyte aggregation on velocity profiles in venules. *American Journal of Physiology-Heart and Circulatory Physiology*, **280**, H222–H236. 135

Blackstock, D.T. (2000). *Fundamentals of physical acoustics*. John Wiley & Sons. 51

Bleeker, H., Shung, K. & Barnhart, J. (1990). Ultrasonic characterization of albunex, a new contrast agent. *The Journal of the Acoustical Society of America*, **87**, 1792. 3

Borden, M.A., Zhang, H., Gillies, R.J., Dayton, P.A. & Ferrara, K.W. (2008). A stimulus-responsive contrast agent for ultrasound molecular imaging. *Biomaterials*, **29**, 597 – 606. 4

Brezzi, F., Bathe, K.J. & Fortin, M. (1989). Mixed-interpolated elements for reissner–mindlin plates. *International Journal for Numerical Methods in Engineering*, **28**, 1787–1801. 25

Briggs, W.L., McCormick, S.F. *et al.* (2000). *A multigrid tutorial*. Siam. 46

Caskey, C.F., Kruse, D.E., Dayton, P.A., Kitano, T.K. & Ferrara, K.W. (2006). Microbubble oscillation in tubes with diameters of 12, 25, and 195 microns. *Applied Physics Letters*, **88**, –. 13

Ceric, H. (2005). *Numerical techniques in modern TCAD*. Technische Universität Wien. 40

Chatterjee, D. & Sarkar, K. (2003). A newtonian rheological model for the interface of microbubble contrast agents. *Ultrasound in medicine & biology*, **29**, 1749–1757. 21, 73

Chien, S., Usami, S., Taylor, H., Lundberg, J.L. & Gregersen, M.I. (1966). Effects of hematocrit and plasma proteins on human blood rheology at low shear rates. *J Appl Physiol*, **21**, 81–87. 135

Chien, S., Usami, S., Dellenback, R.J. & Gregersen, M.I. (1970). Shear-dependent deformation of erythrocytes in rheology of human blood. *Am. J. Physiol*, **219**, 136–142. 135

Christiansen, C., Kryvi, H., Sontum, P. & Skotland, T. (1994). Physical and biochemical characterization of albunex, a new ultrasound contrast agent consisting of air-filled albumin microspheres suspended in a solution of human albumin. *Biotechnology and applied biochemistry*, **19**, 307–320. 3

Church, C. (1995). The effects of an elastic solid surface layer on the radial pulsations of gas bubbles. *The Journal of the Acoustical Society of America*, **97**, 1510. 21, 55, 73

Cobbold, R. (2007). *Foundations of biomedical ultrasound*. Oxford University Press, USA. 51

Colin, A., Giermanska-Kahn, J., Langevin, D. & Desbat, B. (1997). Foaming properties of modified ethoxylated nonionic surfactants. *Langmuir*, **13**, 2953–2959. 21

Collis, J., Manasseh, R., Liovic, P., Tho, P., Ooi, A., Petkovic-Duran, K. & Zhu, Y. (2010). Cavitation microstreaming and stress fields created by microbubbles. *Ultrasonics*, **50**, 273–279. 8

Dai, L. & Jazar, R.N. (2012). *Nonlinear Approaches in Engineering Applications*. Springer. 49, 56

De Gennes, P.G., Brochard-Wyart, F. & Quéré, D. (2004). *Capillarity and wetting phenomena: drops, bubbles, pearls, waves*. Springer. 16

De Jong, N. (2002). Mechanical index. *European Journal of Echocardiography*, **3**, 73–74. 78

De Jong, N., Ten Cate, F., Lancee, C., Roelandt, J. & Bom, N. (1991). Principles and recent developments in ultrasound contrast agents. *Ultrasonics*, **29**, 324–330. 3

de Jong, N., Cornet, R. & Lance, C. (1994). Higher harmonics of vibrating gas-filled microspheres. part one: simulations. *Ultrasonics*, **32**, 447 – 453. 21

Delalande, A., Kotopoulis, S., Rovers, T., Pichon, C. & Postema, M. (2011). Sonoporation at a low mechanical index. *Bubble science, Engineering and Technology*, **3**, 3–12. 5

Dimitrov, D., Panaiotov, I., Richmond, P. & Ter-Minassian-Saraga, L. (1978). Dynamics of insoluble monolayers: I. dilatational or elastic modulus,

friction coefficient, and marangoni effect for dipalmitoyl lecithin monolayers. *Journal of Colloid and Interface Science*, **65**, 483–494. 19

Doinikov, A. & Bouakaz, A. (2010a). Theoretical investigation of shear stress generated by a contrast microbubble on the cell membrane as a mechanism for sonoporation. *The Journal of the Acoustical Society of America*, **128**, 11. 8, 126, 133, 134, 145

Doinikov, A. & Dayton, P. (2007). Maxwell rheological model for lipid-shelled ultrasound microbubble contrast agents. *The Journal of the Acoustical Society of America*, **121**, 3331. 21, 49, 73

Doinikov, A., Zhao, S. & Dayton, P. (2009a). Modeling of the acoustic response from contrast agent microbubbles near a rigid wall. *Ultrasonics*, **49**, 195–201. 49, 126

Doinikov, A.A. & Bouakaz, A. (2010b). Acoustic microstreaming around a gas bubble. *The Journal of the Acoustical Society of America*, **127**, 703–709. 134

Doinikov, A.A., Haac, J.F. & Dayton, P.A. (2009b). Modeling of nonlinear viscous stress in encapsulating shells of lipid-coated contrast agent microbubbles. *Ultrasonics*, **49**, 269–275. 21

Doinikov, A.A., Aired, L. & Bouakaz, A. (2011). Acoustic scattering from a contrast agent microbubble near an elastic wall of finite thickness. *Physics in Medicine and Biology*, **56**, 6951. 120

Dollet, B., Van Der Meer, S.M., Garbin, V., De Jong, N., Lohse, D. & Versluis, M. (2008). Nonspherical oscillations of ultrasound contrast agent microbubbles. *Ultrasound in medicine & biology*, **34**, 1465–1473. 76, 78, 83, 119

Drobac, M., Gilbert, B., Howard, R., Baigrie, R. & Rakowski, H. (1983). Ventricular septal defect after myocardial infarction: diagnosis by two-dimensional contrast echocardiography. *Circulation*, **67**, 335–341. 2

Espinosa, G., López-Montero, I., Monroy, F. & Langevin, D. (2011). Shear rheology of lipid monolayers and insights on membrane fluidity. *Proceedings of the National Academy of Sciences*, **108**, 6008–6013. 19

Faez, T., Goertz, D. & De Jong, N. (2011). Characterization of definity ultrasound contrast agent at frequency range of 5–15 mhz. *Ultrasound in medicine & biology*, **37**, 338–342. 81

Falou, O. (2011). *Modelling high ffrequency ultrasound scattering from cells and ultrasound Contrast Agents*. Ph.D. thesis, aAINR71394. 76

Falou, O., Sojahrood, A.J., Kumaradas, C. & Kolios, M. (2010). Modeling the effect of shell thickness on high frequency ultrasound scattering from ultrasound contrast agents. *Canadian Acoustics*, **38**, 38–39. 76

Flores, F.G. (2013). A prism solid element for large strain shell analysis. *Computer Methods in Applied Mechanics and Engineering*, **253**, 274–286. 26

Forbes, M., Steinberg, R. & OBrien Jr, W. (2008). Examination of inertial cavitation of optison in producing sonoporation of chinese hamster ovary cells. *Ultrasound in medicine & biology*, **34**, 2009–2018. 8, 134, 145

Frinking, P., Bouakaz, A., Kirkhorn, J., Ten Cate, F. & De Jong, N. (2000). Ultrasound contrast imaging: current and new potential methods. *Ultrasound in medicine & biology*, **26**, 965–975. 3

Fritzsch, T., Schartl, M. & Siegert, J. (1988). Preclinical and clinical results with an ultrasonic contrast agent. *Investigative radiology*, **23**, S302. 3

Gelderblom, E.C. (2012). *Ultra-high-speed fluorescence imaging*. Universiteit Twente. 11, 112, 134

Goldberg, B., Raichlen, J. & Forsberg, F. (2001). *Ultrasound contrast agents: basic principles and clinical applications*. Informa Healthcare. 3

Goldberg, B.B., Liu, J.B. & Forsberg, F. (1994). Ultrasound contrast agents: a review. *Ultrasound in medicine & biology*, **20**, 319–333. 3

Gorce, J.M., Arditi, M. & Schneider, M. (2000). Influence of bubble size distribution on the echogenicity of ultrasound contrast agents: A study of sonovue(tm). *Investigative Radiology*, **35**, 661–671. 135

Gramiak, R. & Shah, P. (1968). Echocardiography of the aortic root. *Investigative Radiology*, **3**, 356. 2

Hartsuijker, C. & Welleman, J. (2007). *Engineering Mechanics: Volume 2: Stresses, Strains, Displacements*. Engineering Mechanics, Springer. 24

Harvey, C.J., Blomley, M.J., Eckersley, R.J., Heckemann, R.A., Butler-Barnes, J. & Cosgrove, D.O. (2000). Pulse-inversion mode imaging of liver specific microbubbles: improved detection of subcentimetre metastases. *The Lancet*, **355**, 807–808. 2

Hettiarachchi, K., Talu, E., Longo, M., Dayton, P. & Lee, A. (2007). On-chip generation of microbubbles as a practical technology for manufacturing contrast agents for ultrasonic imaging. *Lab on a Chip*, **7**, 463–468. 11

Hochmuth, R., Mohandas, N. & Jr, P.B. (1973). Measurement of the elastic modulus for red cell membrane using a fluid mechanical technique. *Biophysical Journal*, **13**, 747 – 762. 130

Hoff, L. (2001). *Acoustic characterization of contrast agents for medical ultrasound imaging*. Springer Netherlands. 2, 21, 49

Hosseinkhah, N., Chen, H., Matula, T.J., Burns, P.N. & Hynynen, K. (2013). Mechanisms of microbubblevessel interactions and induced stresses: A numerical study. *The Journal of the Acoustical Society of America*, **134**, 1875–1885. 127

Hughes, T.J. (2012). *The finite element method: linear static and dynamic finite element analysis*. Courier Dover Publications. 30

Hughes, T.J. & Franca, L.P. (1988). A mixed finite element formulation for reissner-mindlin plate theory: Uniform convergence of all higher-order spaces. *Computer methods in applied mechanics and engineering*, **67**, 223–240. 25

Ihlenburg, F. (1998). *Finite element analysis of acoustic scattering*, vol. 132. Springer. 60

Jin, J.M., Jin, J. & Jin, J.M. (2002). *The finite element method in electromagnetics*. Wiley New York. 62

Johnson, C. (1987). *Numerical solution of partial differential equations by the finite element method*. Cambridge University Press, Cambridge. 33, 36, 38, 39

Késmárky, G., Kenyeres, P., Rábai, M. & Tóth, K. (2008). Plasma viscosity: a forgotten variable. *Clinical hemorheology and microcirculation*, **39**, 243–246. 135

Kim, W., Kim, T.H., Choi, J. & Kim, H.Y. (2009). Mechanism of particle removal by megasonic waves. *Applied Physics Letters*, **94**, 081908. 12

Kooiman, K., Böhmer, M., Emmer, M., Vos, H., Chlon, C., Shi, W., Hall, C., de Winter, S., Schroën, K., Versluis, M. *et al.* (2009). Oil-filled polymer microcapsules for ultrasound-mediated delivery of lipophilic drugs. *Journal of Controlled Release*, **133**, 109–118. 4

Kooiman, K., Foppen-Harteveld, M., der Steen, A.F.v. & de Jong, N. (2011). Sonoporation of endothelial cells by vibrating targeted microbubbles. *Journal of Controlled Release*, **154**, 35–41. 5

Kooiman, K., Vos, R., Versluis, M. & de Jong, N. (2014). Acoustic behavior of microbubbles and implications for drug delivery. *Advanced drug delivery reviews*, **72**, 28–48. 6, 11, 12, 135

Krebs, H. (1950). Chemical composition of blood plasma and serum. *Annual review of biochemistry*, **19**, 409–430. 135

Kudo, N., Okada, K. & Yamamoto, K. (2009). Sonoporation by single-shot pulsed ultrasound with microbubbles adjacent to cells. *Biophysical journal*, **96**, 4866–4876. 6

Kuzmin, A., Luisier, M. & Schenk, O. (2013). Fast methods for computing selected elements of the greens function in massively parallel nanoelectronic device simulations. In *Euro-Par 2013 Parallel Processing*, 533–544, Springer. 44

Lai, C.Y., Wu, C.H., Chen, C.C. & Li, P.C. (2006). Quantitative relations of acoustic inertial cavitation with sonoporation and cell viability. *Ultrasound in medicine & biology*, **32**, 1931–1941. 8

Lamb, H. (1882). On the vibrations of a spherical shell. *Proceedings of the London Mathematical Society*, **1**, 50–56. 24

Lamb, H. (1917). On waves in an elastic plate. *Proceedings of the Royal Society of London. Series A*, **93**, 114–128. 75

Lamb, H. (1993). *Hydrodynamics*. Cambridge university press. 76

Landau, L. & Lifshitz, E. (1987). *Fluid Mechanics: Volume 6 (Course Of Theoretical Physics)*. Butterworth-Heinemann. 53

Léauté, G., Mclaughlan, J., Harput, S., Cowell, D. & Freear, S. (2012). Comsol modelling of non-spherical microbubble dynamics near a soft membrane. In *Ultrasonics Symposium (IUS), 2012 IEEE International*, 2286–2289, IEEE. viii, 6, 9

Lee, D.J., Lyshchik, A., Huamani, J., Hallahan, D.E. & Fleischer, A.C. (2008). Relationship between retention of a vascular endothelial growth factor receptor 2 (vegfr2)-targeted ultrasonographic contrast agent and the level of vegfr2 expression in an in vivo breast cancer model. *Journal of Ultrasound in Medicine*, **27**, 855–866. 8

Leighton, T. (1997). *The acoustic bubble*. Academic Pr. 76

Lewis, B.A. & Engelman, D.M. (1983). Lipid bilayer thickness varies linearly with acyl chain length in fluid phosphatidylcholine vesicles. *Journal of Molecular Biology*, **166**, 211 – 217. 28

Lind, S.J. & Phillips, T.N. (2013). The effect of viscoelasticity on the dynamics of gas bubbles near free surfaces. *Physics of Fluids (1994-present)*, **25**. 8

Love, A.E.H. (1888). The small free vibrations and deformation of a thin elastic shell. *Philosophical Transactions of the Royal Society of London. (A.)*, **179**, 491–546. 24

Malzert, A., Boury, F., Saulnier, P., Benoit, J. & Proust, J. (2002). Rheological study of lysozyme and peg2000 at the air-water and dichloromethane-water interfaces under ramp type or sinusoidal perturbations. *Langmuir*, **18**, 10248–10254. 19

Maresca, D., Emmer, M., van Neer, P., Vos, H., Versluis, M., Muller, M., de Jong, N. & van der Steen, A. (2010). Acoustic sizing of an ultrasound contrast agent. *Ultrasound in medicine & biology*, **36**, 1713–1721. 3

Marmottant, P., van der Meer, S., Emmer, M., Versluis, M., de Jong, N., Hilgenfeldt, S. & Lohse, D. (2005). A model for large amplitude oscillations of coated bubbles accounting for buckling and rupture. *The Journal of the Acoustical Society of America*, **118**, 3499–3505. 21, 73

Marmottant, P., Versluis, M., de Jong, N., Hilgenfeldt, S. & Lohse, D. (2006). High-speed imaging of an ultrasound-driven bubble in contact with a wall:narcissus effect and resolved acoustic streaming. *Experiments in fluids*, **41**, 147–153. 63, 75

Marra, V. (2013). On solvers: The v-cycle multigrid. Available at: www.comsol.com/blogs/on-solvers-v-cycle-multigrid [accessed 7 April 2015]. 46

Mathur, A.B., Collinsworth, A.M., Reichert, W.M., Kraus, W.E. & Truskey, G.A. (2001). Endothelial, cardiac muscle and skeletal muscle exhibit different viscous and elastic properties as determined by atomic force microscopy. *Journal of Biomechanics*, **34**, 1545 – 1553. 136

McKendry, J., Grant, C., Johnson, B., Coletta, P., Evans, J. & Evans, S. (2010). Force spectroscopy of streptavidin conjugated lipid coated microbubbles. *Bubble Science, Engineering &# 38; Technology*, **2**, 48–54. 72

McLaughlan, J., Ingram, N., Smith, P., Harput, S., Coletta, P., Evans, S. & Freear, S. (2013). Increasing the sonoporation efficiency of targeted polydisperse microbubble populations using chirp excitation. *Ultrasonics, Ferroelectrics and Frequency Control, IEEE Transactions on*, **60**, 2511–2520. 5, 6, 11, 81

Meijering, B., Juffermans, L., van Wamel, A., Henning, R., Zuhorn, I., Emmer, M., Versteilen, A., Paulus, W., van Gilst, W., Kooiman, K. *et al.* (2009). Ultrasound and microbubble-targeted delivery of macromolecules is regulated by induction of endocytosis and pore formation. *Circulation research*, **104**, 679. 4

Meire, H., Farrant, P. & ter Haar, G. (1995). Basic ultrasound. *Radiation Research*, **144**, 349–349. 1

Monroy, F., Giermanska Kahn, J. & Langevin, D. (1998). Dilational viscoelasticity of surfactant monolayers. *Colloids and Surfaces A: Physicochemical and Engineering Aspects*, **143**, 251–260. 16

Monteux, C., Fuller, G.G. & Bergeron, V. (2004). Shear and dilational surface rheology of oppositely charged polyelectrolyte/surfactant microgels adsorbed at the air-water interface. influence on foam stability. *The Journal of Physical Chemistry B*, **108**, 16473–16482. 21, 53

Moosavi Nejad, S., Hosseini, S.H.R., Akiyama, H. & Tachibana, K. (2011). Optical observation of cell sonoporation with low intensity ultrasound. *Biochemical and biophysical research communications*, **413**, 218–223. 79

Morgan, K., Allen, J., Dayton, P., Chomas, J., Klibaov, A. & Ferrara, K. (2000). Experimental and theoretical evaluation of microbubble behavior: Effect of transmitted phase and bubble size. *Ultrasonics, Ferroelectrics and Frequency Control, IEEE Transactions on*, **47**, 1494–1509. 63

Morse, P.M. (1986). *Theoretical acoustics*. Princeton University Press. 53

Neppiras, E. (1980). Acoustic cavitation. *Physics reports*, **61**, 159–251. 76

Nyborg, W. (1958). Acoustic streaming near a boundary. *The Journal of the Acoustical Society of America*, **30**, 329–339. 8, 134

Offin, D.G., Birkin, P.R. & Leighton, T.G. (2014). An electrochemical and high-speed imaging study of micropore decontamination by acoustic bubble entrapment. *Physical Chemistry Chemical Physics*, **16**, 4982–4989. 12

Ohl, C., Arora, M., Ikink, R., De Jong, N., Versluis, M., Delius, M. & Lohse, D. (2006). Sonoporation from jetting cavitation bubbles. *Biophysical journal*, **91**, 4285–4295. 6

Oshima, M., Torii, R., Kobayashi, T., Taniguchi, N. & Takagi, K. (2001). Finite element simulation of blood flow in the cerebral artery. *Computer Methods in Applied Mechanics and Engineering*, **191**, 661 – 671, minisymposium on Methods for Flow Simulation and Modeling. 137

Patil, A., Reynolds, P. & Hossack, J. (2010). A non-linear three-dimensional model for quantifying microbubble dynamics. *The Journal of the Acoustical Society of America*, 80–86. 71

Paulose, J. & Nelson, D.R. (2013). Buckling pathways in spherical shells with soft spots. *Soft Matter*, **9**, 8227–8245. 28, 72

Payne, E.M.B., Illesinghe, S.J., Ooi, A. & Manasseh, R. (2005). Symmetric mode resonance of bubbles attached to a rigid boundary. *The Journal of the Acoustical Society of America*, **118**, 2841–2849. 120

Peyman, S.A., Abou-Saleh, R.H., McLaughlan, J.R., Ingram, N., Johnson, B.R., Critchley, K., Freear, S., Evans, J.A., Markham, A.F., Coletta, P.L. *et al.* (2012). Expanding 3d geometry for enhanced on-chip microbubble production and single step formation of liposome modified microbubbles. *Lab on a Chip*, **12**, 4544–4552. 5, 11

Pinkerton, J. (1949). The absorption of ultrasonic waves in liquids and its relation to molecular constitution. *Proceedings of the Physical Society. Section B*, **62**, 129. 51

Prentice, P., Cuschieri, A., Dholakia, K., Prausnitz, M. & Campbell, P. (2005). Membrane disruption by optically controlled microbubble cavitation. *Nature Physics*, **1**, 107–110. 6, 93

Pries, A., Secomb, T. & Gaehtgens, P. (2000). The endothelial surface layer. *Pflgers Archiv Eur J Physiol*, **440**, 653–666. 136

Pries, A.R. & Secomb, T.W. (2005). Microvascular blood viscosity in vivo and the endothelial surface layer. *American Journal of Physiology - Heart and Circulatory Physiology*, **289**, H2657–H2664. 136

Pua, E.C. & Zhong, P. (2009). Ultrasound-mediated drug delivery. *Engineering in Medicine and Biology Magazine, IEEE*, **28**, 64–75. 6

Rayleigh, L. (1881). On the infinitesimal bending of surfaces of revolution. *Proceedings of the London Mathematical Society*, **1**, 4–16. 24

Rooney, J. (1972). Shear as a mechanism for sonically induced biological effects. *The Journal of the Acoustical Society of America*, **52**, 1718. 134

Rooney, J.A. (1970). Hemolysis near an ultrasonically pulsating gas bubble. *Science*, **169**, 869–871. 133

Sarkar, K., Shi, W., Chatterjee, D. & Forsberg, F. (2005). Characterization of ultrasound contrast microbubbles using in vitro experiments and viscous and viscoelastic interface models for encapsulation. *The Journal of the Acoustical Society of America*, **118**, 539. 63

Saulnier, P., Boury, F., Malzert, A., Heurtault, B., Ivanova, T., Cagna, A., Panaiotov, I. & Proust, J. (2001). Rheological model for the study of dilational properties of monolayers. comportment of dipalmitoylphosphatidylcholine (dppc) at the dichloromethane (dcm)/water interface under ramp type or sinusoidal perturbations. *Langmuir*, **17**, 8104–8111. 19, 53, 73

Schenk, O. & Gärtner, K. (2004). Solving unsymmetric sparse systems of linear equations with pardiso. *Future Generation Computer Systems*, **20**, 475–487. 44

Schlief, R., Staks, T., Mahler, M., Rufer, M., Fritzsch, T. & Seifert, W. (1990). Successful opacification of the left heart chambers on echocardiographic examination after intravenous injection of a new saccharide based contrast agent. *Echocardiography*, **7**, 61–64. 3

Schneider, M. (1999). Characteristics of sonovue. *Echocardiography*, **16**, 743–746. 135

Shortencarier, M.J., Dayton, P.A., Bloch, S.H., Schumann, P.A., Matsunaga, T.O. & Ferrara, K.W. (2004). A method for radiation-force localized drug delivery using gas-filled lipospheres. *Ultrasonics, Ferroelectrics and Frequency Control, IEEE Transactions on*, **51**, 822–831. 5, 79

Szabo, T. (2004). *Diagnostic ultrasound imaging: inside out*. Academic Press. 1

Teh, S.Y., Lin, R., Hung, L.H. & Lee, A.P. (2008). Droplet microfluidics. *Lab on a Chip*, **8**, 198–220. 11

Temkin, S. & Temkin, S. (1981). *Elements of acoustics*. Wiley. 51

Tho, P., Manasseh, R. & Ooi, A. (2007). Cavitation microstreaming patterns in single and multiple bubble systems. *Journal of Fluid Mechanics*, **576**, 191–233. 12, 132

Truesdell, C. (1945). The membrane theory of shells of revolution. *Transactions of the American Mathematical Society*, **58**, 96–166. 25

Tu, J., Guan, J., Qiu, Y. & Matula, T. (2009). Estimating the shell parameters of sonovue microbubbles using light scattering. *The Journal of the Acoustical Society of America*, **126**, 2954. 74

Unger, E.C., Porter, T., Culp, W., Labell, R., Matsunaga, T. & Zutshi, R. (2004). Therapeutic applications of lipid-coated microbubbles. *Advanced drug delivery reviews*, **56**, 1291–1314. 4

Van Der Meer, S., Versluis, M., Lohse, D., Chin, C., Bouakaz, A. & De Jong, N. (2004). The resonance frequency of sonovue as observed by high-speed optical imaging. In *Ultrasonics Symposium, 2004 IEEE*, vol. 1, 343–345, IEEE. ix, x, 65, 66, 67, 68, 71, 74

van der Meer, S.M., Dollet, B., Voormolen, M.M., Chin, C.T., Bouakaz, A., de Jong, N., Versluis, M. & Lohse, D. (2007). Microbubble spectroscopy of ultrasound contrast agents. *The Journal of the Acoustical Society of America*, **121**, 648–656. 71

Van Wamel, A., Kooiman, K., Harteveld, M., Emmer, M., Ten Cate, F., Versluis, M. & De Jong, N. (2006). Vibrating microbubbles poking individual cells: drug transfer into cells via sonoporation. *Journal of controlled release*, **112**, 149–155. 8

Versluis, M., Goertz, D.E., Palanchon, P., Heitman, I.L., Van Der Meer, S.M., Dollet, B., De Jong, N. & Lohse, D. (2010). Microbubble shape oscillations excited through ultrasonic parametric driving. *Physical Review E*, **82**, 026321. 83

Vos, H., Dollet, B., Bosch, J., Versluis, M. & De Jong, N. (2008). Nonspherical vibrations of microbubbles in contact with a walla pilot study at low mechanical index. *Ultrasound in medicine & biology*, **34**, 685–688. 13, 78

Vos, H., Emmer, M. & de Jong, N. (2009). Oscillation of single microbubbles at room versus body temperature. In *Ultrasonics Symposium, 2008. IUS 2008. IEEE*, 982–984, IEEE. x, 69, 70, 71

Vos, H., Dollet, B., Versluis, M. & de Jong, N. (2011). Nonspherical shape oscillations of coated microbubbles in contact with a wall. *Ultrasound in medicine & biology*, **37**, 935–948. 134, 145

Wan, F. & Weinitschke, H. (1988). On shells of revolution with the love-kirchhoff hypotheses. *Journal of engineering mathematics*, **22**, 285–334. 24

Wang, C., Rallabandi, B. & Hilgenfeldt, S. (2013). Frequency dependence and frequency control of microbubble streaming flows. *Physics of Fluids (1994-present)*, **25**, 022002. 12

Watson, Y.E., Birkin, P.R. & Leighton, T.G. (2003). Electrochemical detection of bubble oscillation. *Ultrasonics sonochemistry*, **10**, 65–69. 12

White, R.E. (1985). *An introduction to the finite element method with applications to nonlinear problems*. John Wiley. 38, 39

Williams, A., Hughes, D. & Nyborg, W. (1970). Hemolysis near a transversely oscillating wire. *Science*, **169**, 871–873. 133

Wu, J. (2002). Theoretical study on shear stress generated by microstreaming surrounding contrast agents attached to living cells. *Ultrasound in Medicine & Biology*, **28**, 125–129. 8

Wu, J., Ross, J. & Chiu, J. (2002). Reparable sonoporation generated by microstreaming. *The Journal of the Acoustical Society of America*, **111**, 1460. 11, 133, 134, 145

Xi, X., Cegla, F., Mettin, R., Holsteyns, F. & Lippert, A. (2014). Study of non-spherical bubble oscillations near a surface in a weak acoustic standing wave field. *The Journal of the Acoustical Society of America*, **135**, 1731–1741. 12, 120, 127

Yang, D., Gao, Y., Tan, K., Zuo, Z., Yang, W., Hua, X., Li, P., Zhang, Y. & Wang, G. (2013). Inhibition of hepatic fibrosis with artificial microrna using ultrasound and cationic liposome-bearing microbubbles. *Gene therapy*, **20**, 1140–1148. 8

Zhao, S., Ferrara, K. & Dayton, P. (2005). Asymmetric oscillation of adherent targeted ultrasound contrast agents. *Applied physics letters*, **87**, 134103. 13

REFERENCES

Zienkiewicz, O.C. & Taylor, R.L. (2005). *The finite element method for solid and structural mechanics*. Butterworth-heinemann. 30, 34, 41, 46